國立臺灣大學理學院物理學系

碩士論文

Department of Physics

College of Science

National Taiwan University

Master Thesis

用於平面型離子阱晶體之容受微動的快速量子糾纏閘

Micromotion-tolerant Fast Entangling Gates in Planar Trapped-ion Crystals

林君錡

Chun-Chi Lin

指導教授: 林俊達 博士

Advisor: Guin-Dar Lin, Ph.D.

中華民國 111 年 9 月

September 2022

doi:10.6342/NTU202203211

國立臺灣大學碩士學位論文

口試委員會審定書

用於平面型離子阱晶體之容受微動的快速量子糾纏閘

Micromotion-tolerant Fast Entangling Gates in Planar Trapped-ion Crystals

本論文係林君錡君（學號 R08222026）在國立臺灣大學物理學系完成之碩士學位論文，於民國 111 年 7 月 29 日承下列考試委員審查通過及口試及格，特此證明

口試委員：_____ (簽名)

（指導教授）

_____ Dr. Ming-Shien Chang

Hsi-Sheng Goan _____

系主任 _____ (簽名)

doi:10.6342/NTU202203211

誌謝

本研究與論文能夠順利完成，首先必須感謝我的指導教授林俊達老師。感謝老師在我碩二失去原指導教授這個艱難的時刻，接收我進入現在的研究團隊並且帶我認識離子阱量子計算的研究領域。謝謝老師在每週的討論中，帶給我許多思考問題的角度與提供研究的方向、以及在論文口試中的各種幫忙，讓我受益匪淺。也要感謝同在團隊中的許婷學姊參與我們的研究討論、適時提供建議與分享相關研究資訊。另外，由衷感謝管希聖教授、張銘顯博士和童世光教授在百忙之中抽空參與我的論文審查和論文口試，並互相分享來自各相關領域的專業意見。最後，感念我的前指導教授朱時宜老師，永遠感謝老師以及他所帶領的團隊成員們，訓練我且陪伴我進入理論物理的研究世界。

doi:10.6342/NTU202203211

doi:10.6342/NTU202203211

摘要

離子阱被視為最有前景的量子計算平台之一，不僅是因為它的量子比特具有長時間的同調性，同時也是因為離子間的強相互作用致使多量子比特閘得以實現。雖然傳統的離子阱量子計算是透過讓離子們排列成一條直鏈來進行操作的，但其較差的可擴展性已然成為一個棘手的問題。在這篇論文中，我展示出一種更具擴展性的配置，即令離子排列於一張平面上，形成一個二維晶體的結構。對此離子阱作理論分析後，可得知離子在平面內必定產生某種微小運動；而若不適度把該運動列入考量，更將會不可避免地防礙量子閘的實際表現。因鑑於此，本文提出一種基於段氏方案的脈衝型雙量子比特快速閘，用以產生兩量子比特間之糾纏態，展示出即使在微運動的影響之下仍然可以獲得高保真度和較短的閘時間。實驗模擬選用的是 $^{40}Ca^{+}$ 離子以及波長 393 奈米之雷射脈衝光，而此波長對應到的即是 $4S_{1/2}$ 態和 $4P_{3/2}$ 態之間的共振躍遷。

關鍵字：量子計算、離子阱、快速閘、量子糾纏、微小運動

doi:10.6342/NTU202203211

doi:10.6342/NTU202203211

Abstract

Ion traps are one of the most promising platforms for quantum computing, not only because of their long qubit coherence time, but also because of the strong ion-ion interaction that enables the multi-qubit gates. While traditional trapped-ion quantum computing is implemented by ions arranged in a linear chain, its poor scalability has become an intractable problem. In this thesis I present a more scalable configuration, ions arranged in a plane forming a two-dimensional crystal structure. A theoretical analysis of this ion trap shows that there must be some in-plane micromotion, which inevitably hinders the actual performance of quantum gates if the motion is not properly taken into account. In light of this, a pulsed two-qubit entangling fast gate based on Duan's scheme is proposed in the thesis, demonstrating that high fidelity and short gate time can still be available even in the presence of micromotion. The simulation is carried out with $^{40}Ca^{+}$ ions, using laser pulses resonant to the 393-nm transition between the $4S_{1/2}$ and $4P_{3/2}$ states.

Keywords: quantum computing, ion trap, fast gate, quantum entanglement, micromotion

doi:10.6342/NTU202203211

doi:10.6342/NTU202203211

Contents

doi:10.6342/NTU202203211

doi:10.6342/NTU202203211

doi:10.6342/NTU202203211

doi:10.6342/NTU202203211

List of Figures

doi:10.6342/NTU202203211

doi:10.6342/NTU202203211

List of Tables

doi:10.6342/NTU202203211

doi:10.6342/NTU202203211

Chapter 1

Introduction

1.1 Quantum Computing with Trapped Ions

The idea of using ions to realize quantum computation was first proposed by Cirac and Zoller in 1995 [1]. In their implementation, ions are confined in a radio-frequency (RF) Paul trap [2] and serve as qubits. The quantum information stored in an individual ion may be shared with another ion through their quantized collective motional modes, achieving quantum entanglement. Today, ion traps has become one of the most promising platforms for quantum computing because of their long qubit coherence time, and also the strong ion-ion interaction that enables two-qubit entangling gates.

Since quantum information is encoded in internal electronic states, it is preferable to seek for atoms with relatively simple level structure in the valence shell. The alkali-like ions, such as Be^+, Mg^+, Ca^+, Sr^+, Ba^+ and Yb^+, are therefore our desired candidates for qubits. These singly ionized ions provide a single electron in the $n\mathrm{S}_{1/2}$ state that can be used to perform quantum information processing. Furthermore, the fact that they carry a positive charge makes it possible to trap the ions in space by external electromagnetic

doi:10.6342/NTU202203211

fields. In general, trapped-ion qubits are divided into four types based on the chosen internal states where quantum information is encoded: hyperfine qubits, Zeeman qubits, fine-structure qubits, and optical qubits. Hyperfine qubits are encoded between the so-called clock states $|f = i \pm \frac{1}{2}, m_f = 0\rangle$ in the $n\mathrm{S}_{1/2}$ manifold for ions of nonzero nuclear spin ($i \neq 0$). Zeeman qubits, on the other hand, are similarly encoded in the $n\mathrm{S}_{1/2}$ manifold, but the two qubit levels $|m_s = \pm\frac{1}{2}\rangle$ are separated with the aid of an external magnetic field. For ions heavy enough to have low-lying D states, we can construct fine-structure qubits with the metastable fine-structure levels $(n-1)\mathrm{D}_{3/2}$ and $(n-1)\mathrm{D}_{5/2}$. For optical qubits, we let $n\mathrm{S}_{1/2}$ state be the computational ground state $|1\rangle$, and let $(n-1)\mathrm{D}_{5/2}$ state be the computational excited state $|0\rangle$.

In this thesis I take $^{40}\mathrm{Ca}^{+}$ ions to demonstrate quantum gate operations. Fig. 1.1 shows the energy levels of a $^{40}\mathrm{Ca}^{+}$ ion and the related transitions. The solid arrows indicate an electric dipole (E1) transition, while the dashed ones represent an electric quadrupole (E2) transition. The qubit states $|0\rangle$ and $|1\rangle$ are optically separated, so the single-qubit rotation can be done by simply driving the E2 transition [3]

$$\hat{V}(t) = \hbar\Omega(\hat{\sigma}^{+} + \hat{\sigma}^{-})\cos(\mathbf{k}\cdot\hat{\mathbf{r}} - \omega t), \tag{1.1}$$

where $\Omega = \frac{e}{2\hbar}\,|\langle 0|(\mathbf{E}_0\cdot\hat{\mathbf{r}})(\mathbf{k}\cdot\hat{\mathbf{r}})|1\rangle|$, with a laser field $\mathbf{E}(t) = \mathbf{E}_0\cos(\mathbf{k}\cdot\mathbf{r} - \omega t)$. State detection in this optical qubit is rather straightforward and can be performed with near-unity efficiency. The application of light driving the $4\mathrm{S}_{1/2} \rightarrow 4\mathrm{P}_{1/2}$ transition enables state-selective fluorescence; the ion will remain dark if the qubit is in $|0\rangle$ state. Since the $4\mathrm{P}$ states have an extremely short lifetime (about 7 ns) compared to the metastable $3\mathrm{D}$ states (about 1 sec), the measurement process can be very efficient. Also, the $4\mathrm{P}_{1/2}$ state cannot decay to the $3\mathrm{D}_{5/2}$ state according to the dipole selection rule $|j' - j| \leq 1$, meaning

doi:10.6342/NTU202203211

that the measurement process may be repeated many times because it does not change the qubit states $|0\rangle \leftrightarrow |1\rangle$.

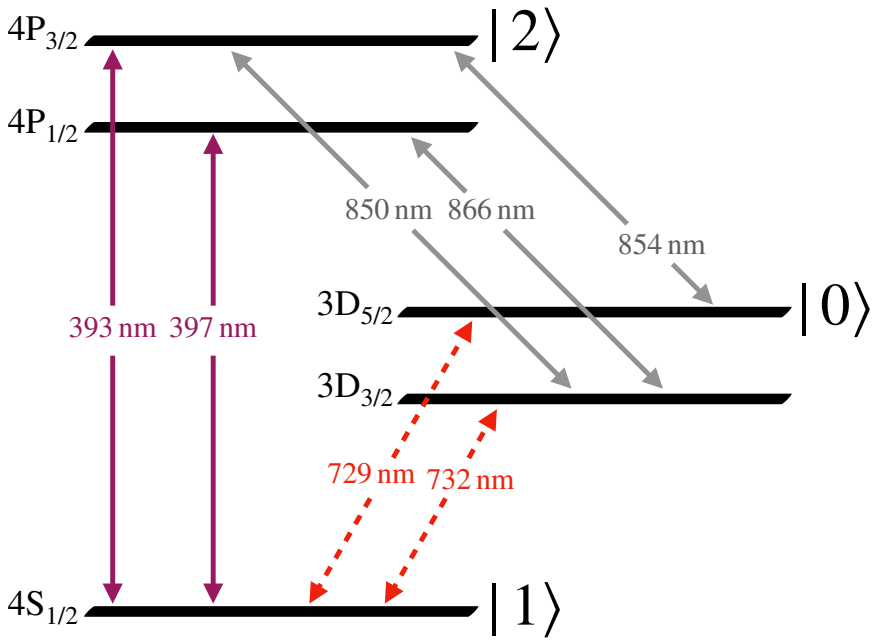

Figure 1.1: Level structure of a $^{40}Ca^{+}$ ion

1.2 Linear Paul Traps

Charged particles can be trapped by external electromagnetic fields. In Penning traps, a static magnetic field traps the ions in the radial directions, and meanwhile a static electric field provides confinement in the axial direction. However, since every ion in a Penning trap rotates at constant angular velocity, it is difficult to implement quantum gates using the ions' collective motional modes. On the other hand, Paul traps, which are capable of creating a nearly stationary array of ions with electric fields alone, have therefore been the main focus for researchers in trapped-ion quantum computing [4].

While, according to Gauss's law ($\nabla^2\Phi = 0$), there does not exist any static electric potential that can stably confine a charged particle, a time-varying electric potential may

doi:10.6342/NTU202203211

do the job. We consider an electric quadrupole field potential of the form

$$\Phi(x, y, z) = \frac{\phi_0}{2}\left(1 + \frac{x^2 - y^2}{d_0^2}\right), \tag{1.2}$$

where d_0 characterizes the size of the trap. Fig. 1.2a (adapted from [2]) illustrates a possible electrode structure that creates the quadratic potential. In an RF Paul trap, we use a time-dependent potential

$$\phi_0 = V_0 \cos(\Omega_T t) + U_0 \tag{1.3}$$

varying at a radio-frequency Ω_T. An ion lying in the x-y plane can therefore be trapped at the saddle points $z = 0$ dynamically, as depicted in Fig. 1.2b.

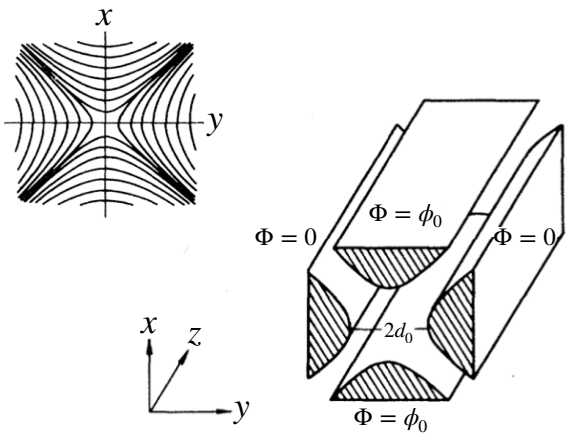

(a) Equipotential lines for Eq. (1.2) and the electrode structure

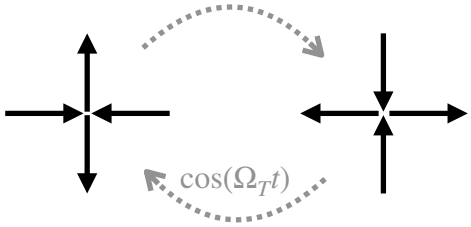

(b) Electric field lines in the x-y plane, varying at a radio-frequency Ω_T

Figure 1.2: Electric fields in an RF Paul trap

The equations of motion for an ion of mass M and charge $+e$ in the Paul trap are

doi:10.6342/NTU202203211

described by the Mathieu equation,

$$\begin{cases} \frac{d^2x}{d\xi^2} + [a + 2q\cos(2\xi)]x = 0 \\ \frac{d^2y}{d\xi^2} - [a + 2q\cos(2\xi)]y = 0 \end{cases}, \tag{1.4}$$

where $\xi = \frac{\Omega_T t}{2}$, $a = \frac{4eU_0}{M\Omega_T^2 d_0^2}$, and $q = \frac{2eV_0}{M\Omega_T^2 d_0^2}$. If the trap parameters are carefully designed such that $a \lesssim q \ll 1$, then the solution to Eq. (1.4) is simply a stable oscillation in the x-y plane [2]. Otherwise the amplitude grows exponentially, leading to an unstable motion. In this case the ion can never be trapped. Note that, theoretically, whether an ion can be trapped should be completely determined by the trap parameters, rather than its initial conditions (e.g., the initial velocity in the x-y plane).

The stable solution to Eq. (1.4) can be expanded to the first order of a and the second order of q, giving [5]

$$\begin{aligned} x(t) \approx x_0 \Bigg[& \cos(\omega_x t + \varphi_x) \left(1 + \frac{q}{2}\cos(\Omega_T t) + \frac{q^2}{32}\cos(2\Omega_T t)\right) \\ & + \beta_x \frac{q}{2} \sin(\omega_x t + \varphi_x)\sin(\Omega_T t)\Bigg], \end{aligned} \tag{1.5}$$

where $\omega_x = \beta_x \frac{\Omega_T}{2}$ and $\beta_x \approx \sqrt{a + \frac{q^2}{2}}$, and similarly for $y(t)$. We can identify the secular motion (oscillating at $\omega_{x,y}$) and the micromotion (oscillating at $n\Omega_T$), since we have $q \ll 1$ and $\omega_{x,y} \ll \Omega_T$. If the $\mathcal{O}(q)$ micromotion terms are neglected, the ion just moves as if it was confined in a *static harmonic pseudo-potential*

$$e\Phi(x, y, z) \to \frac{1}{2} M(\omega_x^2 x^2 + \omega_y^2 y^2). \tag{1.6}$$

Most of the work in trapped-ion quantum computing start with the assumption of the pseudo-potential. While this significantly simplifies our theoretical analyses and the gate design, micromotion errors will still compromise the actual gate performance in real-world experiments. In this thesis, the micromotion effects will instead be formally taken into ac-

doi:10.6342/NTU202203211

count.

Now that the ions are confined in the x- and y-directions, we can arrange them into a linear chain along the z-axis, by considering an additional weak harmonic pseudo-potential in the z-direction [6]. The equilibrium positions $z_i^{(0)}$ of the ions are found by minimizing the potential energy

$$V_{\text{pseudo}} = \sum_{i=1}^{N} \frac{1}{2} M\omega_z^2 z_i^2 + \sum_{i<j} \frac{e^2}{4\pi\epsilon_0} \frac{1}{|z_i - z_j|}. \tag{1.7}$$

Fig. 1.3 demonstrates the equilibrium positions of a 20-ion chain in a linear Paul trap, in the unit of a characteristic length scale $l = \sqrt[3]{\frac{e^2}{M\omega_z^2}}$. The ions moves collectively along the z-axis under small oscillations, which can be decomposed into the axial normal modes ω_p. These modes are obtained by diagonalizing the matrix

$$\mathrm{A}_{ij} = \left. \frac{\partial^2 V_{\text{pseudo}}}{\partial z_i \partial z_j} \right|_{\mathbf{z}^{(0)}}, \tag{1.8}$$

or by solving the eigenvalue equation

$$\mathrm{A}\mathbf{b}^{(p)} = M\omega_p^2 \mathbf{b}^{(p)}. \tag{1.9}$$

There are two specific modes that always exist in the mode spectrum, regardless of the ion number N. One is the center-of-mass (COM) mode, with mode frequency $\omega_p = \omega_z$ and mode coupling $\mathbf{b}^{(p)} \propto (1, 1, \ldots, 1)$. The other one is the breathing mode, with mode frequency $\omega_p = \sqrt{3}\omega_z$ and mode coupling $\mathbf{b}^{(p)} \propto (z_1^{(0)}, z_2^{(0)}, \ldots, z_N^{(0)})$. The quantization of these axial modes,

$$\hat{H} = \sum_{p=1}^{N} \hbar\omega_p \left(\hat{a}_p^\dagger \hat{a}_p + \frac{1}{2} \right), \tag{1.10}$$

provides phonons that can be used to design entangling gates.

doi:10.6342/NTU202203211

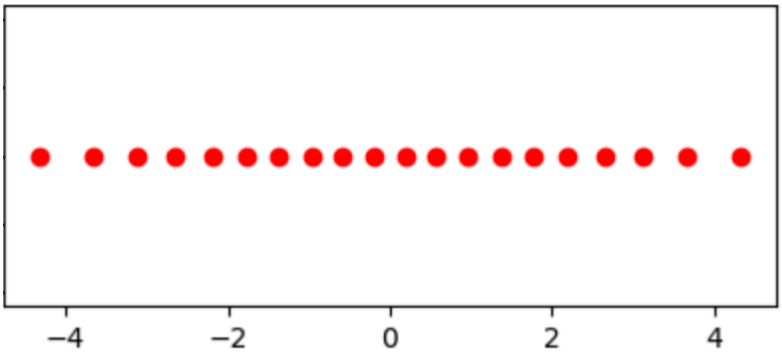

Figure 1.3: Ion chain of $N = 20$ in a linear RF Paul trap

1.3 Two-qubit Gates via Resolved Sideband Transitions

The Hamiltonian of a trapped ion interacting with light consists of a time-independent term $\hat{H}_0$ and a time-varying term $\hat{V}(t)$. If mode p can be clearly resolved from the normal mode spectrum, then we write

$$\begin{cases} \hat{H}_0 = \frac{1}{2}\hbar\omega_0\hat{\sigma}_z + \hbar\omega_p\left(\hat{a}^\dagger\hat{a} + \frac{1}{2}\right) \\ \hat{V}(t) = \hbar\Omega\left(\hat{\sigma}^+ + \hat{\sigma}^-\right)\cos(\mathbf{k}\cdot\hat{\mathbf{r}} - \omega t) \end{cases} . \tag{1.11}$$

In Eq. (1.11) it is assumed that only the pth motional mode is excited during the ion-light interaction. The spatial part in the cosine of $\hat{V}(t)$ can be expressed by

$$\mathbf{k}\cdot\hat{\mathbf{r}} = \mathbf{k}\cdot\mathbf{r}^{(0)} + \eta_p\left(\hat{a}^\dagger + \hat{a}\right), \tag{1.12}$$

where $\eta_p = k_z\sqrt{\frac{\hbar}{2M\omega_p}}$ is the Lamb-Dicke parameter. The constant term in Eq. (1.12) may be dropped because we are not studying the phase effects due to multiple light sources. Switching to the interaction picture with respect to $\hat{H}_0$, we obtain

$$\hat{H}_{\text{int}}(t) \approx \frac{1}{2}\hbar\Omega\hat{\sigma}^+ e^{i\eta_p\left(\hat{a}e^{-i\omega_p t} + \hat{a}^\dagger e^{i\omega_p t}\right)}e^{-i\delta t} + \text{H.c.} \tag{1.13}$$

under the rotating wave approximation (RWA), where $\delta = \omega - \omega_0$ is the detuning of the light.

doi:10.6342/NTU202203211

In order to simplify the interaction described by Eq. (1.13), experiments are usually conducted within the *Lamb-Dicke regime*. This regime is defined by

$$\langle \left[\eta_p(\hat{a}^\dagger + \hat{a})\right]^2 \rangle^{\frac{1}{2}} = \eta_p \sqrt{2n_p + 1} \ll 1. \tag{1.14}$$

In other words, in the Lamb-Dicke regime the displacement of an ion should be much smaller than the wavelength of the light, as indicated by this small deviation of $\mathbf{k} \cdot \hat{\mathbf{r}}$. Therefore, in experiments the Lamb-Dicke parameter has to be carefully designed such that

$$\eta_p^2 = \frac{\hbar^2 k_z^2 / 2M}{\hbar \omega_p} \ll 1. \tag{1.15}$$

In fact, Eq. (1.15) provides a physical interpretation of the Lamb-Dicke regime. Its denominator is the energy spacing of the pth-mode harmonic oscillator, and the numerator corresponds to the change in kinetic energy of the ion. Hence, Eq. (1.15) illustrates a *weak-excitation regime*, and transitions with $|\Delta n_p| > 1$ must be strongly suppressed.

For $\eta_p \ll 1$, Eq. (1.13) can be approximated by

$$\hat{H}_{\text{int}}(t) \approx \frac{1}{2}\hbar\Omega\hat{\sigma}^+ \left[1 + i\eta_p \left(\hat{a}e^{-i\omega_p t} + \hat{a}^\dagger e^{i\omega_p t}\right)\right] e^{-i\delta t} + \text{H.c.} \tag{1.16}$$

If we choose $\delta = 0$ and $\Omega \ll \omega_p$ (weak laser), the evolution will be dominated by the time-independent terms of $\hat{H}_{\text{int}}(t)$. This can be seen from the Magnus expansion of Eq. (1.16), where the zeroth-order term of the effective Hamiltonian corresponds to the RWA, and the first-order correction is the well-known Bloch-Siegert shift in qubit frequency [7]. The lowest-order correction in the spin-flip interaction therefore scales as $(\Omega/\omega_p)^2$, i.e.,

$$\hat{H}_{\text{eff}}(t) = \hat{H}_{\text{carr}} \left(1 + \mathcal{O}\left[(\Omega/\omega_p)^2\right]\right), \tag{1.17}$$

doi:10.6342/NTU202203211

where $\hat{H}_{\text{carr}}$ describes the so-called *carrier transitions* and is given by

$$\hat{H}_{\text{carr}} = \frac{1}{2}\hbar\Omega_{\text{carr}}(\hat{\sigma}^{+} + \hat{\sigma}^{-}). \tag{1.18}$$

In fact, the validity of Eq. (1.16) has been proved under the condition $(\eta_p\Omega/\sqrt{N}\omega_p)^2 \ll 1$, where the excitation of the other irrelevant phonon modes is highly suppressed [6]. Carrier transition only involves the internal states of an ion, so it is suitable for the implementation of a single-qubit rotation gate. Similarly, the so-called *blue sideband* or *red sideband* transitions will in turn dominate the evolution if we set $\delta = \pm\omega_p$ respectively. Their Hamiltonians are given by

$$\hat{H}_{\text{BSB}} = \frac{1}{2}\hbar\Omega_{\text{BSB}}(\hat{\sigma}^{+}\hat{a}^{\dagger} + \hat{\sigma}^{-}\hat{a}) \tag{1.19}$$

$$\hat{H}_{\text{RSB}} = \frac{1}{2}\hbar\Omega_{\text{RSB}}(\hat{\sigma}^{+}\hat{a} + \hat{\sigma}^{-}\hat{a}^{\dagger}). \tag{1.20}$$

The motional states change along with the internal states. In a classical picture these transitions are driven by some spin-dependent forces, leading to the spin-dependent change of motional states. As an enclosed area in phase space results in a quantum phase acquired by the ion (See Sec. 1.4), we can implement two-qubit entangling gates by triggering the sideband transitions, creating a specific quantum phase for every possible combination of the two qubit states, $|00\rangle$, $|01\rangle$, $|10\rangle$ and $|11\rangle$ (as in Eq. (1.21)).

The gate sets enabling universal quantum computation are usually composed of several single-qubit gates and a two-qubit gates that generates quantum entanglement. While from the algorithmic point of view it is convenient to include the CNOT gate in a gate set,

doi:10.6342/NTU202203211

a conditional phase gate such as

$$\exp\left(-i\frac{\pi}{4}\hat{\sigma}_1^z\hat{\sigma}_2^z\right) = \begin{pmatrix} \exp\left(-i\frac{\pi}{4}\right) & 0 & 0 & 0 \\ 0 & \exp\left(i\frac{\pi}{4}\right) & 0 & 0 \\ 0 & 0 & \exp\left(i\frac{\pi}{4}\right) & 0 \\ 0 & 0 & 0 & \exp\left(-i\frac{\pi}{4}\right) \end{pmatrix} \tag{1.21}$$

would be more feasible in realistic experiments. This conditional phase gate differs from the CNOT gate only by some single qubit rotations, and is also capable of creating entangled states.

Resolved sideband transition has been exploited since the very first two-qubit gate proposal [1]. However, its fatal disadvantages have also emerged these years. One disadvantage is the scaling problem. As the number of ions increases, the number of normal modes also increases, and it becomes more and more difficult to resolve a particular mode frequency from the nearly continuous frequency spectrum. Another disadvantage would be the long gate time. Although, when compared with superconducting qubits, trapped-ion qubits stand out in the coherence time ($\sim 10\,\mu$s vs. ~ 1 sec) and gate fidelity, the long gate time (~ 100 ns vs. $\sim 100\,\mu$s) [8] will still make it impossible to solve realistic problems within a reasonable computation time. While the state-of-the-art gate time for resolved sideband transitions are improved to $\sim 10\,\mu$s [4], it is still possible to further reduce the time down to $\sim 1\,\mu$s with *fast gates*. In this work, I will show that the scaling problem can be circumvented, and a significantly shortened gate time can be achieved with high fidelity using fast gates in a planar trapped-ion structure.

doi:10.6342/NTU202203211

1.4 Accumulation of Quantum Phases

A conditional phase gate like Eq. (1.21) results from a series of quantum dynamics that yield different phases for different states [3]. Suppose a quantum state $|\psi(t)\rangle$ acquires a phase ϕ by the end of the gate, i.e.,

$$|\psi(t+T_G)\rangle = e^{i\phi}|\psi(t)\rangle, \tag{1.22}$$

where T_G is the gate time. If we define

$$|\Psi(t)\rangle = e^{-if(t)}|\psi(t)\rangle \tag{1.23}$$

with $f(t+T_G) - f(t) = \phi$, then we obtain an invariant state $|\Psi(t+T_G)\rangle = |\Psi(t)\rangle$. By substituting Eq. (1.23) into the Schrödinger equation $i\hbar\frac{d}{dt}|\psi(t)\rangle = \hat{H}(t)|\psi(t)\rangle$, we can solve for the derivative of f,

$$\frac{df}{dt} = -\frac{1}{\hbar}\langle\psi(t)|\hat{H}(t)|\psi(t)\rangle + i\langle\Psi(t)|\frac{d}{dt}|\Psi(t)\rangle. \tag{1.24}$$

An integration over a gate time gives us the accumulated quantum phase,

$$\begin{aligned}\phi &= f(T_G) - f(0) \\ &= -\frac{1}{\hbar}\int_0^{T_G}\langle\psi(t)|\hat{H}(t)|\psi(t)\rangle dt + i\int_0^{T_G}\langle\Psi(t)|\frac{d}{dt}|\Psi(t)\rangle dt \\ &\equiv \phi_d + \phi_g.\end{aligned} \tag{1.25}$$

The first term ϕ_d contributes to the total phase through the average energy of the state and is called a *dynamic phase*. The second term ϕ_g is independent of the Hamiltonian that evolves the state. If we can parameterize $|\Psi(t)\rangle$ by a complex variable $\alpha = x + iy$, we then have a close contour representing its time evolution, as depicted in Fig. 1.4. This

doi:10.6342/NTU202203211

phase can be calculated in the parameter space by

$$\begin{aligned}\phi_g &= i\int_0^{T_G}\langle\Psi(t)|\frac{d}{dt}|\Psi(t)\rangle dt \\ &= i\oint_C \langle\alpha|\nabla|\alpha\rangle\cdot d\mathbf{r} \\ &= \int_S \mathbf{B}(\alpha)\cdot d\mathbf{S},\end{aligned} \tag{1.26}$$

where $\mathbf{r}=(x,y)$ and $\mathbf{B}(\alpha)\equiv\nabla\times(i\langle\alpha|\nabla|\alpha\rangle)$. From Eq. (1.26) we see that the phase ϕ_g only depends on the contour C and its enclosed area S, so it is called the *geometric phase*.

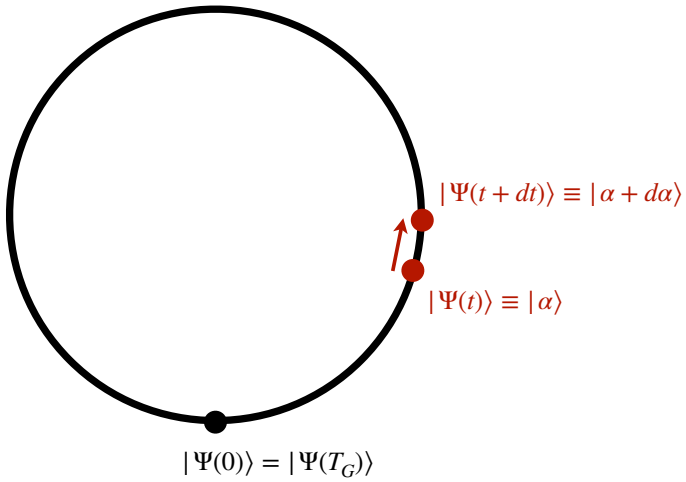

Figure 1.4: Evolution of $|\Psi(t)\rangle$ described by a contour in the α parameter space

In trapped-ion quantum quantum computing, spin-dependent forces are applied to drive harmonic oscillators (phonons). The quantum state can be described by a coherent state $|\alpha\rangle$. Using the fact that $\langle\alpha|\beta\rangle = \exp\left[-\frac{1}{2}\left(|\alpha|^2+|\beta|^2\right)+\alpha^*\beta\right]$ and keeping only the $\mathcal{O}(d\alpha)$ terms, we have

$$\begin{aligned}\langle\alpha|\nabla|\alpha\rangle\cdot d\mathbf{r} &= \langle\alpha|\alpha+d\alpha\rangle - \langle\alpha|\alpha\rangle \\ &= \frac{1}{2}\left(\alpha^* d\alpha - \alpha\, d\alpha^*\right) \\ &= (-iy, ix)\cdot d\mathbf{r}.\end{aligned} \tag{1.27}$$

doi:10.6342/NTU202203211

The effective magnetic field in this case is

$$\mathbf{B}(\alpha) = \nabla \times (y, -x, 0) = (0, 0, -2), \tag{1.28}$$

a constant vector field throughout the whole α parameter space. Since the dynamic phase is shown to be $\phi_d = 4S$ in this driven harmonic oscillator system [3], the total acquired quantum phase is

$$\begin{aligned} \phi &= \phi_d + \phi_g \\ &= 4S - 2S \\ &= 2S. \end{aligned} \tag{1.29}$$

From Eq. (1.29), we find that not only the geometric phase but also the entire quantum phase is proportional to the enclosed area S. Thus, the relative quantum phase between different two-qubit states will be proportional to the difference in their enclosed areas by the end of the gate. This important concept is utilized in the implementation of Eq. (1.21) and will be elaborated in Ch. 3.

doi:10.6342/NTU202203211

doi:10.6342/NTU202203211

Chapter 2

Planar Trapped-ion Systems

2.1 The Pseudo-potential Model

Following the study of a planar trapped-ion system by S.-T. Wang et al. [9], I present a more detailed analysis of the ion trap in this chapter. Consider an RF trapping potential $\Phi(t) = \phi_{\text{DC}} + \Phi_{\text{DC}} + \Phi_{\text{AC}}(t)$ satisfying Laplace's equation $\nabla^2\Phi(t) = 0$, where

$$\phi_{\text{DC}} = \frac{U_0}{d_0^2}\left[(1+\gamma)x^2 + (1-\gamma)y^2 - 2z^2\right] \tag{2.1}$$

$$\Phi_{\text{DC}}(\kappa) = \frac{U(\kappa)}{d_0^2}\left(x^2 + y^2 - 2z^2\right) \tag{2.2}$$

$$\Phi_{\text{AC}}(\kappa, t) = \frac{\kappa V_0 \cos(\Omega_T t)}{d_0^2}\left(x^2 + y^2 - 2z^2\right), \tag{2.3}$$

with $d_0 = 200\,\mu$m characterizing the size of the trap, a DC voltage $U_0 = -0.37\,$V, and an AC voltage $V_0 = 50\,$V. The AC potential oscillates at a radio-frequency $\Omega_T/2\pi = 100$ MHz. There are two additional trap parameters γ and κ introduced into the potential, corresponding to an actual shape of the trap (the electrodes). By setting $\gamma = 0.01$ and breaking the isotropy, the two-dimensional ion crystal cannot rotate freely in the x-y plane. This is to prevent the undesired rotational motions with respect to the trap center. The

doi:10.6342/NTU202203211

other parameter κ indicates a variable AC peak voltage κV_0 and a covarying DC voltage $U(\kappa) = \frac{e(1-\kappa^2)V_0^2}{Md_0^2\Omega_T^2}$, which is a crucial parameter in my gate proposal, as will be presented in Chapter 3. Yet in this chapter, all the calculation will be done with $\kappa = 1$.

The equations of motion of a single $^{40}Ca^+$ ion in the trap are described by the Mathieu equation,

$$\frac{d^2 r_\nu}{d\xi^2} + [a_\nu - 2q_\nu \cos(2\xi)]\, r_\nu = 0 \qquad \nu \in \{x, y, z\}, \tag{2.4}$$

where $\xi = \frac{\Omega_T t}{2}$. The coefficients a_ν and q_ν are designed such that $|a_\nu| < |q_\nu| \ll 1$, ensuring a stable ion trap. Their values are given by

$$\begin{aligned}
a_x(\kappa) &= \frac{8e\,[(1+\gamma)U_0 + U(\kappa)]}{Md_0^2\Omega_T^2} \ (\approx -4.57 \times 10^{-4} \text{ for } \kappa = 1) \\
a_y(\kappa) &= \frac{8e\,[(1-\gamma)U_0 + U(\kappa)]}{Md_0^2\Omega_T^2} \ (\approx -4.48 \times 10^{-4} \text{ for } \kappa = 1) \\
a_z(\kappa) &= \frac{-16e\,[U_0 + U(\kappa)]}{Md_0^2\Omega_T^2} \ (\approx 9.04 \times 10^{-4} \text{ for } \kappa = 1) \\
q_x(\kappa) = q_y(\kappa) &= -\frac{1}{2} q_z(\kappa) \equiv q(\kappa) = \frac{-4e\kappa V_0}{Md_0^2\Omega_T^2} \approx -0.031\kappa.
\end{aligned}$$

After neglecting the micromotion terms, we construct the static pseudo-potential by $\omega_\nu = \beta_\nu \frac{\Omega_T}{2}$, where $\beta_\nu \approx \sqrt{a_\nu + \frac{q_\nu^2}{2}}$, i.e.,

$$\sum_{i=1}^{N} e\Phi(x_i, y_i, z_i; t) \ \longrightarrow \ \frac{1}{2} M \sum_{i=1}^{N} \left(\omega_x^2 x_i^2 + \omega_y^2 y_i^2 + \omega_z^2 z_i^2\right). \tag{2.5}$$

The κ-dependence hence only appears in the axial trapping frequency $\omega_z(\kappa)$, leaving the other two trapping frequencies $\omega_{x,y}$ constant. In order to squeeze the ion crystal into a planar structure, we must apply a much stronger trapping potential in the axial (z) direction than in the radial (x-y) directions, so one has to carefully design a large enough ratio $\omega_z/\omega_{x,y}$. The ratio at which a 2D ion crystal breaks down into a 3D one is called the *critical ratio*. Earlier theoretical study on the critical ratio [10] shows that, in a similar system, $\omega_z/\omega_{x,y} \gtrsim 10$ could guarantee a planar crystal (exact values given in Table 2.2). The

doi:10.6342/NTU202203211

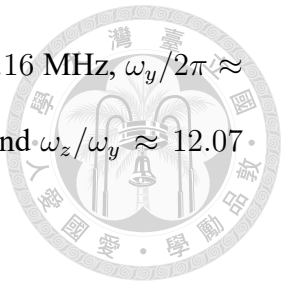

secular trap frequencies found in Eq. (2.5) take values of $\omega_x/2\pi \approx 0.16$ MHz, $\omega_y/2\pi \approx 0.22$ MHz, and $\omega_z(\kappa = 1)/2\pi \approx 2.63$ MHz, with $\omega_z/\omega_x \approx 16.65$ and $\omega_z/\omega_y \approx 12.07$ well beyond the critical ratio.

In this tight-trapping ($\omega_z/\omega_{x,y} \gtrsim 10$) regime, the ions' equilibrium positions lie in the plane $z = 0$, and we can find those positions $(x_i^{(0)}, y_i^{(0)}, 0)$ by minimizing the total potential energy

$$V_{\text{pseudo}} = \frac{1}{2}M\sum_{i=1}^{N}\left(\omega_x^2 x_i^2 + \omega_y^2 y_i^2\right) + \sum_{i<j}\frac{e^2}{4\pi\epsilon_0}\frac{1}{\sqrt{(x_i - x_j)^2 + (y_i - y_j)^2}}. \tag{2.6}$$

However, the dimension of the minimization problem grows rapidly as N increases, and the potential energy V_{pseudo} typically has multiple minima [10], both of which make the direct minimization almost impossible for a 2D Paul trap. A better way to obtain the equilibrium positions is to mimic a real cooling process, by molecular dynamics simulation with added dissipation [11]. Starting with an equilateral triangles in a 2D hexagonal structure, we can solve the equations of motion with a small friction $\eta < M\omega_{x,y}$,

$$M\ddot{\mathbf{r}} = -\frac{\partial V_{\text{pseudo}}}{\partial \mathbf{r}} - \eta\dot{\mathbf{r}}, \tag{2.7}$$

where $\mathbf{r} = (x_1, \ldots, x_N, y_1, \ldots, y_N)$. The equilibrium positions are hence given by $\mathbf{r}^{(0)} \equiv \mathbf{r}(t \to \infty)$. Fig. 2.1a demonstrates a hexagonal structure of 217 ions at $t = 0$, with ion spacing $a_0 = 14\,\mu$m. The equilibrium positions in Fig. 2.1b are found by solving Eq. (2.7) until a large enough $t = t_f$ (compared to a trap period $2\pi/\omega_{x,y}$) is reached. Such triangular lattice is also observed experimentally in recent years [12, 13]. In the simulation the final time is taken to be $t_f = 10^4 \cdot 2\pi/\omega_y$. While large t_f requires a long computation time, smaller t_f may lead to a set of non-equilibrium positions. It is hard to determine whether the ions sit right on their equilibrium positions simply by an inspection

doi:10.6342/NTU202203211

of Fig. 2.1b. However, this non-equilibrium can be seen from the divergence of average ion positions when solving for micromotion (See Sec. 2.2), or the emergence of imaginary frequencies in the radial normal modes (See Sec. 2.3).

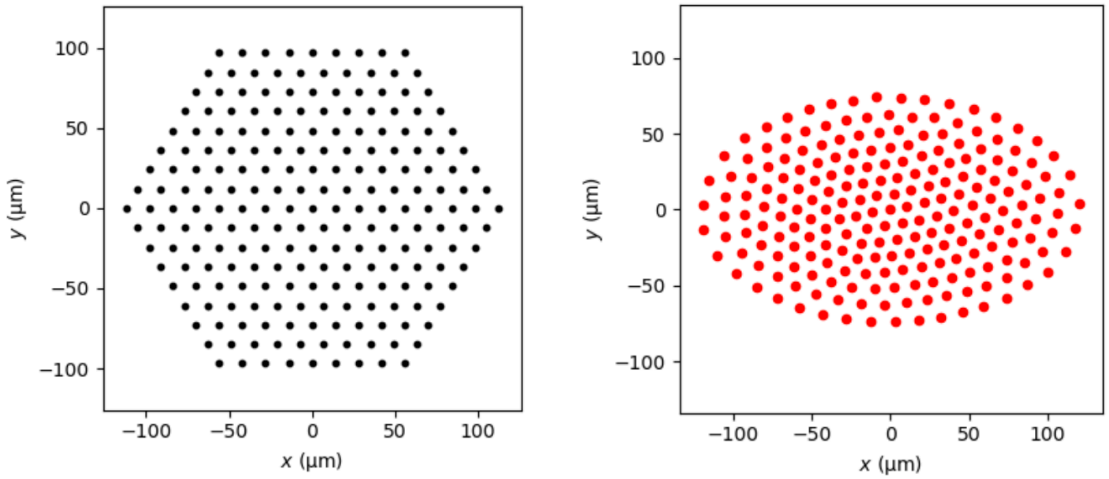

(a) Initial positions of the $^{40}Ca^{+}$ ions

(b) Equilibrium positions of the $^{40}Ca^{+}$ ions

Figure 2.1: A planar crystal of 217 ions in the pseudo-potential model

2.2 Micromotion and Average Positions of the Ions

The pseudo-potential model yields a set of equilibrium positions. However, it should be noted that the model is only an approximation of the real potential $\Phi(t)$ without micromotion. The ions cannot be lying at rest on their equilibrium positions, even if they are cooled down to an extremely low temperature. No matter how perfect the trap is, micromotion induced by the oscillating RF potential must always exist. In order to account for this intrinsic micromotion in the x-y plane, we have to recover the original time-varying potential energy,

$$V(t) = \sum_{i=1}^{N} e\Phi(x_i, y_i, 0; t) + V_C, \tag{2.8}$$

where $V_C = \sum_{i<j} \frac{e^2}{4\pi\epsilon_0} \frac{1}{\sqrt{(x_i-x_j)^2+(y_i-y_j)^2}}$ is the Coulomb potential energy. By expanding the Coulomb energy to the second order, we rewrite the two terms of Eq. (2.8) in quadratic

doi:10.6342/NTU202203211

forms (derived in App. A.1),

$$\sum_{i=1}^{N} e\Phi(x_i, y_i, 0; t) \;=\; \frac{1}{2}\mathbf{r}^{\mathrm{T}}\mathrm{M}_{\mathrm{DC}}\mathbf{r} + \frac{V_0}{d_0^2}\cos(\Omega_T t)\,\mathbf{r}^{\mathrm{T}}\mathbf{r} \tag{2.9}$$

$$V_C \;\approx\; \mathrm{g}^{\mathrm{T}}\mathbf{r} + \frac{1}{2}\mathbf{r}^{\mathrm{T}}\mathrm{M}_C\mathbf{r}. \tag{2.10}$$

The dependence on z_i is dropped in Eq. (2.8) because the three dimensions are decoupled in our RF potential, and the axial (z) Coulomb potential energy is also decoupled from the radial (x-y) terms under tight trapping, as will be shown in Sec. 2.3. The total potential energy thus takes the form

$$V(t) \;\approx\; \frac{1}{2}\mathbf{r}^{\mathrm{T}}(\mathrm{M}_{\mathrm{DC}} + \mathrm{M}_C)\mathbf{r} + \frac{V_0}{d_0^2}\cos(\Omega_T t)\,\mathbf{r}^{\mathrm{T}}\mathbf{r} + \mathbf{g}^{\mathrm{T}}\mathbf{r}. \tag{2.11}$$

The first term in Eq. (2.11) indicates a coupled interaction, which makes the coordinates $\mathbf{r} = (x_1, \ldots, x_N, y_1, \ldots, y_N)$ coupled together in the equations of motion. However, since the matrix $\mathrm{M}_{DC} + \mathrm{M}_C$ is symmetric, we can find an orthogonal transformation Q that diagonalizes it,

$$\Lambda = \mathrm{Q}^{\mathrm{T}}(\mathrm{M}_{\mathrm{DC}} + \mathrm{M}_C)\mathrm{Q}. \tag{2.12}$$

By casting the transformation $\mathbf{r} \equiv \mathrm{Q}\mathbf{s}$, Eq. (2.11) becomes

$$V(t) \;\approx\; \frac{1}{2}\mathbf{s}^{\mathrm{T}}\Lambda\mathbf{s} + \frac{V_0}{d_0^2}\cos(\Omega_T t)\,\mathbf{s}^{\mathrm{T}}\mathbf{s} + (\mathrm{Q}^{\mathrm{T}}\mathbf{g})^{\mathrm{T}}\mathbf{s}. \tag{2.13}$$

The equations of motion are now decoupled under the new normal coordinates and described by the inhomogeneous Mathieu equation,

$$\frac{d^2 s_i}{d\xi^2} + [a_i - 2q_i\cos(2\xi)]\,s_i = f_i, \tag{2.14}$$

where $a_i = \frac{4\Lambda_{ii}}{M\Omega_T^2}$, $q_i = \frac{-4eV_0}{Md_0^2\Omega_T^2} = q$, and $f_i = \frac{-4}{M\Omega_T^2}(\mathrm{Q}^{\mathrm{T}}\mathbf{g})_i$. After numerically solving Eq. (2.14) and transforming back into the ion coordinates (See App. A.2), we obtain the exact

doi:10.6342/NTU202203211

ion motion [14]

$$\mathbf{r}(t) = \mathbf{r}^{(0)} + \mathbf{r}^{(1)}\cos(\Omega_T t) + \mathbf{r}^{(2)}\cos(2\Omega_T t) + \cdots, \tag{2.15}$$

where $\mathbf{r}^{(0)}$ is the average positions of the ions, and $\mathbf{r}^{(n)}$ corresponds to the nth-order micromotion amplitudes. It should be noted that, while in Eq. (2.10), the expansion of Coulomb energy is evaluated at the equilibrium positions found in Sec. 2.1, the new average positions $\mathbf{r}^{(0)}$ in Eq. (2.15) would be slightly deviated. Therefore, a precise calculation of the exact ion motion should include an iteration process, by repeating Eq. (2.10) to Eq. (2.15) and updating the average positions. If the ions nearly reach equilibrium in the dynamical simulation of Sec. 2.1, the obtained equilibrium positions will lead to converged average positions $\mathbf{r}^{(0)}$ after several iterations, proving the consistency of the model. Hence, the divergence of $\mathbf{r}^{(0)}$ should be a hint of non-equilibrium in the previous dynamical simulation.

Fig. 2.2a demonstrates the equilibrium positions of 217 ions obtained by solving the equations of motion Eq. (2.7), and also the corrected average positions $\mathbf{r}^{(0)}$ after 100 iterations of Eq. (2.10) to Eq. (2.15). The average deviation of $\mathbf{r}^{(0)}$ is only $0.095\,\mu$m, showing nice convergence and consistency of the model. Fig. 2.2b plots the distribution of the nearest-neighbor (NN) distance of the ions. The NN distance of an ion ranges from $10.35\,\mu$m to $15.23\,\mu$m, with an average distance of $12.18\,\mu$m. From the numerical solution Eq. (2.15), we can find the relations between the micromotion amplitudes $\mathbf{r}^{(n)}$ and average positions $\mathbf{r}^{(0)}$. For example,

$$\mathbf{r}^{(1)} \approx -\frac{q}{2}\mathbf{r}^{(0)} \tag{2.16}$$

$$\mathbf{r}^{(2)} \approx \frac{q^2}{32}\mathbf{r}^{(0)}. \tag{2.17}$$

Since $|q| \approx 0.031 \ll 1$, it is sufficient to drop higher-order terms of $\mathcal{O}(q^3)$. The propor-

doi:10.6342/NTU202203211

tionality relations give us a simple picture of how the ions move under micromotion, i.e., a small *breathing oscillation* with respect to the trap center. Fig. 2.3 plots the micromotion amplitudes $|\mathbf{r}^{(1)}|$ of the 217 ions. It is clear that the outermost ions, having the largest ion spacing ($\simeq 15\,\mu$m), suffer from the severest micromotion ($|\mathbf{r}^{(1)}| \simeq 1.8\,\mu$m). Table 2.1 lists the shift of $\mathbf{r}^{(0)}$ obtained by the pseudo and exact potentials, the NN distance, and the micromotion amplitudes $|\mathbf{r}^{(1)}|$ for different number of ions. When we scale up the planar ion trap, the harmonic pseudo-potential forces the ion to form a more compact structure, resulting in the decrease of average NN distance. The micromotion, on the other hand, are getting larger because more ions are arranged farther away from the trap center.

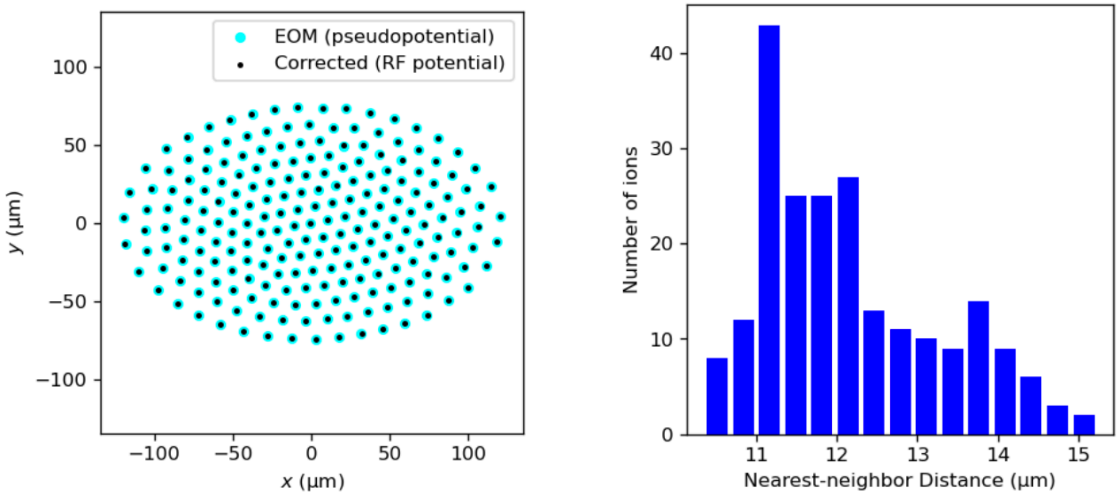

(a) $\mathbf{r}^{(0)}$ obtained by pseudo and exact potentials

(b) Distribution of the NN distance

Figure 2.2: Average positions and NN distance for a 217-ion system

Table 2.1: Scaling up N on ion spacing and micromotion amplitude (in μm)

N	7	19	37	61	91	127	169	217
Avg. shift of $\mathbf{r}^{(0)}$	0.03	0.04	0.06	0.09	0.07	0.08	0.09	0.10
Min. NN distance	17.1	14.9	13.4	12.8	12.1	11.6	11.2	10.4
Max. NN distance	18.9	17.5	16.7	16.2	15.8	15.2	15.0	15.2
Avg. NN distance	17.6	16.1	15.1	14.2	13.5	13.0	12.6	12.2
Min. micromotion amplitude	0.00	0.11	0.09	0.09	0.01	0.01	0.02	0.01
Max. micromotion amplitude	0.39	0.64	0.88	1.11	1.32	1.49	1.67	1.84

doi:10.6342/NTU202203211

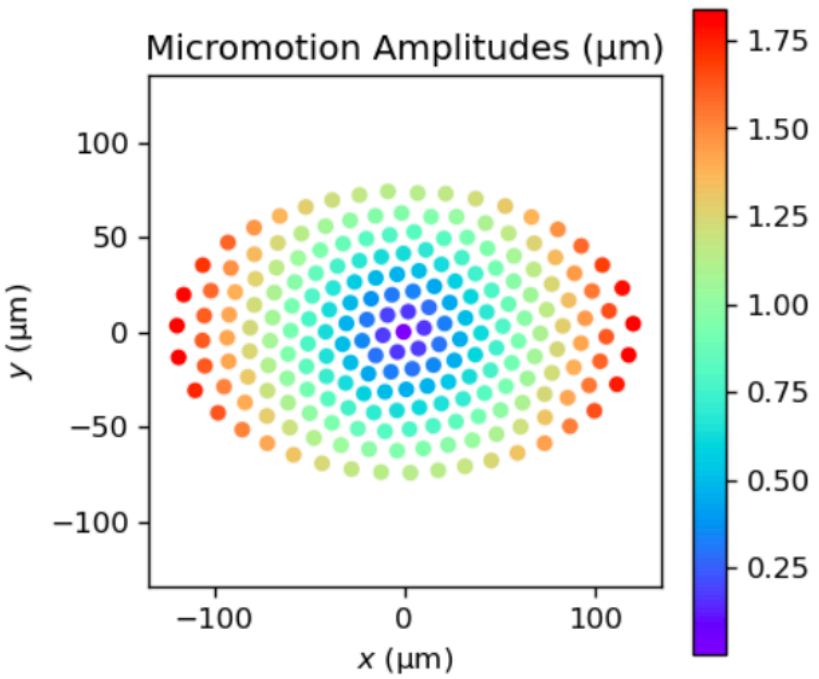

Figure 2.3: Micromotion amplitudes of a 217-ion system

2.3 Vibrational Normal Modes Without Micromotion

In this section, I elaborate the formalism of vibrational normal modes, *without* taking micromotion into account. The formalism of 1D normal modes derived in App. A.3 can be easily generalized and applied to our planar trapped-ion system. In the pseudo-potential model of Sec. 2.1, the total potential energy is

$$V_{\text{pseudo}} = \frac{1}{2}M\sum_{i=1}^{N}\left(\omega_x^2 x_i^2 + \omega_y^2 y_i^2 + \omega_z^2 z_i^2\right) + V_C, \tag{2.18}$$

where the Coulomb energy $V_C = \sum_{i<j}\frac{e^2}{4\pi\epsilon_0}\frac{1}{\sqrt{(x_i-x_j)^2+(y_i-y_j)^2+(z_i-z_j)^2}}$. According to the formalism of normal modes, we have to calculate the second derivatives of V_{pseudo}, evaluated at the equilibrium positions $\mathbf{r}^{(0)} = (x_1^{(0)},\ldots,x_N^{(0)},y_1^{(0)},\ldots,y_N^{(0)})$ and $\mathbf{z}^{(0)} = (z_1^{(0)},\ldots,z_N^{(0)})$. Since we have $z_i^{(0)} = 0$ in the tight trapping regime, it can be shown that

$$\left.\frac{\partial^2 V_C}{\partial x_i \partial z_j}\right|_{\mathbf{r}^{(0)},\mathbf{z}^{(0)}} = \left.\frac{\partial^2 V_C}{\partial y_i \partial z_j}\right|_{\mathbf{r}^{(0)},\mathbf{z}^{(0)}} = 0. \tag{2.19}$$

doi:10.6342/NTU202203211

The axial (z) energy terms are thus completely decoupled from the radial (x-y) terms. This explains why we can drop the z-dependence in Eq. (2.6) and Eq. (2.8) when searching for the equilibrium positions and calculating the in-plane motions.

The in-plane normal modes are obtained by diagonalizing the matrix

$$\mathrm{A} = \begin{pmatrix} M\omega_x^2\,\mathrm{I}_N & 0 \\ 0 & M\omega_y^2\,\mathrm{I}_N \end{pmatrix} + \mathrm{M}_C, \tag{2.20}$$

where I_N is the $N \times N$ identity matrix and M_C can be found in App. A.1. Fig. 2.4 plots the in-plane mode spectrum for a 37-ion system. The collective center-of-mass (COM) motions along the x- and y-directions can be easily identified from their mode couplings $\mathbf{b}^{(p)}$ respectively. The two COM mode frequencies are $\omega_p = \omega_x$ and $\omega_p = \omega_y$, as highlighted in Fig. 2.4. It should be noted that, if the calculation yields *imaginary* in-plane mode frequencies, this would be a warning of the non-equilibrium mentioned in Sec. 2.1. Imaginary mode frequencies come from the negative eigenvalues of A. In these cases, Eq. (A.25) no longer holds, which means there exist some displacements $\boldsymbol{\zeta}$ that could further decrease the potential energy, showing the equilibrium positions used are actually non-equilibrium.

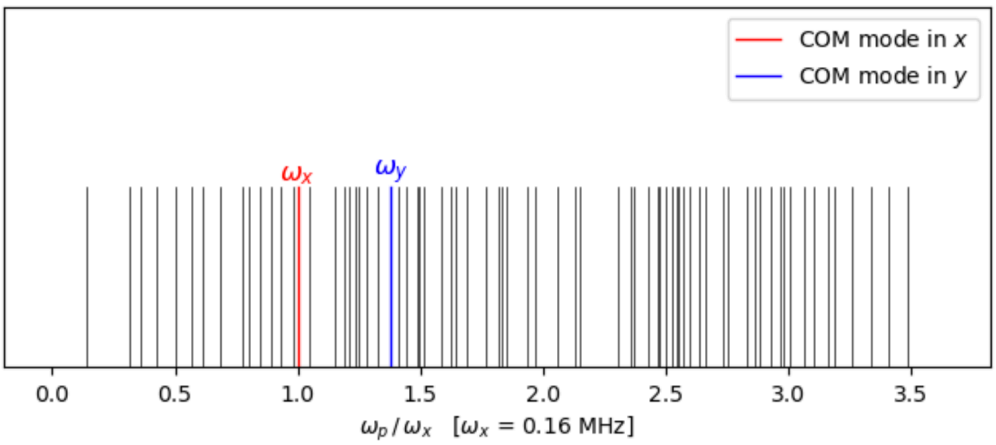

Figure 2.4: Radial (In-plane) normal mode spectrum for $N = 37$

doi:10.6342/NTU202203211

The out-of-plane normal modes are obtained by diagonalizing the matrix

$$\mathrm{A}_{ij} = M\omega_z^2\,\delta_{ij} + \left.\frac{\partial^2 V_C}{\partial z_i \partial z_j}\right|_{\mathbf{r}^{(0)},\,\mathbf{z}^{(0)}}, \tag{2.21}$$

with

$$\left.\frac{\partial^2 V_C}{\partial z_i^2}\right|_{\mathbf{r}^{(0)},\,\mathbf{z}^{(0)}} = \frac{-e^2}{4\pi\epsilon_0}\sum_{j\neq i}\frac{1}{\left[r_{ij}^{(0)}\right]^3} \tag{2.22}$$

$$\left.\frac{\partial^2 V_C}{\partial z_i \partial z_j}\right|_{\mathbf{r}^{(0)},\,\mathbf{z}^{(0)}} = \frac{-e^2}{4\pi\epsilon_0}\frac{-1}{\left[r_{ij}^{(0)}\right]^3}, \tag{2.23}$$

where $r_{ij}^{(0)} \equiv \sqrt{\left(x_i^{(0)} - x_j^{(0)}\right)^2 + \left(y_i^{(0)} - y_j^{(0)}\right)^2}$. Fig. 2.5 plots the out-of-plane mode spectrum for a 37-ion system. The COM mode in the z-direction has a frequency of $\omega_p = \omega_z$. It is found that the the largest frequency always corresponds to the COM mode, while the smallest frequency must correspond to the zigzag mode, as are highlighted in the spectrum. The zigzag motion can be visualized by its mode couplings $\mathbf{b}^{(p)}$, as plotted in Fig. 2.6a for a 7-ion system. Fig. 2.6b illustrates the out-of-plane zigzagging of these ions from a side view (along the y-axis).

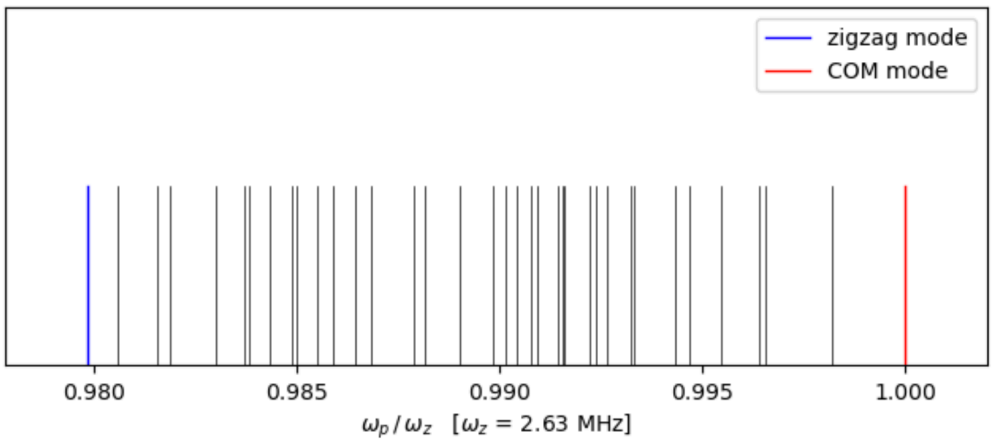

Figure 2.5: Axial (Out-of-plane) normal mode spectrum for $N = 37$

doi:10.6342/NTU202203211

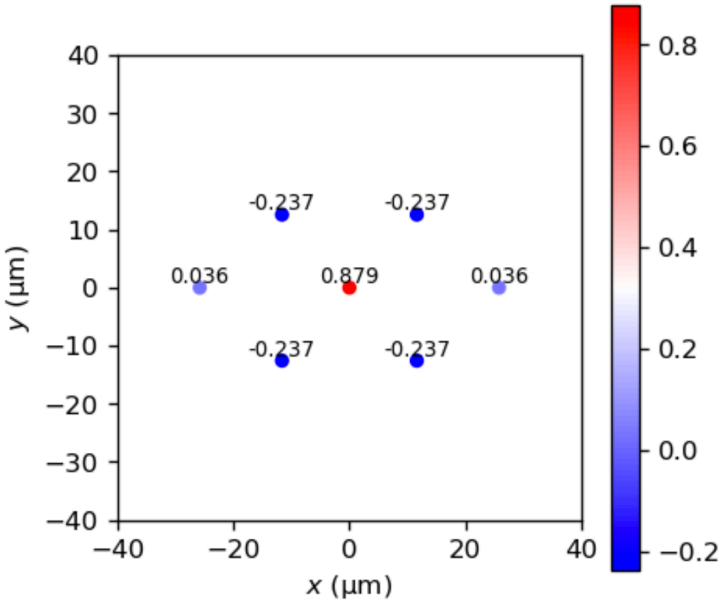

(a) The zigzag mode coupling $b_i^{(p)}$

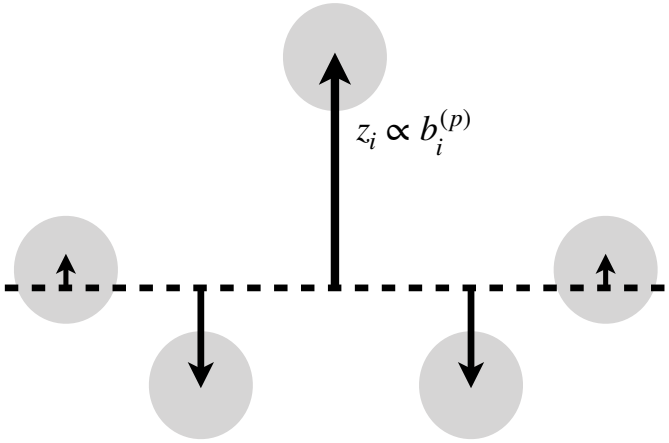

(b) Zigzagging as seen along the y-axis

Figure 2.6: Visualization of the zigzag mode for $N = 7$

doi:10.6342/NTU202203211

2.4 Impact of Micromotion

The presence of micromotion fundamentally prohibits the normal mode formalism. Since the ions oscillate intrinsically, we are unable to find the equilibrium positions where they can sit at rest, even under an extremely low temperature. However, in our planar trapped-ion system the ions are confined in a plane and their axial micromotion is highly suppressed. It is thus sufficient to study the axial normal modes with the pseudo-potential model at equilibrium positions $z_i^{(0)} = 0$, given the in-plane micromotion. To this end, Eq. (2.21) must be modified to account for the micromotion. Specifically, the second derivatives have to be evaluated at the ions' in-plane positions Eq. (2.15) for any time t, instead of the fixed equilibrium positions $\mathbf{r}^{(0)}$, i.e.,

$$\left.\frac{\partial^2 V_C}{\partial z_i^2}\right|_{\mathbf{r}(t),\,\mathbf{z}^{(0)}} = \frac{-e^2}{4\pi\epsilon_0}\sum_{j\neq i}\frac{1}{r_{ij}^3} \tag{2.24}$$

$$\left.\frac{\partial^2 V_C}{\partial z_i \partial z_j}\right|_{\mathbf{r}(t),\,\mathbf{z}^{(0)}} = \frac{-e^2}{4\pi\epsilon_0}\frac{-1}{r_{ij}^3}, \tag{2.25}$$

where $r_{ij} \equiv \sqrt{[x_i(t)-x_j(t)]^2 + [y_i(t)-y_j(t)]^2}$. Since the micromotion is inherently a small breathing oscillation, $r_i^{(n)} \propto q^n\, r_i^{(0)}$, we can expand r_{ij}^{-3} in terms of q,

$$\begin{aligned}
r_{ij}^{-3} &= \left[\left(\sum_{n=0}^{\infty}\left(x_i^{(n)} - x_j^{(n)}\right)\cos(n\Omega_T t)\right)^2 + \left(\sum_{n=0}^{\infty}\left(y_i^{(n)} - y_j^{(n)}\right)\cos(n\Omega_T t)\right)^2\right]^{-3/2} \\
&= \left(r_{ij}^{(0)}\right)^{-3}\left[1 - \frac{q}{2}\cos(\Omega_T t) + \frac{q^2}{32}\cos(2\Omega_T t) + \mathcal{O}(q^3)\right]^{-3} \\
&= \left(r_{ij}^{(0)}\right)^{-3}\left[1 + \frac{3q}{2}\cos(\Omega_T t) - \frac{3q^2}{32}\cos(2\Omega_T t) + \frac{3q^2}{2}\cos^2(\Omega_T t) + \mathcal{O}(q^3)\right] \\
&= \left(r_{ij}^{(0)}\right)^{-3}\left[1 + \frac{3q^2}{4} + \frac{3q}{2}\cos(\Omega_T t) + \frac{21q^2}{32}\cos(2\Omega_T t) + \mathcal{O}(q^3)\right].
\end{aligned}$$

The inclusion of micromotion simply results in a rescaling of the derivatives. The constant part of the potential energy constitutes the rescaled normal modes, which can be quantized

doi:10.6342/NTU202203211

as harmonic oscillators $\sum_{p=1}^{N} \hbar\omega'_p \hat{a}_p^\dagger \hat{a}_p$. The time-dependent parts can be viewed as a fast oscillating periodic perturbation ($\Omega_T \gg \omega_z$), which contributes to the mode transitions on the order of $q(\omega_z/\Omega_T)^2 \sim q^3$ and can be safely neglected [9]. The rescaled axial mode spectrum is obtained by diagonalizing A′, with

$$\mathrm{A}'_{ii} = M\omega_z^2 - \frac{e^2}{4\pi\epsilon_0} \sum_{j\neq i} \frac{1+\frac{3}{4}q^2}{\left(r_{ij}^{(0)}\right)^3} \tag{2.26}$$

$$\mathrm{A}'_{ij} = \frac{e^2}{4\pi\epsilon_0} \frac{1+\frac{3}{4}q^2}{\left(r_{ij}^{(0)}\right)^3}. \tag{2.27}$$

It is clear that $q \to 0$ takes us back to the previously discussed micromotion-free system.

Given the micromotion-free axial spectrum, we can analytically calculate the corrected one. Suppose we have two matrices A and A′ differing by a scaling parameter $\alpha = 1 + \frac{3}{4}q^2$, where

$$\mathrm{A} = M\omega_z^2\,\mathrm{I} + \mathrm{M}_C \tag{2.28}$$

$$\mathrm{A}' = M\omega_z^2\,\mathrm{I} + \alpha\mathrm{M}_C \tag{2.29}$$

and the eigenvalue problem $\mathrm{A}\mathbf{b} = \mu\mathbf{b}$ has been solved. We observe that M_C and A share the same eigenvectors, $\mathrm{M}_C\mathbf{b} = (\mu - M\omega_z^2)\mathbf{b}$. From this, we know that the inclusion of micromotion essentially leaves the axial mode structure unchanged,

$$\mathrm{A}'\,\mathbf{b} = \left[\alpha\mu + (1-\alpha)M\omega_z^2\right]\mathbf{b} \;\equiv\; \mu'\,\mathbf{b}, \tag{2.30}$$

while the mode frequencies are slightly reduced,

$$\omega'_p = \sqrt{\frac{\mu'}{M}} = \sqrt{\alpha\omega_p^2 - (\alpha-1)\omega_z^2}. \tag{2.31}$$

The corrected axial mode spectrum ω'_p obtained from direct diagonalization of A′ is shown in Fig. 2.7. Lower-frequency modes suffer from larger frequency shifts $\omega'_p - \omega_p$, while

doi:10.6342/NTU202203211

the COM mode is the only one that is kept invariant. However, the reduction in frequency ($\sim$ 10 Hz) is still very small compared with the mode frequencies ($\sim$ 1 MHz).

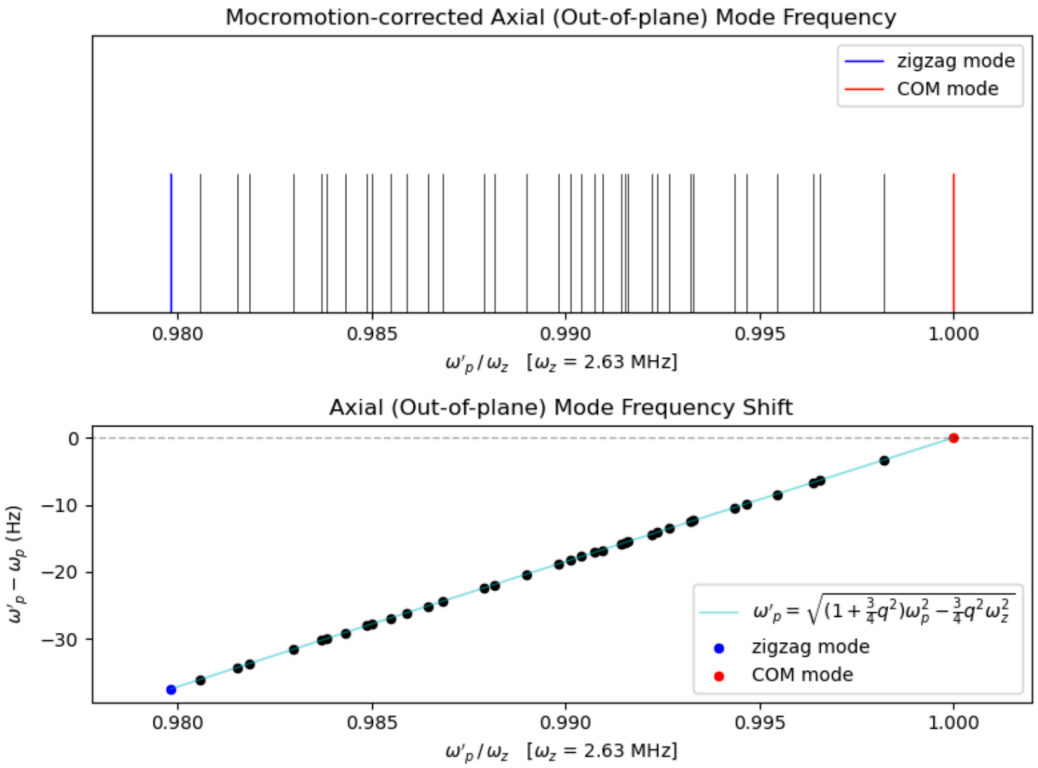

Figure 2.7: Corrected axial spectrum and frequency shifts for $N = 37$

In Sec. 2.3, the relation between imaginary radial frequency and non-equilibrium has been stated. Imaginary axial frequency, on the other hand, could also emerge as a result of the breakdown of our planar ion trap. Ions may move in an unbounded motion $e^{\pm i\omega_p t}$ in the z-direction for imaginary ω_p, inconsistent with the normal mode formalism. In this case we are no longer able to confine ions in a plane stably, where the 2D crystal effectively breaks down into a 3D crystal. Such breakdown may happen when ω_z is low enough compared to $\omega_{x,y}$, as mentioned in Sec. 2.1. Despite a weak axial trapping potential that could lead to the breakdown, micromotion might also lead to a destabilizing effect [15]. If micromotion becomes large (indicated by a large $|q|$), then μ'_p for the zigzag mode could be pushed to zero or even negative, giving rise to an imaginary frequency. The minimally required ω_z to create a 2D crystal, or the critical frequency, is therefore made

doi:10.6342/NTU202203211

higher by this intrinsic micromotion. In other words, a stable 2D trap designed without the consideration of micromotion could still be destabilized in real experiments. Nevertheless, a recent experiment disproves this micromotion-destabilized theory [13]. It is claimed that the pseudo-potential approach already provides a close approximation.

Since the zigzag mode has the lowest frequency, we can define the critical frequency by the minimal ω_z that pushes the zigzag-mode frequency to zero. Table 2.2 lists the critical axial trapping frequencies $\omega_z^{\min}$ and critical ratios $\omega_z^{\min}/\omega_x$ for different ion numbers. Due to the disagreement with experiments and the considerably small shifts in axial mode frequencies, the following theoretical analyses simply exploit the pseudo-potential approximation (ω_p), rather than the micromotion-destabilized theory (ω_p'). Apparently, we require higher ω_z to confine ions in a plane when there are more ions in the trap. The general rule of thumb of $\omega_z/\omega_{x,y} \gtrsim 10$ mentioned in Sec. 2.1 is justified here, at least still good enough for N as large as 217. In the next chapter, the decoupled axial modes are used to implement fast gates in this planar trapped-ion crystal.

Table 2.2: Critical ratios and critical axial trapping frequencies

N	7	19	37	61	91	127	169	217
$\omega_z^{\min}/\omega_x$	1.99	2.71	3.33	3.84	4.26	4.69	5.04	5.41
$\omega_z^{\min}/\omega_y$	1.44	1.96	2.41	2.78	3.09	3.40	3.65	3.92
$\omega_z^{\min}$ (MHz)	0.32	0.43	0.53	0.61	0.67	0.74	0.80	0.86

doi:10.6342/NTU202203211

doi:10.6342/NTU202203211

Chapter 3

Fast Gates in Planar Ion Crystals

3.1 Fast Gate Formalism

3.1.1 Spin-dependent Kicks From Ultrafast Laser Pulses

Consider a $^{40}Ca^{+}$ ion interacting with light of frequency ω, which is resonant to the $4S_{1/2} \leftrightarrow 4P_{3/2}$ transition shown in Fig. 1.1 and leaving the $|0\rangle$ state untouched. If the light is applied perpendicular to the ion plane (i.e., going in the z-direction), we can write down the total Hamiltonian as a sum of $\hat{H}_0$ and $\hat{V}(t)$, where

$$\begin{cases} \hat{H}_0 = 0\,|1\rangle\langle 1| + \hbar\omega|2\rangle\langle 2| + \hbar\omega_0|0\rangle\langle 0| \\ \hat{V}(t) = \hbar\Omega\cos(k\hat{z} - \omega t + \phi)\,(|1\rangle\langle 2| + |2\rangle\langle 1|) + \sum_{p=1}^{N}\hbar\omega_p\left(\hat{a}_p^\dagger\hat{a}_p + \frac{1}{2}\right) \end{cases} . \tag{3.1}$$

After switching to the interaction picture with respect to $\hat{H}_0$, we obtain the interaction Hamiltonian

$$\hat{H}_{\text{int}} \approx \frac{1}{2}\hbar\Omega\left[e^{-i(k\hat{z}+\phi)}|1\rangle\langle 2| + e^{i(k\hat{z}+\phi)}|2\rangle\langle 1|\right] + \sum_p \hbar\omega_p\left(\hat{a}_p^\dagger\hat{a}_p + \frac{1}{2}\right), \tag{3.2}$$

doi:10.6342/NTU202203211

where the counter-rotating terms are dropped according to RWA. For a single π pulse with duration τ, the evolution (up to a constant global phase) is given by

$$\hat{U}_k = \exp\left(-\frac{i\pi}{2}\left[e^{-i(k\hat{z}+\phi)}|1\rangle\langle 2| + e^{i(k\hat{z}+\phi)}|2\rangle\langle 1|\right] - i\sum_p \omega_p \hat{a}_p^\dagger \hat{a}_p \tau\right), \tag{3.3}$$

where the condition $\int_0^\tau \Omega dt = \pi$ has been imposed. Since an ultrafast laser ($\tau \sim 1\,\text{ps}$) is used in this work, we can neglect the contribution of the harmonic oscillators ($\omega_p \sim \omega_z \sim 1\,\text{MHz}$) in Eq. (3.3) as $\omega_p \tau \ll 1$. The fact that $\left[e^{-i(k\hat{z}+\phi)}|1\rangle\langle 2| + e^{i(k\hat{z}+\phi)}|2\rangle\langle 1|\right]^2 = |1\rangle\langle 1| + |2\rangle\langle 2|$ gives us an explicit form of Eq. (3.3),

$$\begin{aligned}\hat{U}_k &\approx \cos\left(\frac{\pi}{2}\right)(|1\rangle\langle 1| + |2\rangle\langle 2|) \\ &\quad - i\sin\left(\frac{\pi}{2}\right)\left[e^{-i(k\hat{z}+\phi)}|1\rangle\langle 2| + e^{i(k\hat{z}+\phi)}|2\rangle\langle 1|\right] + |0\rangle\langle 0| \\ &= -i\left[e^{-i(k\hat{z}+\phi)}|1\rangle\langle 2| + e^{i(k\hat{z}+\phi)}|2\rangle\langle 1|\right] + |0\rangle\langle 0|. \end{aligned} \tag{3.4}$$

In quantum mechanics we know that the operator $\exp\left(\frac{i\hat{p}\hat{x}}{\hbar}\right)$ acting on a state $|\psi\rangle$ shifts the state by p in the momentum space. Accordingly, Eq. (3.4) describes a so-called spin-dependent kick (SDK) [16, 17, 18, 19]: The ion gets excited to $|2\rangle$ and acquires a momentum $\hbar k$ in the z-direction if it is initially in the ground state $|1\rangle$, and vice versa. These absorption and stimulated emission processes are illustrated in Fig. 3.1a and 3.1b respectively.

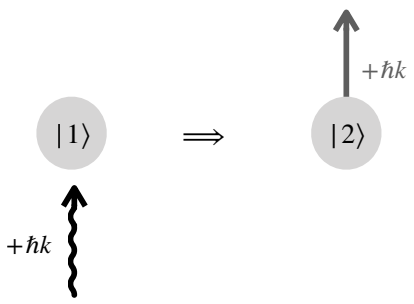

(a) Ion absorbing a photon and kicked by $+\hbar k$

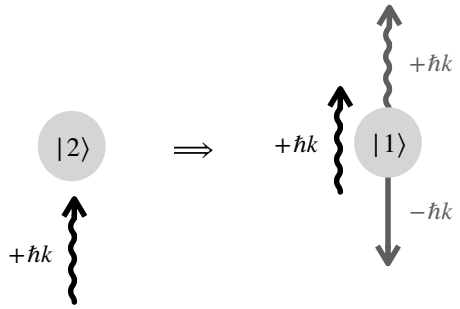

(b) Ion emitting a photon and kicked by $-\hbar k$

Figure 3.1: SDK from a π pulse in the z-direction

doi:10.6342/NTU202203211

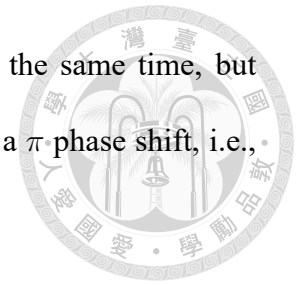

Now we apply two pulses going in the opposite directions at the same time, but slightly delay one of them such that one pulse hits the ion first with a π phase shift, i.e., $\phi_k - \phi_{-k} = \pm\pi$. The two possible scenarios are

$$\begin{cases} \hat{U}_{-k}\hat{U}_k &= e^{-2ik\hat{z}}|2\rangle\langle 2| + e^{2ik\hat{z}}|1\rangle\langle 1| + |0\rangle\langle 0| \\ \hat{U}_k\hat{U}_{-k} &= e^{2ik\hat{z}}|2\rangle\langle 2| + e^{-2ik\hat{z}}|1\rangle\langle 1| + |0\rangle\langle 0| \end{cases} . \tag{3.5}$$

The kicking of such pulse pairs does not result in any population transfer between the internal states. We can eliminate the $|2\rangle$ dependence and focus on the qubit subspace because only the qubit states $a|0\rangle + b|1\rangle$ will be involved effectively. Eq. (3.5) can thus be rewritten as a compact exponential form,

$$\hat{U}_s = e^{2isk\hat{z}\hat{n}}, \tag{3.6}$$

where $\hat{n} \equiv \frac{1}{2}(\hat{I} - \hat{\sigma}_z)$ and $\hat{n}|n\rangle = n|n\rangle$ for $n = 0, 1$. The parameter $s = \pm 1$ indicates which pulse in the pulse pair arrives first, as shown in Fig. 3.2. The two pulses should hit the ion one after the other, making two successive single-photon processes. In the following analysis, the two pulses are viewed as a simultaneous pulse pair at time t, by assuming a much smaller time delay between them compared to the laser repetition δt (See Fig. 3.3). Clearly Eq. (3.6) tells that a momentum $2s\hbar k$ is imparted to the ion if it is originally in the computational ground state $|1\rangle$, and it stays still if it is in the $|0\rangle$ state. The SDKs from such pulse pairs always keep the internal state of the ion; only the motional states will be changed after the kicks.

3.1.2 Fast Gate Schemes

By kicking two selected ions at time t_m, we obtain the unitary operator

$$\hat{U}^m_{\text{kick}} = e^{2is_m k(\hat{z}_1\hat{n}_1 + \hat{z}_2\hat{n}_2)}. \tag{3.7}$$

doi:10.6342/NTU202203211

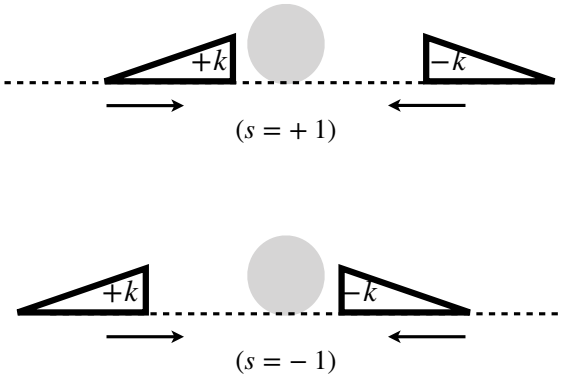

Figure 3.2: SDKs from a π pulse pair in the z-direction

A pulsed fast gate is comprised of several SDKs with interspersed free evolution of motional states during $\delta t_m \equiv t_m - t_{m-1}$ [20, 21],

$$\hat{U}_{\text{gate}} = \prod_{m=1}^{L} \hat{U}_{\text{kick}}^{m} \, e^{-i\sum_{p=1}^{N} \omega_p \hat{a}_p^\dagger \hat{a}_p \delta t_m}, \tag{3.8}$$

where L is the total number of SDKs, $t_1 \equiv 0$ and $\delta t_1 \equiv 0$. Fast gates are thus constructed by a pulse sequence

$$\mathbf{s} = [s_1,\, s_2,\, s_3,\, \ldots,\, s_{L-1},\, s_L]$$

$$\mathbf{t} = [t_1,\, t_2,\, t_3,\, \ldots,\, t_{L-1},\, t_L]$$

with a gate time defined by $T_G = t_L - t_1$, as shown in Fig. 3.3. In the ideal case, we could simply assume an infinite laser repetition rate, i.e., $s_m \in \mathbb{Z}$. A pulse group applied at time t_m would consist of $|s_m|$ instantaneous pulse pairs, and the sign of s_m is similarly defined as in Sec. 3.1.1. For the realistic case with a finite repetition rate, we still confine s_m to ± 1. The goal here is to minimize the infidelity of the gate with variables $\mathbf{s}$ and $\mathbf{t}$, making our fast gate $\hat{U}_{\text{gate}}$ approach the ideal conditional phase gate

$$\hat{U}_{\text{ideal}} = e^{-i\frac{\pi}{4}\hat{\sigma}_1^z \hat{\sigma}_2^z} \, e^{-iT_G \sum_{p=1}^{N} \omega_p \hat{a}_p^\dagger \hat{a}_p}, \tag{3.9}$$

doi:10.6342/NTU202203211

where all motional states are restored after the operation of this ideal gate.

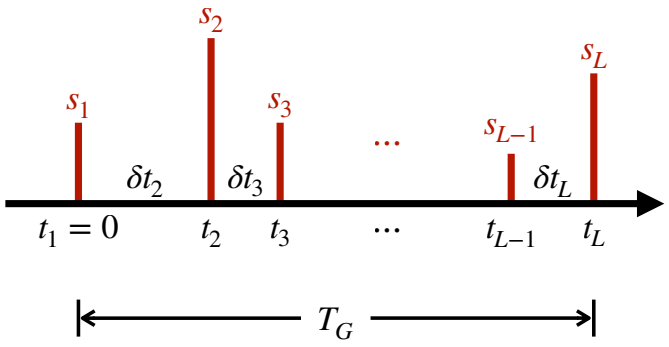

Figure 3.3: Fast gate scheme represented by a pulse sequence

Researchers in this field have proposed several gate schemes for the optimization [22, 23]. The García-Ripoll, Zoller and Cirac (GZC) scheme contains only four variables and is given by

$$\mathbf{s}_{\mathrm{GZC}} = [-2n,\ 3n,\ -2n,\ 2n,\ -3n,\ 2n]$$

$$\mathbf{t}_{\mathrm{GZC}} = [-\tau_1,\ -\tau_2,\ -\tau_3,\ \tau_3,\ \tau_2,\ \tau_1],$$

where the pulse timings have been shifted by $-\tau_1$ just to clearly demonstrate the antisymmetry of the scheme. The antisymmetry has been shown to be helpful for the restoration of motional modes [22]. A similar scheme called the fast robust antisymmetric gate (FRAG) scheme is given by

$$\mathbf{s}_{\mathrm{FRAG}} = [-n,\ 2n,\ -2n,\ 2n,\ -2n,\ n]$$

$$\mathbf{t}_{\mathrm{FRAG}} = [-\tau_1,\ -\tau_2,\ -\tau_3,\ \tau_3,\ \tau_2,\ \tau_1].$$

While the GZC and FRAG schemes are optimized under the assumption of an infinite

doi:10.6342/NTU202203211

laser repetition rate $f_{\text{rep}} = \infty$, Duan's scheme is designed for a finite f_{rep},

$$\begin{aligned}\mathbf{s}^{(1)} &= [+1, \ldots, +1, -1, \ldots, -1] \equiv [+n, -n] \\ \mathbf{t}^{(1)} &= [0, \tau_{\text{rep}}, 2\tau_{\text{rep}}, \ldots, (2n-1)\tau_{\text{rep}}],\end{aligned}$$

where $\tau_{\text{rep}} = 1/f_{\text{rep}}$ is the finite repetition period. Apparently, Duan's scheme also exploit the antisymmetry to achieve motional restoration. The only variable n is optimized such that the generated phase approaches $-\pi/4$. In case of poor motional restoration, higher-order Duan's schemes may be used to suppressed the motional errors [24]. The mth-order Duan's scheme can be obtained by the iterative exploitation of antisymmetry,

$$\begin{aligned}\mathbf{s}^{(m)} &= [\mathbf{s}^{(m-1)}, -\mathbf{s}^{(m-1)}] \\ \mathbf{t}^{(m)} &= [0, \tau_{\text{rep}}, 2\tau_{\text{rep}}, \ldots, (2^m n - 1)\tau_{\text{rep}}].\end{aligned}$$

3.1.3 Phase Space Trajectories

According to Eq. (A.29), the displacement $\hat{z}_i$ from equilibrium $z_i = 0$ can be expanded in terms of the axial normal modes,

$$\hat{z}_i = \sum_{p=1}^{N} \sqrt{\frac{\hbar}{2M\omega_p}} \left(\hat{a}_p + \hat{a}_p^\dagger\right) b_i^{(p)}. \tag{3.10}$$

The momentum kicks $\hat{U}_{\text{kick}}^m$ can hence be rewritten as a product of displacement operators for each mode p,

$$\begin{aligned}\hat{U}_{\text{kick}}^m |n_1 n_2\rangle &= \prod_{p=1}^{N} e^{2is_m\eta_p\left(b_1^{(p)}n_1 + b_2^{(p)}n_2\right)\left(\hat{a}_p + \hat{a}_p^\dagger\right)} |n_1 n_2\rangle \\ &= \prod_{p=1}^{N} \hat{D}_p(ic_{mp}) |n_1 n_2\rangle,\end{aligned} \tag{3.11}$$

doi:10.6342/NTU202203211

where $\hat{D}_p(\alpha_p) = \exp(\alpha_p \hat{a}_p^\dagger - \alpha_p^* \hat{a}_p)$ is the displacement operator for the pth motional mode, and $c_{mp} \equiv 2 s_m \eta_p \left(b_1^{(p)} n_1 + b_2^{(p)} n_2 \right)$. The fast gate unitary is thus rewritten as

$$\hat{U}_{\text{gate}} |n_1 n_2\rangle = \prod_{m=1}^{L} \prod_{p=1}^{N} \hat{D}_p(i c_{mp})\, e^{-i\omega_p \delta t_m \hat{a}_p^\dagger \hat{a}_p} |n_1 n_2\rangle. \tag{3.12}$$

In order to better understand the effects of $\hat{U}_{\text{gate}}$, we can consider a coherent state of the pth motional mode $|\alpha_p\rangle$ without loss of generality due to its overcompleteness. Using the identities $e^{-i\omega_p \delta t_m \hat{a}_p^\dagger \hat{a}_p} |\alpha_p\rangle = |\alpha_p e^{-i\omega_p \delta t_m}\rangle$ and $\hat{D}(\alpha)\hat{D}(\beta) = e^{i\text{Im}[\alpha\beta^*]} \hat{D}(\alpha+\beta)$, the new state after a free evolution during δt_m followed by a kick at t_m is

$$\begin{aligned}
\hat{D}_p(i c_{mp})\, e^{-i\omega_p \delta t_m \hat{a}_p^\dagger \hat{a}_p} |\alpha_p\rangle &= \hat{D}_p(i c_{mp}) \hat{D}_p(\alpha_p e^{-i\omega_p \delta t_m}) |0\rangle \\
&= e^{i\text{Im}\left[(i c_{mp})(\alpha_p^* e^{i\omega_p \delta t_m})\right]} \hat{D}_p(i c_{mp} + \alpha_p e^{-i\omega_p \delta t_m}) |0\rangle \\
&= e^{i\text{Re}\left[\alpha_p c_{mp} e^{-i\omega_p \delta t_m}\right]} \left| \alpha_p e^{-i\omega_p \delta t_m} + i c_{mp} \right\rangle.
\end{aligned} \tag{3.13}$$

These SDKs can be visualized in the phase space of every motional mode p. By definition, the dimensionless displacement and momentum for the coherent state $|\alpha_p\rangle$ are

$$\begin{cases} \langle X_p \rangle = \langle \alpha_p | \frac{1}{\sqrt{2}} \left(\hat{a}_p + \hat{a}_p^\dagger \right) |\alpha_p\rangle = \frac{1}{\sqrt{2}} \left(\alpha_p + \alpha_p^* \right) = \sqrt{2}\, \text{Re}[\alpha_p] \\ \langle P_p \rangle = \langle \alpha_p | \frac{-i}{\sqrt{2}} \left(\hat{a}_p - \hat{a}_p^\dagger \right) |\alpha_p\rangle = \frac{-i}{\sqrt{2}} \left(\alpha_p - \alpha_p^* \right) = \sqrt{2}\, \text{Im}[\alpha_p] \end{cases}.$$

Fig. 3.4a demonstrates a typical phase space trajectory according to Eq. (3.13), starting from a coherent state $|\alpha_p\rangle$ at time t_{m-1}. The state first goes through a free evolution within δt_m, and then receives an instantaneous kick $i c_{mp}$ at time t_m. The trajectory in Fig. 3.4a can be further simplified by switching to the interaction picture with respect to the pth motional mode, i.e., $|\alpha_p'\rangle \equiv e^{i\omega_p \hat{a}_p^\dagger \hat{a}_p t} |\alpha_p\rangle$. Those free evolution segments will be gone in the co-rotating frame. In this rotating phase space, the dimensionless displacement and momentum are defined by

$$\begin{cases} \langle X_p' \rangle = \langle \alpha_p' | \frac{1}{\sqrt{2}} \left(\hat{a}_p + \hat{a}_p^\dagger \right) |\alpha_p'\rangle = \frac{1}{\sqrt{2}} \left(\alpha_p e^{i\omega_p t} + \alpha_p^* e^{-i\omega_p t} \right) = \sqrt{2}\, \text{Re}[\alpha_p e^{i\omega_p t}] \\ \langle P_p' \rangle = \langle \alpha_p' | \frac{-i}{\sqrt{2}} \left(\hat{a}_p - \hat{a}_p^\dagger \right) |\alpha_p'\rangle = \frac{-i}{\sqrt{2}} \left(\alpha_p e^{i\omega_p t} - \alpha_p^* e^{-i\omega_p t} \right) = \sqrt{2}\, \text{Im}[\alpha_p e^{i\omega_p t}] \end{cases},$$

doi:10.6342/NTU202203211

where the identity $e^{-i\omega_p \hat{a}_p^\dagger \hat{a}_p t}\, \hat{a}_p\, e^{i\omega_p \hat{a}_p^\dagger \hat{a}_p t} = \hat{a}_p e^{i\omega_p t}$ has been used. Fig. 3.4b plots a typical trajectory in rotating phase space, starting from the state $|\alpha_p'\rangle = |0\rangle$. At time $t_1 = 0$, the ion receives a kick $ic_{1p}e^{i\omega_p t_1}$ and reaches the state $|\alpha_p'(t_1)\rangle$. A subsequent free evolution within δt_2 leaves the state unchanged in the rotating phase space, while an angle $\Delta\theta = \omega_p t_2 - \omega_p t_1 = \omega_p \delta t_2$ is formed defining the direction of the next kick. A following kick $ic_{2p}e^{i\omega_p t_2}$ at time t_2 then brings the state to $|\alpha_p'(t_2)\rangle$. In Fig. 3.4b it is assumed that $c_{1p} > 0$ and $c_{2p} < 0$. If c_{2p} is positive, then the kick at t_2 would instead point in the upper left direction.

3.1.4 Gate Fidelity

From Eq. (3.13), we can derive the change of an initial state $|\alpha_p\rangle$ by the end of a fast gate (See App. B.1). According to Eq. (B.31), the acquired quantum phase from the pth motional mode after a whole series of kicks is

$$\begin{aligned}\xi_p &= \mathrm{Re}\left[\alpha_p \sum_{m=1}^{L} c_{mp} e^{-i\omega_p t_m}\right] + 4\eta_p^2 \left(b_1^{(p)} n_1 + b_2^{(p)} n_2\right)^2 \sum_{m=2}^{L} \sum_{l=1}^{m-1} s_m s_l \sin[\omega_p (t_m - t_l)] \\ &\equiv \xi_p' + \xi_p''. \end{aligned} \tag{3.14}$$

Now if we define a *motional displacement*

$$C_p \equiv i \sum_{m=1}^{L} c_{mp} e^{i\omega_p t_m} = 2i\eta_p \left(b_1^{(p)} n_1 + b_2^{(p)} n_2\right) \sum_{m=1}^{L} s_m e^{i\omega_p t_m}, \tag{3.15}$$

then the coherent state by the end of the fast gate takes the form

$$\begin{aligned} |\tilde{\alpha}_p\rangle &= e^{-i\omega_p T_G \hat{a}_p^\dagger \hat{a}_p} |C_p + \alpha_p\rangle \\ &= e^{-i\omega_p T_G \hat{a}_p^\dagger \hat{a}_p} \hat{D}_p(C_p) \hat{D}_p(\alpha_p) e^{-i\mathrm{Im}\left[C_p \alpha_p^*\right]} |0\rangle \\ &= e^{-i\omega_p T_G \hat{a}_p^\dagger \hat{a}_p} \hat{D}_p(C_p) e^{-i\xi_p'} |\alpha_p\rangle. \end{aligned} \tag{3.16}$$

doi:10.6342/NTU202203211

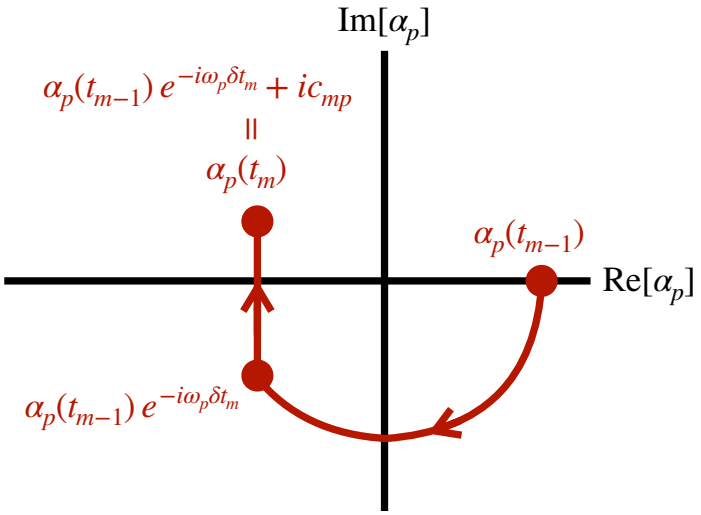

(a) Phase space trajectory for a free evolution within δt_m and a kick at t_m

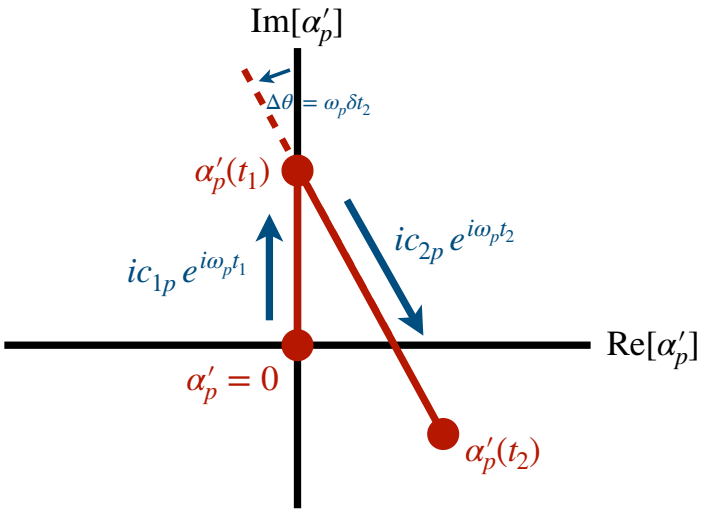

(b) Trajectory in the rotating phase space from t_1 to t_2

Figure 3.4: Visualization of SDKs in the phase space of the pth motional mode

doi:10.6342/NTU202203211

Using the definition of $n_i = \frac{1}{2}(1-\sigma_i^z)$ and dropping the global phases without internal state dependence, we obtain a formula for a fast gate acting on the total coherent state $|\alpha\rangle \equiv \prod_p |\alpha_p\rangle$, i.e., expressing Eq. (3.12) as

$$\begin{aligned}\hat{U}_{\text{gate}}|\sigma_1^z\sigma_2^z\rangle|\alpha\rangle &= e^{i\Theta\sigma_1^z\sigma_2^z}\, e^{i\theta_1\sigma_1^z}\, e^{i\theta_2\sigma_2^z}\, e^{\sum_p i\xi_p'}\, |\sigma_1^z\sigma_2^z\rangle|\tilde{\alpha}\rangle \\ &= e^{i\Theta\sigma_1^z\sigma_2^z}\, e^{i\theta_1\sigma_1^z}\, e^{i\theta_2\sigma_2^z}\, e^{-iT_G\sum_p \omega_p \hat{a}_p^\dagger \hat{a}_p} \left[\prod_{p=1}^{N} \hat{D}_p(C_p)\right] |\sigma_1^z\sigma_2^z\rangle|\alpha\rangle, \end{aligned} \tag{3.17}$$

where

$$\Theta = \sum_{p=1}^{N} 2\eta_p^2 b_1^{(p)} b_2^{(p)} \sum_{m=2}^{L}\sum_{l=1}^{m-1} s_m s_l \sin[\omega_p(t_m - t_l)] \tag{3.18}$$

is the conditional phase that will be optimized to $-\pi/4$, and

$$\begin{cases} \theta_1 = \sum_{p=1}^{N} -2\eta_p^2 b_1^{(p)}\left(b_1^{(p)} + b_2^{(p)}\right) \sum_{m=2}^{L}\sum_{l=1}^{m-1} s_m s_l \sin[\omega_p(t_m - t_l)] \\ \theta_2 = \sum_{p=1}^{N} -2\eta_p^2 b_2^{(p)}\left(b_1^{(p)} + b_2^{(p)}\right) \sum_{m=2}^{L}\sum_{l=1}^{m-1} s_m s_l \sin[\omega_p(t_m - t_l)] \end{cases} \tag{3.19}$$

are the phases associated with individual spins σ_i^z. Since the undesired θ_1 and θ_2 can be corrected by additional single-qubit rotations, we can simply drop these two terms and write down the explicit fast gate unitary operator,

$$\hat{U}_{\text{gate}} \rightarrow e^{i\Theta\hat{\sigma}_1^z\hat{\sigma}_2^z}\, e^{-iT_G\sum_p \omega_p \hat{a}_p^\dagger \hat{a}_p} \prod_{p=1}^{N} \hat{D}_p(C_p). \tag{3.20}$$

Before diving into the derivation of fast gate fidelity, we shall compare Eq. (3.20) with Eq. (3.9) first to see the big picture. Given a pulse sequence **s** and **t**, $\hat{U}_{\text{gate}}$ approaches the ideal conditional phase gate if $\Theta \rightarrow -\pi/4$ and $C_p \rightarrow 0$ for all p. In other words, a proper series of SDKs in phase spaces should encircle proper areas corresponding to the $-\pi/4$ quantum phase. Meanwhile, the kicks should also bring the motional states back to where they start, achieving a closed phase-space trajectory and hence motional restoration.

In order to measure the fidelity of a fast gate, we calculate the overlap $\left|\langle \hat{U}_{\text{ideal}}^\dagger \hat{U}_{\text{gate}}\rangle\right|^2$. As the free evolution terms are canceled out in the calculation of overlapping, we may

doi:10.6342/NTU202203211

redefine

$$\hat{U}_{\text{ideal}}|n_1 n_2\rangle \equiv e^{-i\frac{\pi}{4}\sigma_1^z\sigma_2^z}|n_1 n_2\rangle \tag{3.21}$$

$$\hat{U}_{\text{gate}}|n_1 n_2\rangle \equiv e^{i\Theta\sigma_1^z\sigma_2^z}\prod_{p=1}^{N}\hat{D}_p\left(\beta_1^{(p)}n_1+\beta_2^{(p)}n_2\right)|n_1 n_2\rangle, \tag{3.22}$$

with $\beta_j^{(p)} = 2i\eta_p b_j^{(p)}\sum_m s_m e^{i\omega_p t_m}$. The gate fidelity for an initial two-qubit state $|\psi_0\rangle$ is thus defined by

$$F \equiv \langle\psi_0|\hat{U}_{\text{ideal}}^{\dagger}\,\hat{\rho}\,\hat{U}_{\text{ideal}}|\psi_0\rangle, \tag{3.23}$$

where $\hat{\rho} = \text{Tr}_{\text{m}}\left[\hat{U}_{\text{gate}}\left(|\psi_0\rangle\langle\psi_0|\otimes\hat{\rho}_{\text{th}}\right)\hat{U}_{\text{gate}}^{\dagger}\right]$ traces partially over all motional modes, and $\hat{\rho}_{\text{th}} = \prod_p \hat{\rho}_{\text{th}}^{(p)}$ is an initial thermal product state. While it is possible to calculate the average fidelity over all initial two-qubit state $|\psi_0\rangle = a|00\rangle + b|01\rangle + c|10\rangle + d|11\rangle$, a specific state is used here,

$$|\psi_0\rangle = |+\rangle|+\rangle = \frac{1}{2}\left(|00\rangle+|01\rangle+|10\rangle+|11\rangle\right), \tag{3.24}$$

since it is shown to yield the worst-case fidelity [25]. The average fidelity will always exceeds that worst-case fidelity. After a straightforward derivation provided in App. B.2, we obtain the gate fidelity

$$F = \frac{1}{8}\left[2+\Gamma_+ +\Gamma_- - 2\left(\Gamma_1+\Gamma_2\right)\sin(2\Theta)\right], \tag{3.25}$$

where

$$\begin{cases}\Gamma_j = \exp\left[-\sum_p\left|\beta_j^{(p)}\right|^2\left(\bar{n}_p+\frac{1}{2}\right)\right]\\ \Gamma_\pm = \exp\left[-\sum_p\left|\beta_1^{(p)}\pm\beta_2^{(p)}\right|^2\left(\bar{n}_p+\frac{1}{2}\right)\right]\end{cases} \tag{3.26}$$

and $\bar{n}_p$ is the initial mean phonon number for the pth axial mode. In the following simulation, the initial mean phonon occupation is set to be $\bar{n}_p = 0.1$ for all modes. Ideally we would have $\Theta = -\pi/4$ and $\beta_j^{(p)} \propto C_p \propto \sum_m s_m e^{i\omega_p t_m} = 0$, yielding the highest possible value of $F = 1$.

doi:10.6342/NTU202203211

3.2 A Micromotion-tolerant Scheme

3.2.1 Stroboscopic Fast Gates

Although the out-of-plane micromotion in a planar trapped-ion crystal can be neglected, the in-plane micromotion may still lead to a terrible gate fidelity. Simply put, a target ion could receive different light intensities at different times given a finite laser profile centered at its average position $\mathbf{r}^{(0)}$, since the ion is never stationary in the plane. Micromotion thus brings about an effect of imperfect π pulses and hinders the actual gate performance. In light of this, I propose a pulsed fast gate scheme, which is insensitive to the in-plane micromotion of trapped ions. First of all, we observe that Eq. (2.15) provides a deterministic description of micromotion, with a fundamental frequency of Ω_T. Secondly, this periodicity tells that the ions always swing back to their average positions $\mathbf{r}^{(0)}$ whenever $\cos(\Omega_T t) = 0$, i.e., with a period

$$\tau_{\text{rep}} = \frac{m\pi}{\Omega_T} \quad (m \in \mathbb{N}), \tag{3.27}$$

corresponding to a vanishing AC voltage in Eq. (2.3). To circumvent the micromotion problem, we only have to send pulses as soon as $\Phi_{\text{AC}} = 0$ at a fixed laser repetition rate

$$\omega_{\text{rep}} = \frac{2\pi}{\tau_{\text{rep}}} = \frac{2}{m}\Omega_T \quad (m \in \mathbb{N}). \tag{3.28}$$

Such a stroboscopic pulsing scheme guarantees that the pulses always meet the ions at their average positions. In this work the largest possible rate $\omega_{\text{rep}} = 2\Omega_T = 2\pi \times 200\,\text{MHz}$ is used in order to obtain the fastest possible gates.

Since the required laser repetition rate is a fixed finite number, Duan's fast gate scheme would be a good choice. In Duan's scheme, there is only one SDK at a time

doi:10.6342/NTU202203211

($s = \pm 1$), and the kicking operator Eq. (3.7) can be expressed in the computational basis by

$$
\begin{aligned}
e^{2isk(\hat{z}_1\hat{n}_1+\hat{z}_2\hat{n}_2)} &\propto e^{-isk(\hat{z}_1\hat{\sigma}_1^z+\hat{z}_2\hat{\sigma}_2^z)} \\
&= \begin{pmatrix} e^{-isk(\hat{z}_1+\hat{z}_2)} & & & \\ & e^{-isk(\hat{z}_1-\hat{z}_2)} & & \\ & & e^{isk(\hat{z}_1-\hat{z}_2)} & \\ & & & e^{isk(\hat{z}_1+\hat{z}_2)} \end{pmatrix},
\end{aligned} \tag{3.29}
$$

where a global phase without internal state dependence is dropped. The motional states are kicked in the phase space by

$$
\begin{cases} e^{\pm isk(\hat{z}_1+\hat{z}_2)} = \prod_p \hat{D}_p\left[\pm is\eta_p\left(b_1^{(p)} + b_2^{(p)}\right)\right] \\ e^{\pm isk(\hat{z}_1-\hat{z}_2)} = \prod_p \hat{D}_p\left[\pm is\eta_p\left(b_1^{(p)} - b_2^{(p)}\right)\right] \end{cases}, \tag{3.30}
$$

depending on which spin states the two ions are in. The SDKs are separated by a laser repetition period τ_{rep}, and the angle between two successive kicks in rotating phase space is

$$
\Delta\theta = \omega_p \tau_{\text{rep}} = 2\pi \frac{\omega_p}{\omega_{\text{rep}}}. \tag{3.31}
$$

In Duan's fast gate scheme, we require a much larger repetition rate such that $\omega_{\text{rep}} \gg \omega_p$, so the trajectory roughly forms a circle after $n \simeq \omega_{\text{rep}}/\omega_p$ kicks [26], as shown in Fig. 3.5 for an example of $n = 5$. Note that it is impossible to make $\omega_{\text{rep}}/\omega_p$ an integer for all motional modes, so there must be some nonzero displacements after n kicks. However, since $C_p \propto \sum_m s_m e^{i\omega_p t_m}$, the application of another n SDKs in the opposite direction yields

$$
\begin{aligned}
C_p &\propto \sum_{m=1}^{n} e^{2m\pi i\omega_p/\omega_{\text{rep}}} - \sum_{m=n+1}^{2n} e^{2m\pi i\omega_p/\omega_{\text{rep}}} \\
&= \left(1 - e^{2n\pi i\omega_p/\omega_{\text{rep}}}\right) \sum_{m=1}^{n} e^{2m\pi i\omega_p/\omega_{\text{rep}}},
\end{aligned} \tag{3.32}
$$

doi:10.6342/NTU202203211

reducing the original displacement by a factor of

$$1 - e^{2n\pi i\omega_p/\omega_{\text{rep}}} = e^{2n\pi i\omega_p/\omega_{\text{rep}}}\left[e^{2\pi i(1-n\omega_p/\omega_{\text{rep}})} - 1\right] \approx 2\pi i\left(1 - n\frac{\omega_p}{\omega_{\text{rep}}}\right). \tag{3.33}$$

Thus, errors in motional restoration can be suppressed by exploiting the antisymmetry $\mathbf{s}^{(1)} = [+n, -n]$, as shown in Fig. 3.5.

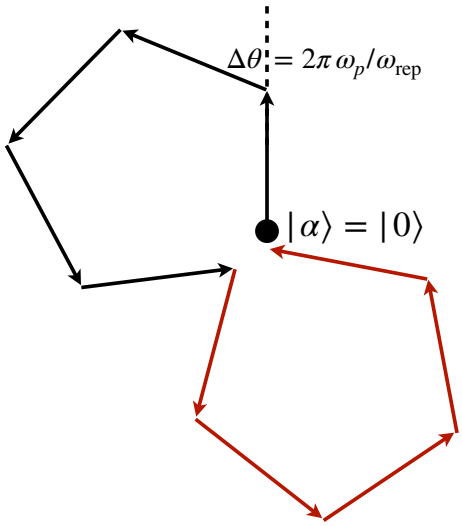

Figure 3.5: Duan's scheme $\mathbf{s}^{(1)} = [+n, -n]$ in rotating phase space for $n = 5$

According to Eq. (3.30), if the two ions are initially in the $|00\rangle$ ($|11\rangle$) or $|01\rangle$ ($|10\rangle$) state, the outlined circles in phase space will have a radius of $R_+^{(p)}$ or $R_-^{(p)}$, where

$$2\pi R_\pm^{(p)} \approx \frac{\omega_{\text{rep}}}{\omega_p} \cdot \eta_p \left| b_1^{(p)} \pm b_2^{(p)} \right|. \tag{3.34}$$

As the mth-order Duan's scheme generates 2^m circles in phase space, the enclosed area is $S_\pm^{(p)} \approx 2^m\pi(R_\pm^{(p)})^2$. We thus require that the relative quantum phase between $|00\rangle$ ($|11\rangle$) and $|01\rangle$ ($|10\rangle$) states be $\Delta\phi = -\pi/4 - \pi/4 = -\pi/2$, i.e.,

$$-\frac{\pi}{2} = \sum_{p=1}^{N} 2S_+^{(p)} - \sum_{p=1}^{N} 2S_-^{(p)} = \sum_{p=1}^{N} \frac{2^m k^2 \hbar \omega_{\text{rep}}^2 b_1^{(p)} b_2^{(p)}}{\pi M \omega_p^3}. \tag{3.35}$$

In this fast gate proposal, the second-order Duan's scheme $\mathbf{s}^{(2)} = [+n, -2n, +n]$ is used,

doi:10.6342/NTU202203211

producing four circles in the rotating phase spaces as plotted in Fig. 3.6. This figure is plotted for an outermost ion pair in the $N = 217$ ion trap. The COM mode trajectory (left) is shown for two ions initially in $|11\rangle$. The zigzag mode trajectory (right) is shown for an initial state $|01\rangle$. Note that the outlined circles in the zigzag mode phase space have extremely small diameters ($\sim 10^{-7}$), indicating a very weak excitation in this mode.

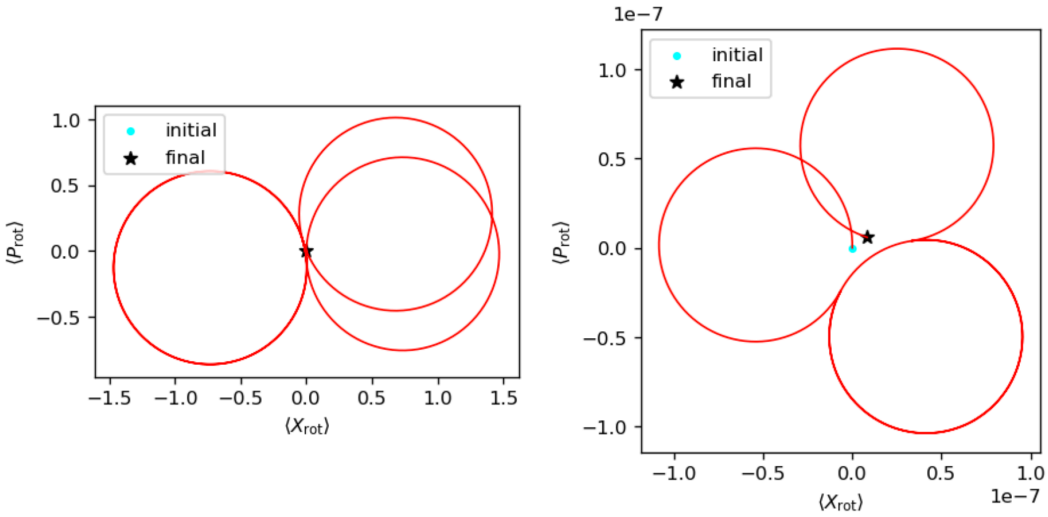

Figure 3.6: Phase space trajectories of the second-order Duan's scheme

In Eq. (3.35), the only variable is $\omega_z(\kappa)$. By tuning the variable κ in AC/DC voltages and hence the axial trapping frequency, the enclosed areas can be optimized to yield a desired quantum phase. After the phase condition is satisfied, we then work on the motional conditions, by finding the optimal integer value of $\omega_{\text{rep}}/\omega_{\text{COM}} \leq n \leq \omega_{\text{rep}}/\omega_{\text{zigzag}}$ (given the optimized ω_z) that minimizes the gate infidelity $\delta F \equiv 1 - F$. Theoretically, this variational trapping frequency scheme should work in the tight-trapping regime. If $\omega_z(\kappa)$ is always large enough to keep the ions tightly bound in a plane (cf. the critical ω_z in Table 2.2), then from Eq. (2.29) we know that varying the diagonal matrix $M\omega_z^2$ I does not alter the mode structures $\mathbf{b}^{(p)}$. The mode coupling of each ion remains the same; only the mode frequencies ω_p will be shifted. To summarize my scheme, the two-qubit gate on an ion pair is implemented by requiring that $\omega_z(\kappa)$ go to its optimal value before the

doi:10.6342/NTU202203211

stroboscopic laser pulses arrive. We will need different axial trapping frequencies ω_z and numbers of pulses n for different pairs of target ions.

It is important to check whether we are working in a stable ion trap when we tune the voltages by κ. In Fig. 3.7 we see that $|a_\nu(\kappa)| < |q_\nu(\kappa)| \ll 1$ for all κ, ensuring a stable ion trap during the operation of the fast gates. Also, it is possible to suggest a theoretical control precision for real-world experiments. Given a fixed number of pulses n, the sensitivity of gate infidelity to $\omega_z(\kappa)$ determines how precise we should control the AC/DC voltages. Fig. 3.8 plots the infidelity for an outermost ion pair in a 217-ion crystal as a function of the control parameter κ. If we set the upper limit to be the fault-tolerant quantum computing threshold of 2×10^{-4} (the gray dashed line) [27], then we obtain a range of allowed κ and AC peak voltage, i.e., $39.41\,\mathrm{V} < \kappa V_0 < 39.66\,\mathrm{V}$. Since the optimal value is $39.53\,\mathrm{V}$, this suggests a control precision of at least $0.1\,\mathrm{V}$ in the AC peak voltage.

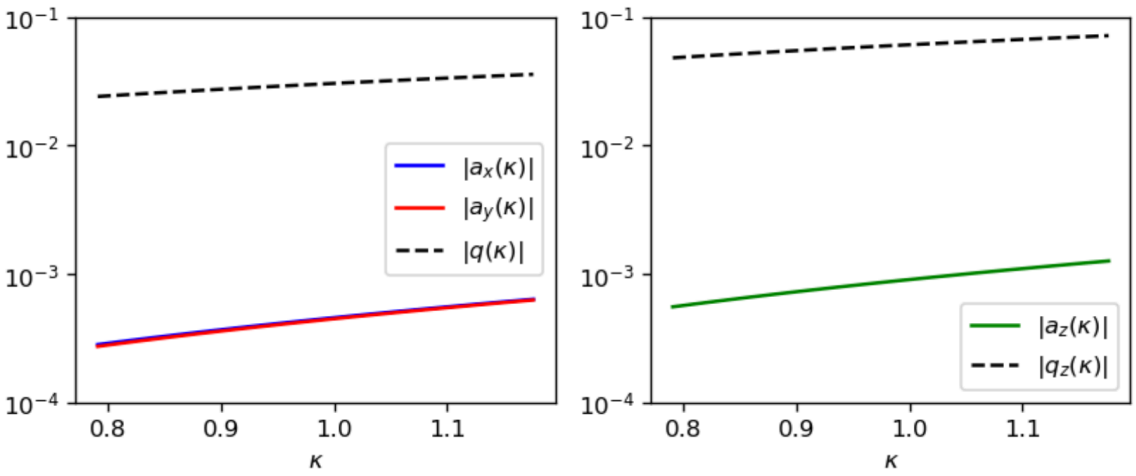

Figure 3.7: $|a_\nu|$ and $|q_\nu|$ as a function of κ

doi:10.6342/NTU202203211

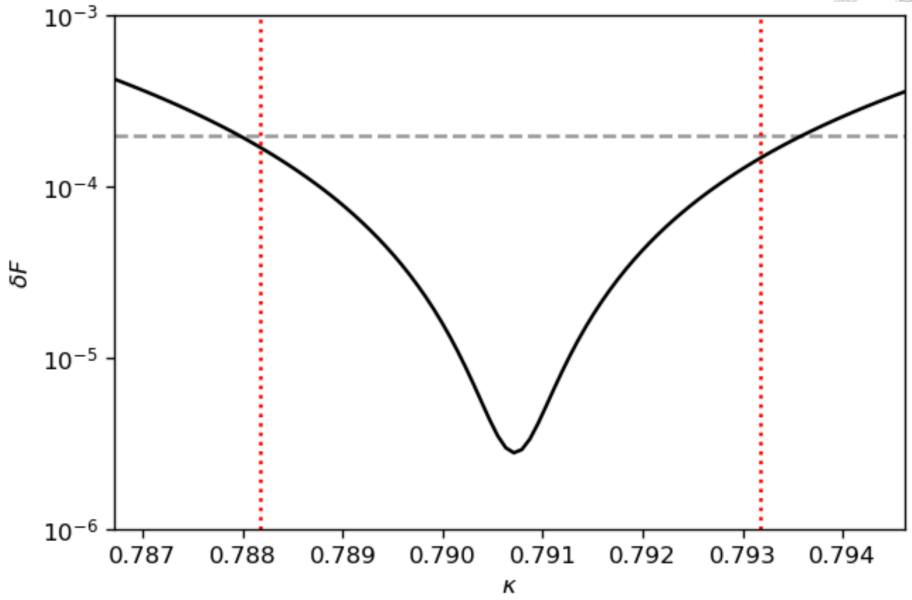

Figure 3.8: Sensitivity of gate infidelity to the control parameter κ

3.2.2 Gate Performance

In this work, a fast gate simulation on the 217-ion crystal is done to suggest the gate performance. Since entangling gates on neighboring ions are sufficient in quantum computing, Fig. 3.9a plots the optimal axial trapping frequency for every pair of neighboring ions. The color of a line segment connecting two ions indicates the value of the needed ω_z, ranging from 2.07 MHz ($\kappa \approx 0.79$) to 3.10 MHz ($\kappa \approx 1.18$), far beyond the critical frequency. In general, inner ion pairs need higher trapping frequencies, but there are still some places where the required ω_z suddenly decrease as compared to their surrounding pairs. The sudden decrease might be related to crystal defects. In the center of the ion crystal, the ions form a nice triangular lattice, where an ion is surrounded by another six ions. However, there is some inevitable irregular arrangement, where an ion is surrounded by five or seven ions, leading to the crystal defects.

Fig. 3.9b shows the gate infidelity for those ion pairs, ranging from $\delta F \approx 4.1 \times 10^{-7}$ to $\delta F \approx 8.5 \times 10^{-5}$, well below a fault-tolerant quantum computing threshold of 2×10^{-4}.

doi:10.6342/NTU202203211

The infidelity can still be very low for the outermost ion pairs ($\sim 10^{-6}$), even though there is notable micromotion. Higher infidelity again happens in the crystal defects. Fig. 3.9c shows the gate time for every ion pairs, ranging from $T_G \approx 1.32\,\mu$s to $T_G \approx 1.96\,\mu$s, significantly faster than typical sideband transition gates. When we adjust the value of κ, the Mathieu coefficient $q(\kappa)$ changes accordingly. Since micromotion amplitudes are proportional to $|q|$, we can expect severe micromotion in the system when we address an ion pair that comes with large $|q(\kappa)|$. Thus, from Fig. 3.9d we expect large micromotion in the crystal when operating the gates on inner ion pairs. Instead, while we operate on the outer ion pairs, their micromotion amplitudes are only roughly $1.5\,\mu$m.

Fast gates can be fast because multiple motional modes are excited, operating far outside the Lamb-Dicke regime. Fig. 3.10 demonstrates an ion's displacement in the z-direction during the kicking of the fast gate, when it is initially in $|\psi_0\rangle = |+\rangle|+\rangle$. The displacement is computed according to Eq. (3.10), i.e.,

$$\langle k\hat{z}_i\rangle = \langle\alpha_p(t)|\sum_{p=1}^{N}\eta_p b_i^{(p)}\left(\hat{a}_p+\hat{a}_p^\dagger\right)|\alpha_p(t)\rangle = \sum_{p=1}^{N}2\eta_p b_i^{(p)}\mathrm{Re}[\alpha_p(t)]\,, \tag{3.36}$$

where $\alpha_p(t)$ is given in Fig. 3.4a. To check the Lamb-Dicke condition, we have to calculate

$$\langle(k\hat{z}_i)^2\rangle^{\frac{1}{2}} = \left|\sum_{p=1}^{N}2\eta_p b_i^{(p)}\mathrm{Re}[\alpha_p(t)]\right| = |\langle k\hat{z}_i\rangle|\,. \tag{3.37}$$

In Fig. 3.10, it is clear that the condition $\langle(k\hat{z}_i)^2\rangle^{1/2} \ll 1$ does not hold for all t, so we are surely working outside of the Lamb-Dicke regime.

In the gate simulation, the initial axial mean phonon occupation is set to be $\bar{n}_p = 0.1$ for all modes ($T \sim 0.05\,$mK). From Fig. 3.11, we may conclude that the initial axial temperature T should not be a limiting factor of gate fidelity. Similar results are also obtained by another research group theoretically [28]. For example, a recent experiment

doi:10.6342/NTU202203211

has just reported $\bar{n} \approx 2.5$ ($T \sim 0.38\,\mathrm{mK}$) in a planar trapped-ion structure [13], which corresponds to an infidelity of $\delta F \approx 1.4 \times 10^{-5}$ in Fig. 3.11. For the Doppler cooling limit of $^{40}Ca^{+}$ ions, $T_D \approx 0.54\,\mathrm{mK}$ ($\bar{n} \approx 3.8$) also keeps the infidelity on the 10^{-5} level, still well below the fault-tolerant threshold of 2×10^{-4} (the gray dashed line). The Doppler temperature is defined by $k_B T_D = \frac{1}{2}\hbar\Gamma$, where $\Gamma/2\pi = 22.3\,\mathrm{MHz}$ is the natural linewidth of the $4S_{1/2} \leftrightarrow 4P_{1/2}$ transition [29].

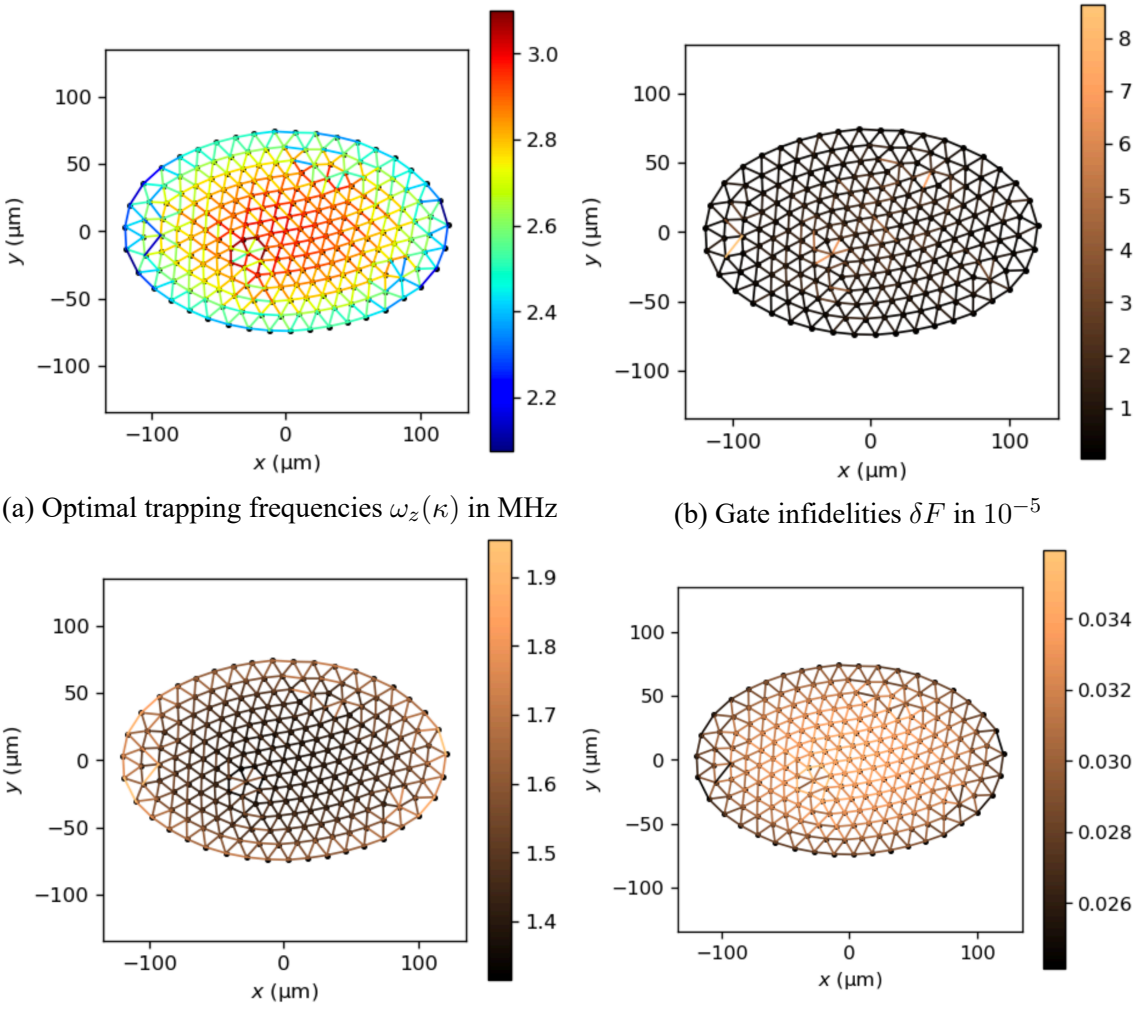

(a) Optimal trapping frequencies $\omega_z(\kappa)$ in MHz

(b) Gate infidelities δF in 10^{-5}

(c) Gate times T_G in μs

(d) Mathieu coefficient $|q(\kappa)|$

Figure 3.9: Optimal ω_z, δF, T_G and $|q|$ for neighboring-ion pairs in a 217-ion crystal

doi:10.6342/NTU202203211

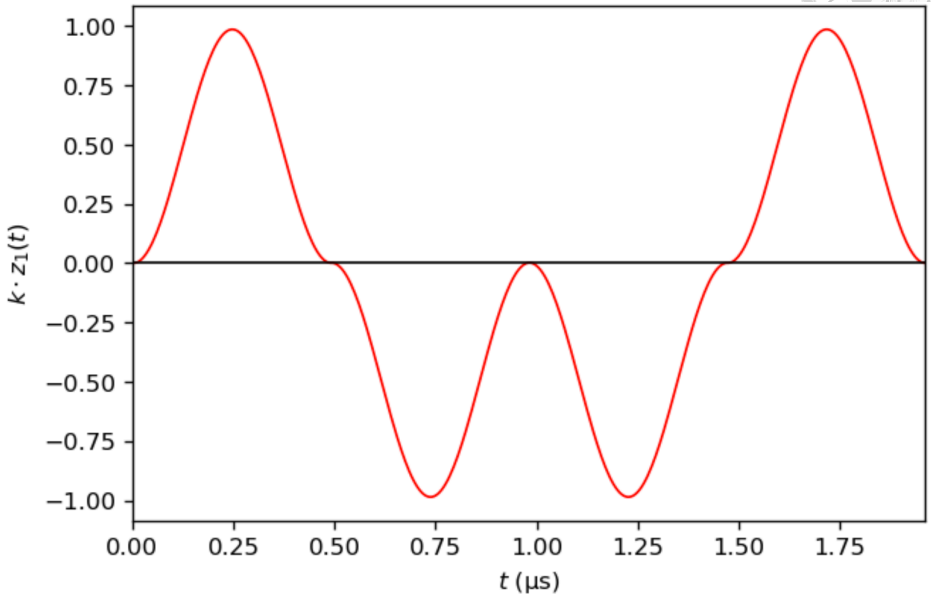

Figure 3.10: Axial displacement of an ion during a fast gate

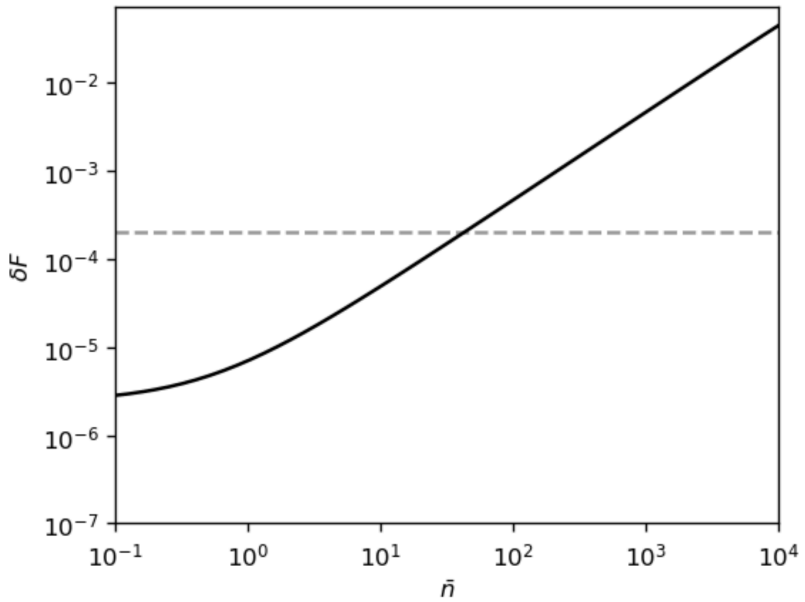

Figure 3.11: Dependence of gate infidelity on the initial axial temperature

doi:10.6342/NTU202203211

3.2.3 Trap Scaling

Fig. 3.12, Fig. 3.13 and Fig. 3.14 show the optimal axial trapping frequencies ω_z, gate infidelities δF and gate times T_G respectively when we scale up our ion trap. A summary of trap scaling is presented in Table 3.1. Generally speaking, we need higher trapping frequencies in larger ion traps. The minimally required trapping frequencies are all far beyond their respective critical values (cf. Table 2.2), ensuring a planar structure throughout the gate operation. As we scale up the ion trap, the maximal gate infidelity among all neighboring ion pairs also increases. Yet surprisingly, the gate times of all ion pairs are decreased in the scaling of traps. It is because larger ω_z results in a smaller n, where $\omega_{\text{rep}}/\omega_{\text{COM}} \leq n \leq \omega_{\text{rep}}/\omega_{\text{zigzag}}$. This also makes sense physically, since every motional mode contributes to the quantum phase: The more motional modes it involves, the faster the quantum phase accumulates.

Table 3.1: Ion trap scaling on optimal ω_z, T_G and δF

N	7	19	37	61	91	127	169	217
Min. ω_z (MHz)	1.75	1.88	1.89	1.95	1.97	1.93	1.96	2.07
Max. ω_z (MHz)	2.24	2.44	2.62	2.70	2.80	2.89	2.95	3.10
Min. T_G (μs)	1.80	1.66	1.54	1.50	1.46	1.42	1.38	1.32
Max. T_G (μs)	2.30	2.16	2.14	2.10	2.08	2.12	2.08	1.96
Max. δF (10^{-5})	0.4	0.7	1.6	2.9	2.9	5.1	7.4	8.5

doi:10.6342/NTU202203211

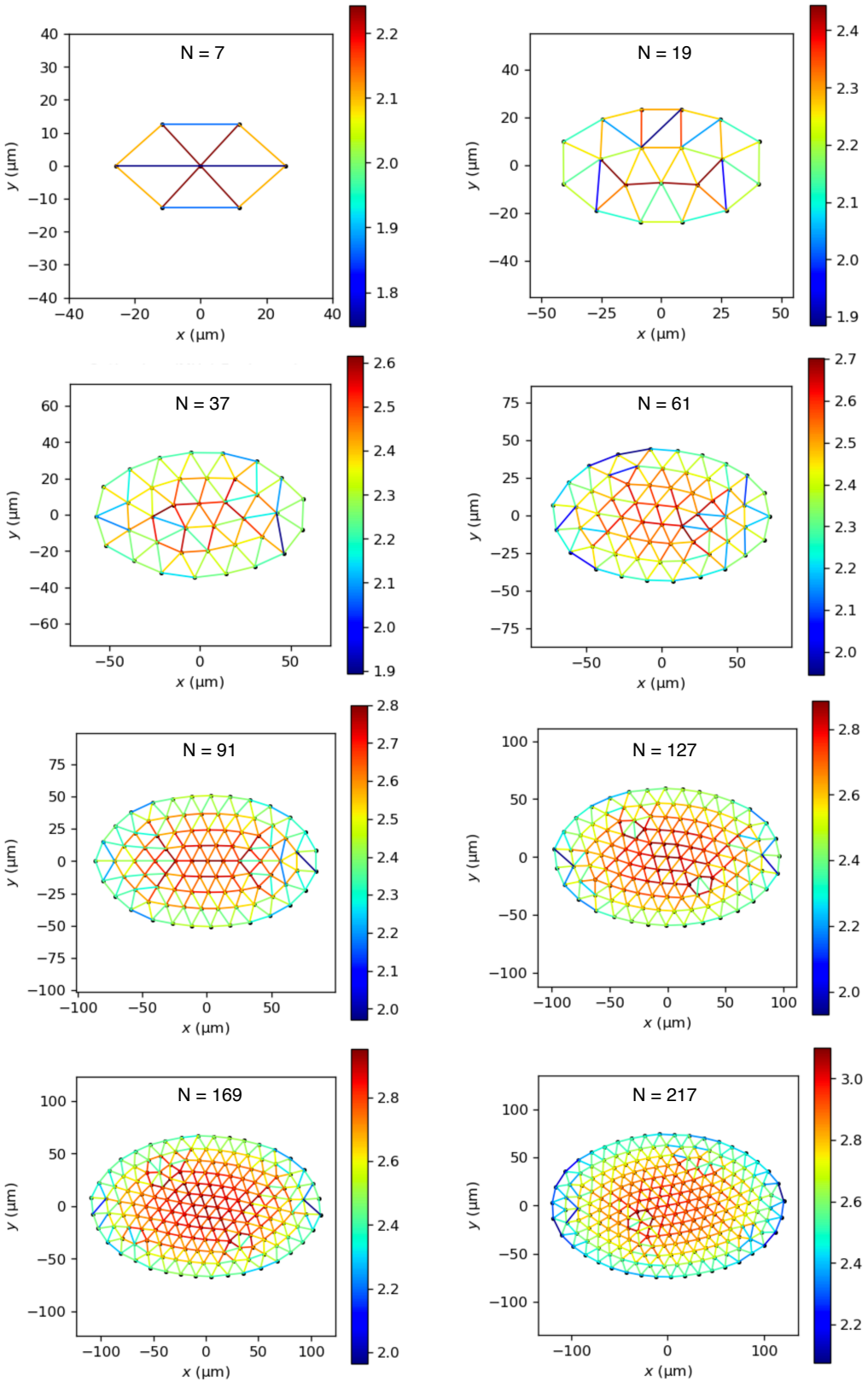

Figure 3.12: Ion trap scaling on optimal ω_z (in MHz)

doi:10.6342/NTU202203211

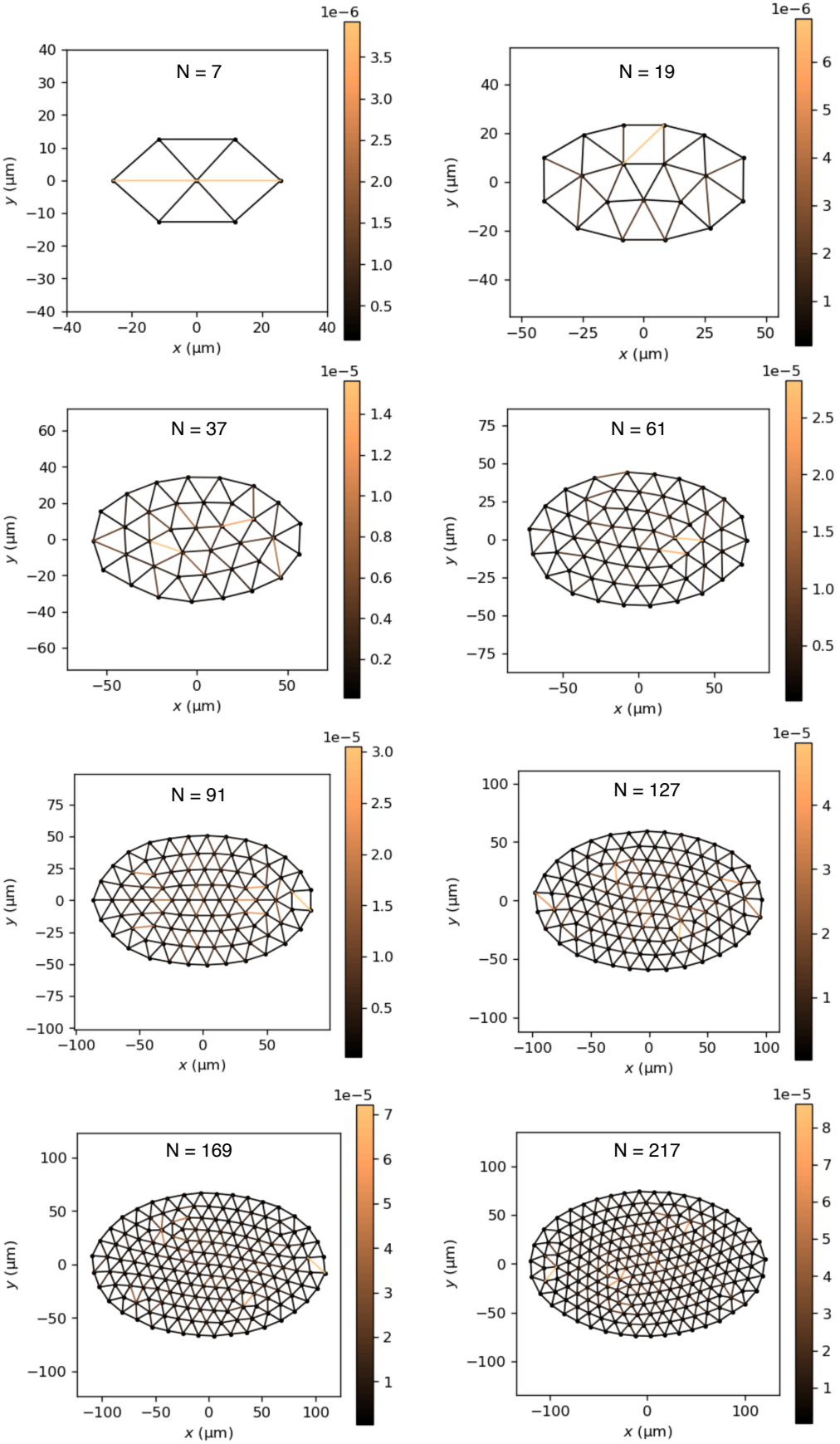

Figure 3.13: Ion trap scaling on gate infidelity

doi:10.6342/NTU202203211

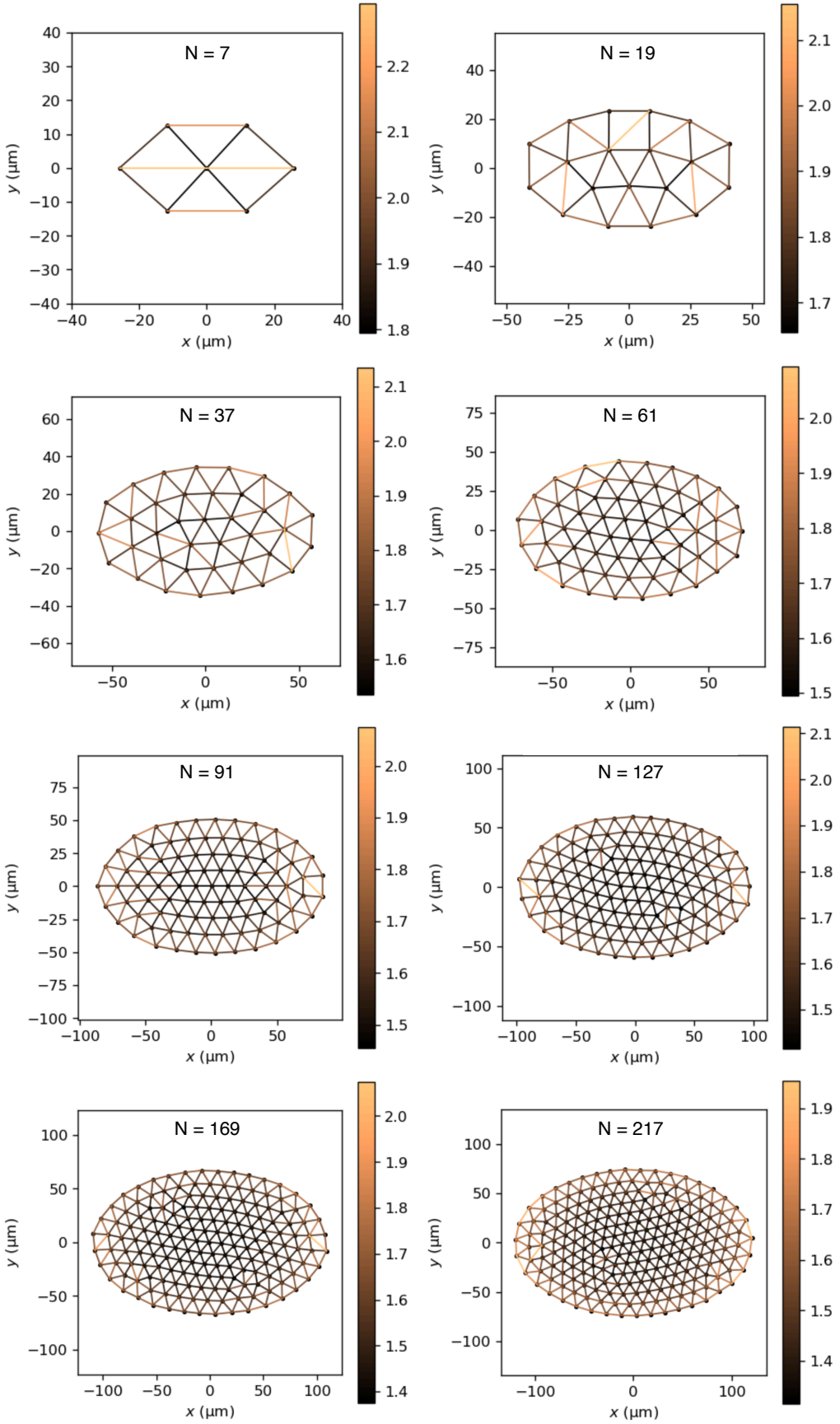

Figure 3.14: Ion trap scaling on gate time (in μs)

doi:10.6342/NTU202203211

3.3 Discussions

3.3.1 Why Outer Ion Pairs Require Lower Trapping Frequencies

From Fig. 3.12 we observe a obvious tendency—outer ion pairs in general require lower trapping frequencies. This can be explained via the formula of acquired quantum phase (Eq. 3.35). Since outer ions have significantly smaller couplings $|b_i^{(p)}|$ to low-frequency modes, we need smaller mode frequencies ω_p (hence smaller ω_z) to obtain the same $-\pi/4$ quantum phase. In Fig. 3.15 some representative mode couplings $|b_i^{(p)}|$ of a 217-ion crystal is shown. Couplings to the four highest-frequency modes are shown in the right column of Fig. 3.15, where the very highest-frequency mode (mode 217) corresponds to the COM mode. On the other hand, couplings to the four lowest-frequency modes are shown in the left column, where the very lowest-frequency mode (mode 1) corresponds to the zigzag mode. It is clear that the coupling of each ion roughly shares the same order of magnitude in the high-frequency regime. However, low-frequency-mode couplings can differ up to several orders of magnitude when we compare the inner and outer ions.

In a physical point of view, we can easily imagine how hard it is to excite zigzag-like (low-frequency) modes by kicking outer ions alone (see Fig. 2.6b for example). Their vanishing Coulomb forces on the center ions can hardly induce zigzag-like oscillations in the middle of the plane, which explains the significantly small coupling to those modes. If laser pulses hit an ion pair composed of outer ions (i.e., an outer ion pair or distant ions), the excited motion will be dominated by COM-like (high-frequency) modes. In order to obtain a fixed quantum phase, we have to in turn considerably excite these COM-like modes, compensating the little area enclosed by low-frequency modes. In this case, lowering

doi:10.6342/NTU202203211

the trapping frequency allows more pulses $n \simeq \omega_{\text{rep}}/\omega_p$ during the gate, achieving the significant excitation of COM-like modes.

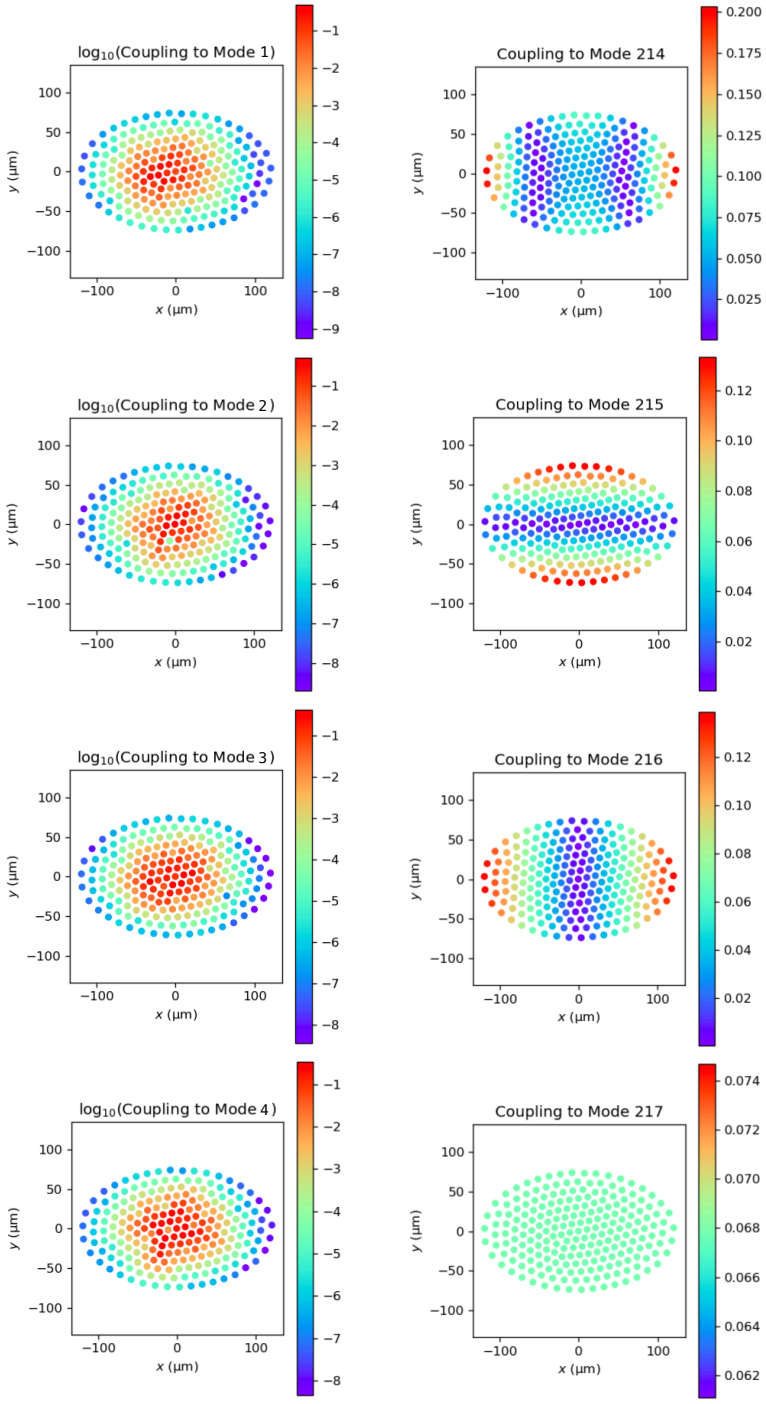

Figure 3.15: Couplings to the four lowest (left) and four highest (right) modes

doi:10.6342/NTU202203211

3.3.2 Distant Ion Pairs

While it is sufficient to entangle neighboring ions, we can still try to extend this scheme and see how far it goes. In Fig. 3.16, six exemplary distant ion pairs are taken to demonstrate the gate performance: (1) a pair separated by one ion, (2) a pair separated by two ions, (3) a pair separated by three ions, (4) a pair separated by half the maximum y-distance, (5) a pair separated by half the maximum x-distance, and (6) the pair with the largest separation. Table 3.2 lists the optimal trapping frequencies ω_z, infidelities δF and gate times T_G of the six ion pairs, calculated with the second-order Duan's scheme. The required trapping frequency decreases as ions are separated farther away. For pair (6) it is no longer possible to find a trapping frequency beyond the critical value (0.86 MHz). We can also see that the infidelity increases rapidly for a distant ion pair. A pair separated by only one ion can make a terrible infidelity of $\delta F \sim 10^{-3}$.

Although the original scheme seems restricted when it comes to distant ion pairs, we can try to lift the limitation with the help of higher-order Duan's schemes. According to Eq. (3.35), higher-order schemes generate more circles in phase spaces, so the required trapping frequency can be made larger. In Table 3.2, the optimal trapping frequencies ω_z', infidelities $\delta F'$ and gate times T_G' calculated with higher-order Duan's schemes are shown. For pair (1), it is good enough to use the fifth-order scheme, and the infidelity is suppressed down to $\delta F \sim 10^{-5}$. For pair (2), the seventh-order scheme is needed to yield an acceptable infidelity of $\delta F \sim 10^{-4}$. However, its gate time is increased up to $44.2\,\mu$s. Thus, applying more laser pulses may improve the fidelity of a distant ion pair, but the gate will no longer be fast. For pair (3)-(6), the pulse sequences of the seventh-order Duan's scheme are just too large to perform the optimization. Yet we can still expect an even

doi:10.6342/NTU202203211

longer gate time for each of the pairs.

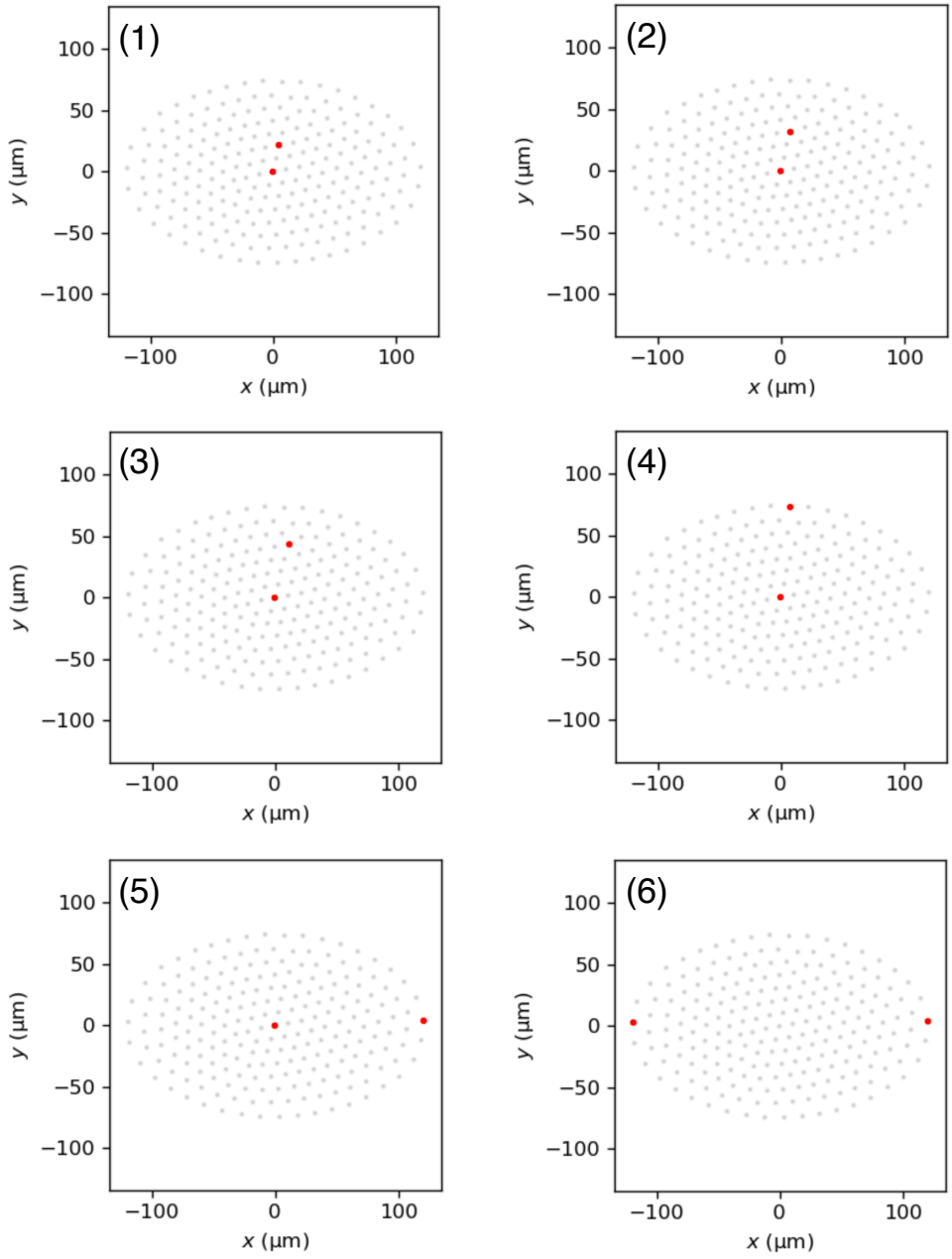

Figure 3.16: Six exemplary distant ion pairs

3.3.3 Pulse Imperfection

The effect of imperfect π pluses has been analyzed in [30, 31]. It is stated that errors in pulse area is a limiting factor to experimental implementations of fast gates, typically

doi:10.6342/NTU202203211

Table 3.2: Optimal trapping frequencies, infidelities and gate times of the distant ion pairs

Pair number	(1)	(2)	(3)	(4)	(5)	(6)
ω_z (MHz)	1.91	1.48	1.22	0.89	0.86	N/A
ω_z' (MHz)	2.92	2.99	2.49	1.84	1.36	0.89
δF	8.7×10^{-3}	0.46	0.75	0.75	N/A	N/A
$\delta F'$	5.1×10^{-5}	1.6×10^{-4}	N/A	N/A	N/A	N/A
T_G (μs)	2.24	3.08	3.90	4.52	N/A	N/A
T_G' (μs)	11.2	44.2	N/A	N/A	N/A	N/A

due to intensity fluctuations of the pulsed laser. In the worst-case analysis, each π pulse has an error θ in its pulse area, and Eq. (3.4) becomes

$$\begin{aligned}\hat{U}_k^\theta \approx & \cos\left(\frac{\pi}{2}-\theta\right)(|1\rangle\langle 1|+|2\rangle\langle 2|) \\ & -i\sin\left(\frac{\pi}{2}-\theta\right)\left[e^{-i(k\hat{z}+\phi)}|1\rangle\langle 2|+e^{i(k\hat{z}+\phi)}|2\rangle\langle 1|\right]+|0\rangle\langle 0| \\ = & \sin\theta\,(|1\rangle\langle 1|+|2\rangle\langle 2|) \\ & -i\cos\theta\left[e^{-i(k\hat{z}+\phi)}|1\rangle\langle 2|+e^{i(k\hat{z}+\phi)}|2\rangle\langle 1|\right]+|0\rangle\langle 0|, \end{aligned} \tag{3.38}$$

resulting in a pulse pair kicking of

$$\hat{U}_s^\theta = \theta^2\hat{I}+\left(1-\theta^2\right)\hat{U}_s+2\theta\sin(k\hat{z})\,(|2\rangle\langle 2|-|1\rangle\langle 1|)+\mathcal{O}(\theta^3), \tag{3.39}$$

where $\hat{I}=|0\rangle\langle 0|+|1\rangle\langle 1|+|2\rangle\langle 2|$ and $\hat{U}_s=e^{2isk\hat{z}}|1\rangle\langle 1|+e^{-2isk\hat{z}}|2\rangle\langle 2|+|0\rangle\langle 0|$. If there are L imperfect kicks on two target ions, then a simple conservative estimation of gate fidelity yields

$$F_\varepsilon \sim (1-\varepsilon_1 L)^2\,(1-\varepsilon_2 L)^2\,F_0, \tag{3.40}$$

where $\varepsilon_i \equiv \theta_i^2$ characterizes the population transfer error of a π pulse for the ith ion, and F_0 is the fidelity calculated with perfect pulses. Eq. (3.40) is valid for $\varepsilon L \ll 1$ and can be used to suggest the allowed pulse errors in experiments. For example, in the case of Fig.

doi:10.6342/NTU202203211

3.9b we can impose an upper limit of a fault-tolerant threshold by

$$\delta F_\varepsilon = 1 - F_\varepsilon \sim 1 - (1 - \varepsilon L)^4 F_0 \lesssim 10^{-4}, \tag{3.41}$$

which gives $\varepsilon \lesssim 10^{-8}$ for every ion pair.

Now we consider a Gaussian profile of beam waist w, centered at the average position $\mathbf{r}^{(0)}$ of an ion. If micromotion was not seriously taken into account, we would have a worst-case error of

$$\frac{1}{2}\Omega e^{-|\mathbf{r}^{(1)}|^2/w^2}\tau \equiv \frac{\pi}{2} - \theta, \tag{3.42}$$

where $\Omega\tau = \pi$, i.e.,

$$\theta = \frac{\pi}{2}\left(1 - e^{-|\mathbf{r}^{(1)}|^2/w^2}\right). \tag{3.43}$$

For the outermost ions in Fig. 2.3 with micromotion amplitude $1.5\,\mu$m, merely $L = 10$ *perfect* π pulses of waist $w = 7\,\mu$m could make $F_0 = 1 - 10^{-6}$ turn into $F_\varepsilon \sim 0.9$. Therefore, resolving the micromotion problem is indeed a crucial work toward practical quantum computing in Paul traps [28].

3.3.4 Effects of Pulse Duration and Beam Waist

The micromotion effects due to a finite pulse duration τ can be shown with the help of Eq. (3.40). Suppose at time t_0 the target ion is located at its average position $\mathbf{r}^{(0)}$ (i.e., $\Omega_T t_0 = \frac{\pi}{2}$), and a laser pulse has just arrived. Due to the micromotion, the ion is displaced slightly in the x-y plane by

$$\left|\mathbf{r}^{(1)} \cos\left(\frac{\pi}{2} + \Omega_T\tau\right)\right| = \left|\mathbf{r}^{(1)}\right| \sin(\Omega_T\tau) \tag{3.44}$$

doi:10.6342/NTU202203211

after the pulse. The pulse area is hence modified by

$$\frac{1}{2}\int_0^\tau \Omega e^{-|\mathbf{r}^{(1)}|^2 \sin^2(\Omega_T t)/w^2} dt \equiv \frac{\pi}{2} - \theta, \tag{3.45}$$

where $\Omega = \pi/\tau$. Of course, for a pair of neighboring ions, finite laser profiles may also result in an overlap. If the two ions are separated by a distance d, then the laser pulses kicking one ion affect the other one roughly by $\Omega e^{-d^2/w^2}$, which can be combined with the integrand of Eq. (3.45) to incorporate the overlapping effect.

In Table 3.3, an outermost pair of neighboring ions (with the largest micromotion) in the 217-ion crystal is used to demonstrate the effects of finite pulse duration and finite beam waist. The original infidelity is $\delta F_0 = 2.8 \times 10^{-6}$. For $w = 3\,\mu$m, a typical ultrafast laser of duration $\tau = 1\,$ps does not compromise the infidelity at all. The radial displacement of the ions within a pulse duration is only on the order of a nanometer. Moreover, the gate remains robust as the pulse duration is increased up to $10\,$ps. For $\tau = 100\,$ps, gate fidelity will drop notably, but we can extend the beam waist to compensate this micromotion effect and obtain a nice infidelity of $\delta F_\varepsilon = 3.9 \times 10^{-5}$. While effects of large pulse duration can be compensated by large beam waist, we should note that the overlapping effect may in turn play an important role and decrease the fidelity if w is set too large. In fact, there is a lower limit on the pulse duration such that $\omega\tau \gg 1$, where

$$\omega = \frac{2\pi c}{393\,\text{nm}} \approx 2\pi \times 763\,\text{THz}, \tag{3.46}$$

and hence the RWA in Eq. (3.2) can be valid [32].

doi:10.6342/NTU202203211

3.3.5 Estimation of Average Laser Power

In order to estimate the required laser power for this fast gate scheme, we first take a look at the Wigner-Weisskopf theory. The theory states that the decay rate of $|2\rangle \rightarrow |1\rangle$ can be expressed as

$$\Gamma_{21} = \frac{\mu^2 k^3}{3\pi\hbar\epsilon_0}, \tag{3.47}$$

where $\mu = |\langle 1|e\hat{\mathbf{r}}|2\rangle|$ is the transition dipole moment. From the lifetime of $|2\rangle$ (6.9 ns) and its branching ratios (given in Fig. 3.17), we can solve

$$\Gamma_{21} = 0.9347\,\Gamma_2 = 0.9347 \cdot \frac{1}{6.9\,\text{ns}} \tag{3.48}$$

for the transition dipole moment, obtaining $\mu \simeq 1.066$ eÅ. Since the Rabi frequency can be expressed by $\Omega \simeq \mu E_0/\hbar$ and $\Omega = \pi/\tau$ for a π pulse, we obtain the electric field amplitude of the laser $E_0 \simeq \hbar\pi/\mu\tau$. The intensity of the laser beam is hence given by

$$I = \frac{1}{2}\epsilon_0 c E_0^2 \simeq \frac{1}{2}\epsilon_0 c \left(\frac{\hbar\pi}{\mu\tau}\right)^2. \tag{3.49}$$

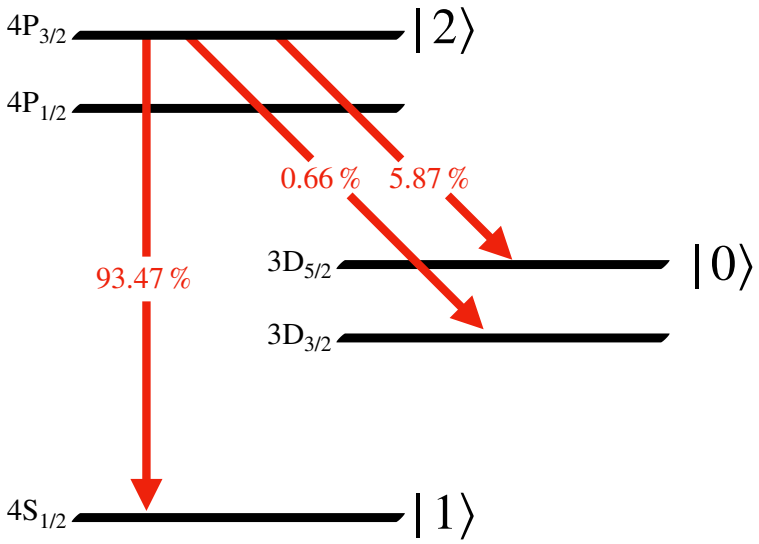

Figure 3.17: Branching ratios for the decay of $|2\rangle$ state

doi:10.6342/NTU202203211

For a Gaussian laser beam of waist w and total power P, the power distributed per unit area defines the intensity, i.e.,

$$I = \frac{P}{\pi w^2/2} = \frac{E_{\text{pulse}}/\tau}{\pi w^2/2}, \tag{3.50}$$

where E_{pulse} is the pulse energy. Combining Eq. (3.50) with Eq. (3.49), we obtain the energy of a single laser pulse

$$E_{\text{pulse}} \simeq \frac{c\epsilon_0 \pi^3 w^2 \hbar^2}{4\mu^2 \tau}, \tag{3.51}$$

and the average laser power can be calculated by

$$\bar{P} = E_{\text{pulse}} \cdot f_{\text{rep}}, \tag{3.52}$$

which is proportional to w^2 and τ^{-1}. The estimated average laser power for different pulse duration τ and beam waist w is shown in Table 3.3. For a typical choice of $(\tau, w) = (1\,\text{ps},\ 3\,\mu\text{m})$, the analysis suggests a laser on the mW-level.

Table 3.3: Micromotion Effects due to a finite pulse duration τ and beam waist w

(τ, w)	$(1\,\text{ps},\ 3\,\mu\text{m})$	$(10\,\text{ps},\ 3\,\mu\text{m})$	$(100\,\text{ps},\ 6\,\mu\text{m})$
Average laser power (mW)	1.412	0.141	0.056
Ion displacement (μm)	10^{-3}	10^{-3}	0.1
δF_ε	2.8×10^{-6}	2.9×10^{-6}	3.9×10^{-5}

3.3.6 Aperiodic Micromotion

In Sec. 2.2, we have seen that the in-plane micromotion is ideally a small periodic oscillation. However, in a real-world experiment the displacements can still be aperiodic. If the ions quite much deviate from the ideal periodic trajectories, the fast gate scheme proposed in this thesis will no longer be micromotion-tolerant. Now the crucial question would be "How do we characterize the degree of aperiodicity, and how does it

doi:10.6342/NTU202203211

affect the gate fidelity?" In fact, a detailed theoretical analysis was provided earlier in [33]. For a cold enough planar crystal, the in-plane micromotion $\mathbf{r}(t)$ basically follows Eq. (2.15). For a more realistic case, we can consider a small perturbation added into the periodic trajectories, i.e., $\mathbf{r}'(t) \equiv \mathbf{r}(t) + \epsilon$. After expanding the Coulomb potential at $\mathbf{r}'(t)$, we can solve the Mathieu equation with the Floquet theory. The Floquet modes $\chi_\nu(t) = \chi_\nu(0)\, e^{i\omega_\nu t}$ $(\nu = 1, 2, \ldots, 2N)$ and the original ion coordinates are connected via the Floquet-Lyapunov transformation. In other words, the ion motion under a small perturbation should be described by a combination of all the $n\Omega_T + \omega_\nu$ frequency terms instead of $n\Omega_T$, and hence there are no definite periods anymore.

While the Floquet-Lyapunov theory provides a more accurate description of the ions' micromotion, how it affects the gate fidelity should be the main focus here. To answer the question, we must first find a way to characterize the degree of micromotion aperiodicity. This has actually been studied in a previous dynamical simulation of planar trapped-ion crystals [11], where the authors provided a concept of radial effective temperature. They defined the effective temperature T_{eff} in the radial (x-y) directions that uses ion velocities v_i computed from displacements δr_i between times that differ by a complete RF period $2\pi/\Omega_T$, in other words, motion that is not periodic with the RF voltage. After computing the radial effective velocities of all ions

$$v_i = \frac{\delta r_i}{2\pi/\Omega_T}, \tag{3.53}$$

we obtain the effective temperature according to the equipartition principle

$$\sum_{i=1}^{N} \frac{1}{2} M v_i^2 \;=\; 2 \cdot \frac{1}{2} N k_B T_{\text{eff}}. \tag{3.54}$$

doi:10.6342/NTU202203211

The root-mean-squared value of the aperiodic displacements δr_i is thus given by

$$\delta r_{\text{rms}} = \frac{2\pi}{\Omega_T}\sqrt{\frac{2k_B T_{\text{eff}}}{M}}. \tag{3.55}$$

In the dynamical simulation [11], an effective temperature of $T_{\text{eff}} = 0.02\,\text{mK}$ was achieved, corresponding to a vanishingly small degree of aperiodicity $\delta r_{\text{rms}} \approx 0.91\,\text{nm}$. In this case, the deviation from the periodic micromotion trajectories can be directly neglected. In the Doppler cooling limit, $T_{\text{eff}} = T_D \approx 0.54\,\text{mK}$ corresponds to $\delta r_{\text{rms}} \approx 4.72\,\text{nm}$, which is still extremely small compared to the micromotion amplitude ($\sim 1\,\mu\text{m}$) of an outermost ion pair in Fig. 2.3. The deviation from the periodic micromotion trajectories causes a pulse error that can be described similarly as in Eq. (3.43), i.e.,

$$\theta = \frac{\pi}{2}\left(1 - e^{-\delta r_{\text{rms}}^2/w^2}\right). \tag{3.56}$$

Given a beam waist $w = 3\,\mu\text{m}$, the gate infidelity for this ion pair only increases a little bit from $\delta F = 2.8 \times 10^{-6}$ to $\delta F_\varepsilon \approx 2.9 \times 10^{-6}$. However, a higher effective temperature, for instance $T_{\text{eff}} = 0.25\,\text{K}$ ($\delta r_{\text{rms}} \approx 0.1\,\mu\text{m}$), would inevitably hinder the gate performance. This problem may similarly be solved by widening the beam waist, as in the last case of Table 3.3.

doi:10.6342/NTU202203211

doi:10.6342/NTU202203211

Chapter 4

Conclusions

In this thesis, a planar trapped-ion structure of the Paul trap is presented. Such 2D traps are more scalable than the traditional 1D ones. Yet aside from the scalability issue, there is inevitable micromotion in a Paul trap regardless of its type (planar or linear). The intrinsic micromotion is shown to be a small in-plane breathing oscillation in a 2D Paul trap. The outermost $^{40}Ca^{+}$ ions (in a 217-ion crystal for example), having the largest ion spacing ($\simeq 15\,\mu$m), suffer from the severest micromotion ($|\mathbf{r}^{(1)}| \simeq 1.8\,\mu$m). Since the ions are tightly bound in a plane, micromotion in the axial (z) direction is highly suppressed and can be neglected. Although entangling gates are designed on the decoupled axial degree of freedom, the radial micromotion can hinder the gate performance if it is not properly taken into consideration.

To circumvent the micromotion issue, a stroboscopic fast entangling gate based on Duan's scheme is proposed, by setting the laser repetition period equal to some multiples of the micromotion period. Pairs of pulses resonant to the 393-nm transition between the $4S_{1/2}$ and $4P_{3/2}$ states are used to generate SDKs. The optimization of gate fidelity includes two variables n and $\omega_z(\kappa)$. By tuning the κ-dependence in the AC/DC voltages, we

doi:10.6342/NTU202203211

first optimize the enclosed phase-space areas and obtain a desired $-\pi/4$ quantum phase. Given this optimized trapping frequency $\omega_z(\kappa)$, we then find the optimal pulse number $n \simeq \omega_{\text{rep}}/\omega_p$ that minimizes the gate infidelity δF. The proposed two-qubit gate on an ion pair is implemented by requiring that $\omega_z(\kappa)$ go to its optimal value before the stroboscopic laser pulses arrive. We will need different axial trapping frequencies ω_z and numbers of pulses n for different pairs of ions.

The entangling gate is conducted between neighboring ions. It remains robust upon the scaling of ion traps, with infidelity ($\sim 10^{-6}$) well below a fault-tolerant quantum computing threshold of $\delta F \sim 10^{-4}$ [27]. The gate time ($\sim 1\,\mu$s) is observed to be decreasing as we scale up the trap. While it is possible to directly entangle pairs of distant ions with higher-order Duan's schemes (i.e., using more laser pulses), the drastically increased gate time would eventually make it inefficient. Theoretically it is suggested that the experimental pulse errors be controlled down to $\varepsilon \lesssim 10^{-8}$ in order for the fault-tolerant quantum computation. For a typical choice of pulse duration and beam waist $(\tau, w) = (1\,\text{ps},\, 3\,\mu\text{m})$, the analysis suggests an average laser power of several mW. Experimentally, the motion of ions should deviate little from the periodic micromotion trajectories in the Doppler cooling limit, where the gate performance would hardly be affected.

doi:10.6342/NTU202203211

Bibliography

[1] J. I. Cirac and P. Zoller, "Quantum computations with cold trapped ions," *Phys. Rev. Lett.*, vol. 74, pp. 4091–4094, May 1995. [Online]. Available: https://link.aps.org/doi/10.1103/PhysRevLett.74.4091

[2] W. Paul, "Electromagnetic traps for charged and neutral particles," *Rev. Mod. Phys.*, vol. 62, pp. 531–540, Jul 1990. [Online]. Available: https://link.aps.org/doi/10.1103/RevModPhys.62.531

[3] R. Ozeri, "The trapped-ion qubit tool box," *Contemp. Phys.*, vol. 52, no. 6, pp. 531–550, 2011. [Online]. Available: https://doi.org/10.1080/00107514.2011.603578

[4] C. D. Bruzewicz, J. Chiaverini, R. McConnell, and J. M. Sage, "Trapped-ion quantum computing: Progress and challenges," *Appl. Phys. Rev.*, vol. 6, no. 2, p. 021314, 2019. [Online]. Available: https://doi.org/10.1063/1.5088164

[5] D. J. Wineland, C. Monroe, W. M. Itano, D. Leibfried, B. E. King, and D. M. Meekhof, "Experimental issues in coherent quantum-state manipulation of trapped atomic ions," *J. Res. Natl. Inst. Stand. Technol.*, vol. 103, no. 3, p. 259, 1998. [Online]. Available: https://www.osti.gov/biblio/665305

doi:10.6342/NTU202203211

[6] D. F. V. James, "Quantum dynamics of cold trapped ions with application to quantum computation," *Appl. Phys. B*, vol. 66, pp. 181–190, 1998. [Online]. Available: https://doi.org/10.1007/s003400050373

[7] D. Zeuch, F. Hassler, J. J. Slim, and D. P. DiVincenzo, "Exact rotating wave approximation," *Ann. Phys. (N. Y.)*, vol. 423, p. 168327, 2020. [Online]. Available: https://www.sciencedirect.com/science/article/pii/S000349162030261X

[8] N. M. Linke, D. Maslov, M. Roetteler, S. Debnath, C. Figgatt, K. A. Landsman, K. Wright, and C. Monroe, "Experimental comparison of two quantum computing architectures," *Proc. Natl. Acad. Sci. U.S.A.*, vol. 114, no. 13, pp. 3305–3310, 2017. [Online]. Available: https://www.pnas.org/doi/abs/10.1073/pnas.1618020114

[9] S.-T. Wang, C. Shen, and L.-M. Duan, "Quantum computation under micromotion in a planar ion crystal," *Sci. Rep.*, vol. 5, p. 8555, 2015. [Online]. Available: https://www.nature.com/articles/srep08555

[10] P. Zou, J. Xu, W. Song, and S.-L. Zhu, "Implementation of local and high-fidelity quantum conditional phase gates in a scalable two-dimensional ion trap," *Phys. Lett. A*, vol. 374, no. 13, pp. 1425–1430, 2010. [Online]. Available: https://www.sciencedirect.com/science/article/pii/S0375960110001106

[11] J. P. Schiffer, M. Drewsen, J. S. Hangst, and L. Hornekær, "Temperature, ordering, and equilibrium with time-dependent confining forces," *Proc. Natl. Acad. Sci. U.S.A.*, vol. 97, no. 20, pp. 10 697–10 700, 2000. [Online]. Available: https://www.pnas.org/doi/abs/10.1073/pnas.190320397

[12] M. K. Ivory, A. Kato, A. Hasanzadeh, and B. B. Blinov, "A Paul trap with sectored ring electrodes for experiments with two-dimensional ion crystals,"

doi:10.6342/NTU202203211

Rev. Sci. Instrum., vol. 91, p. 053201, 2020. [Online]. Available: https://aip.scitation.org/doi/10.1063/1.5145102

[13] M. D'Onofrio, Y. Xie, A. J. Rasmusson, E. Wolanski, J. Cui, and P. Richerme, "Radial two-dimensional ion crystals in a linear Paul trap," *Phys. Rev. Lett.*, vol. 127, p. 020503, Jul 2021. [Online]. Available: https://link.aps.org/doi/10.1103/PhysRevLett.127.020503

[14] C. Shen and L.-M. Duan, "High-fidelity quantum gates for trapped ions under micromotion," *Phys. Rev. A*, vol. 90, p. 022332, Aug 2014. [Online]. Available: https://link.aps.org/doi/10.1103/PhysRevA.90.022332

[15] P. Richerme, "Two-dimensional ion crystals in radio-frequency traps for quantum simulation," *Phys. Rev. A*, vol. 94, p. 032320, Sep 2016. [Online]. Available: https://link.aps.org/doi/10.1103/PhysRevA.94.032320

[16] J. Mizrahi, C. Senko, B. Neyenhuis, K. G. Johnson, W. C. Campbell, C. W. S. Conover, and C. Monroe, "Ultrafast spin-motion entanglement and interferometry with a single atom," *Phys. Rev. Lett.*, vol. 110, p. 203001, May 2013. [Online]. Available: https://link.aps.org/doi/10.1103/PhysRevLett.110.203001

[17] W. C. Campbell, J. Mizrahi, Q. Quraishi, C. Senko, D. Hayes, D. Hucul, D. N. Matsukevich, P. Maunz, and C. Monroe, "Ultrafast gates for single atomic qubits," *Phys. Rev. Lett.*, vol. 105, p. 090502, Aug 2010. [Online]. Available: https://link.aps.org/doi/10.1103/PhysRevLett.105.090502

[18] D. Heinrich, M. Guggemos, M. Guevara-Bertsch, M. I. Hussain, C. F. Roos, and R. Blatt, "Ultrafast coherent excitation of a $^{40}Ca^{+}$ ion," *New J. Phys.*, vol. 21, no. 7, p. 073017, Jul 2019. [Online]. Available: https://doi.org/10.1088/1367-2630/ab2a7e

doi:10.6342/NTU202203211

[19] J. D. Wong-Campos, S. A. Moses, K. G. Johnson, and C. Monroe, "Demonstration of two-atom entanglement with ultrafast optical pulses," *Phys. Rev. Lett.*, vol. 119, p. 230501, Dec 2017. [Online]. Available: https://link.aps.org/doi/10.1103/PhysRevLett.119.230501

[20] J. J. García-Ripoll, P. Zoller, and J. I. Cirac, "Speed optimized two-qubit gates with laser coherent control techniques for ion trap quantum computing," *Phys. Rev. Lett.*, vol. 91, p. 157901, Oct 2003. [Online]. Available: https://link.aps.org/doi/10.1103/PhysRevLett.91.157901

[21] E. Torrontegui, D. Heinrich, M. I. Hussain, R. Blatt, and J. J. García-Ripoll, "Ultra-fast two-qubit ion gate using sequences of resonant pulses," *New J. Phys.*, vol. 22, no. 10, p. 103024, Oct 2020. [Online]. Available: https://doi.org/10.1088/1367-2630/abbab6

[22] C. D. B. Bentley, A. R. R. Carvalho, and J. J. Hope, "Trapped ion scaling with pulsed fast gates," *New J. Phys.*, vol. 17, no. 10, p. 103025, Oct 2015. [Online]. Available: https://doi.org/10.1088/1367-2630/17/10/103025

[23] C. D. B. Bentley, A. R. R. Carvalho, D. Kielpinski, and J. J. Hope, "Fast gates for ion traps by splitting laser pulses," *New J. Phys.*, vol. 15, no. 4, p. 043006, Apr 2013. [Online]. Available: https://doi.org/10.1088/1367-2630/15/4/043006

[24] L.-M. Duan, "Scaling ion trap quantum computation through fast quantum gates," *Phys. Rev. Lett.*, vol. 93, p. 100502, Sep 2004. [Online]. Available: https://link.aps.org/doi/10.1103/PhysRevLett.93.100502

[25] Y. Wu, S.-T. Wang, and L.-M. Duan, "Noise analysis for high-fidelity quantum entangling gates in an anharmonic linear Paul trap," *Phys. Rev. A*, vol. 97, p.

doi:10.6342/NTU202203211

062325, Jun 2018. [Online]. Available: https://link.aps.org/doi/10.1103/PhysRevA.97.062325

[26] Y.-K. Wu and L.-M. Duan, "A two-dimensional architecture for fast large-scale trapped-ion quantum computing," *Chin. Phys. Lett.*, vol. 37, no. 7, p. 070302, Jun 2020. [Online]. Available: https://doi.org/10.1088/0256-307x/37/7/070302

[27] P. Brooks and J. Preskill, "Fault-tolerant quantum computation with asymmetric Bacon-Shor codes," *Phys. Rev. A*, vol. 87, p. 032310, Mar 2013. [Online]. Available: https://link.aps.org/doi/10.1103/PhysRevA.87.032310

[28] A. K. Ratcliffe, L. M. Oberg, and J. J. Hope, "Micromotion-enhanced fast entangling gates for trapped-ion quantum computing," *Phys. Rev. A*, vol. 101, p. 052332, May 2020. [Online]. Available: https://link.aps.org/doi/10.1103/PhysRevA.101.052332

[29] M. Keller, B. Lange, K. Hayasaka, W. Lange, and H. Walther, "Deterministic cavity quantum electrodynamics with trapped ions," *J. Phys. B: At. Mol. Opt. Phys*, vol. 36, no. 3, pp. 613–622, Jan 2003. [Online]. Available: https://doi.org/10.1088/0953-4075/36/3/318

[30] E. P. G. Gale, Z. Mehdi, L. M. Oberg, A. K. Ratcliffe, S. A. Haine, and J. J. Hope, "Optimized fast gates for quantum computing with trapped ions," *Phys. Rev. A*, vol. 101, p. 052328, May 2020. [Online]. Available: https://link.aps.org/doi/10.1103/PhysRevA.101.052328

[31] Z. Mehdi, A. K. Ratcliffe, and J. J. Hope, "Fast entangling gates in long ion chains," *Phys. Rev. Res.*, vol. 3, p. 013026, Jan 2021. [Online]. Available: https://link.aps.org/doi/10.1103/PhysRevResearch.3.013026

doi:10.6342/NTU202203211

[32] C. D. B. Bentley, R. L. Taylor, A. R. R. Carvalho, and J. J. Hope, "Stability thresholds and calculation techniques for fast entangling gates on trapped ions," *Phys. Rev. A*, vol. 93, p. 042342, Apr 2016. [Online]. Available: https://link.aps.org/doi/10.1103/PhysRevA.93.042342

[33] H. Landa, M. Drewsen, B. Reznik, and A. Retzker, "Modes of oscillation in radiofrequency Paul traps," *New J. Phys.*, vol. 14, no. 9, p. 093023, Sep 2012. [Online]. Available: https://doi.org/10.1088/1367-2630/14/9/093023

doi:10.6342/NTU202203211

Appendix A — Trapped-ion Dynamics

A.1 Expansion of Radial Potential Energy in the 2D Trap

Since the RF potential is already in a quadratic form, its matrix representation is straightforward,

$$\sum_{i=1}^{N} e\Phi(x_i, y_i, 0; t) \;=\; \frac{1}{2}\mathbf{r}^{\mathrm{T}}\mathrm{M}_{\mathrm{DC}}\mathbf{r} + \frac{V_0}{d_0^2}\cos(\Omega_T t)\,\mathbf{r}^{\mathrm{T}}\mathbf{r}, \tag{A.1}$$

with $\mathbf{r} = (x_1, \ldots, x_N, y_1, \ldots, y_N)$ and

$$\mathrm{M}_{\mathrm{DC}} = \begin{pmatrix} \frac{2(1+\gamma)eU_0}{d_0^2}\,\mathrm{I}_N & 0 \\ 0 & \frac{2(1-\gamma)eU_0}{d_0^2}\,\mathrm{I}_N \end{pmatrix}, \tag{A.2}$$

where I_N is the $N \times N$ identity matrix. On the other hand, the Coulomb potential energy, $V_C = \sum_{i<j} \frac{e^2}{4\pi\epsilon_0} \frac{1}{\sqrt{(x_i-x_j)^2+(y_i-y_j)^2}}$, should be expanded up to the second order of $\mathbf{r}$ at a given set of equilibrium positions $\mathbf{r}^{(0)}$. If we define

$$(\mathbf{m}_C)_i = \left.\frac{\partial V_C}{\partial r_i}\right|_{\mathbf{r}^{(0)}} \tag{A.3}$$

$$(\mathrm{M}_C)_{ij} = \left.\frac{\partial^2 V_C}{\partial r_i \partial r_j}\right|_{\mathbf{r}^{(0)}}, \tag{A.4}$$

then the Coulomb energy can be approximated by

doi:10.6342/NTU202203211

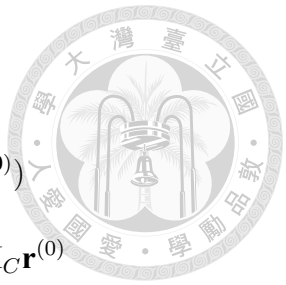

$$
\begin{aligned}
V_C &\approx \text{const.} + \mathbf{m}_C^{\mathrm{T}}(\mathbf{r}-\mathbf{r}^{(\mathbf{0})}) + \frac{1}{2}(\mathbf{r}-\mathbf{r}^{(\mathbf{0})})^{\mathrm{T}}\mathrm{M}_C(\mathbf{r}-\mathbf{r}^{(\mathbf{0})}) \\
&= \text{const.} + \mathbf{m}_C^{\mathrm{T}}\mathbf{r} + \frac{1}{2}\mathbf{r}^{\mathrm{T}}\mathrm{M}_C\mathbf{r} - \frac{1}{2}\mathbf{r}^{(0)\mathrm{T}}\mathrm{M}_C\mathbf{r} - \frac{1}{2}\mathbf{r}^{\mathrm{T}}\mathrm{M}_C\mathbf{r}^{(0)} \\
&= \text{const.} + \left(\mathbf{m}_C - \mathrm{M}_C\mathbf{r}^{(0)}\right)^{\mathrm{T}}\mathbf{r} + \frac{1}{2}\mathbf{r}^{\mathrm{T}}\mathrm{M}_C\mathbf{r}, \qquad \text{(A.5)}
\end{aligned}
$$

where the symmetry of the second-order derivatives ($\mathrm{M}_C = \mathrm{M}_C^{\mathrm{T}}$) has been used. Letting $\mathbf{g} \equiv \mathbf{m}_C - \mathrm{M}_C\mathbf{r}^{(0)}$ and dropping the constant term, we hence derive the quadratic form of V_C in Eq. (2.10). The matrix elements can be computed by evaluating the following derivatives at $\mathbf{r}^{(0)}$:

$$\frac{\partial V_C}{\partial x_i} = \frac{-e^2}{4\pi\epsilon_0}\sum_{j\neq i}\frac{x_i - x_j}{[(x_i-x_j)^2+(y_i-y_j)^2]^{3/2}} \qquad \text{(A.6)}$$

$$\frac{\partial V_C}{\partial y_i} = \frac{-e^2}{4\pi\epsilon_0}\sum_{j\neq i}\frac{y_i - y_j}{[(x_i-x_j)^2+(y_i-y_j)^2]^{3/2}} \qquad \text{(A.7)}$$

$$\frac{\partial^2 V_C}{\partial x_i^2} = \frac{-e^2}{4\pi\epsilon_0}\sum_{j\neq i}\frac{-2(x_i-x_j)^2+(y_i-y_j)^2}{[(x_i-x_j)^2+(y_i-y_j)^2]^{5/2}} \qquad \text{(A.8)}$$

$$\frac{\partial^2 V_C}{\partial x_i \partial x_j} = \frac{-e^2}{4\pi\epsilon_0}\frac{2(x_i-x_j)^2-(y_i-y_j)^2}{[(x_i-x_j)^2+(y_i-y_j)^2]^{5/2}} \qquad \text{(A.9)}$$

$$\frac{\partial^2 V_C}{\partial y_i^2} = \frac{-e^2}{4\pi\epsilon_0}\sum_{j\neq i}\frac{(x_i-x_j)^2-2(y_i-y_j)^2}{[(x_i-x_j)^2+(y_i-y_j)^2]^{5/2}} \qquad \text{(A.10)}$$

$$\frac{\partial^2 V_C}{\partial y_i \partial y_j} = \frac{-e^2}{4\pi\epsilon_0}\frac{-(x_i-x_j)^2+2(y_i-y_j)^2}{[(x_i-x_j)^2+(y_i-y_j)^2]^{5/2}} \qquad \text{(A.11)}$$

$$\frac{\partial^2 V_C}{\partial x_i \partial y_i} = \frac{-e^2}{4\pi\epsilon_0}\sum_{j\neq i}\frac{-3(x_i-x_j)(y_i-y_j)}{[(x_i-x_j)^2+(y_i-y_j)^2]^{5/2}} \qquad \text{(A.12)}$$

$$\frac{\partial^2 V_C}{\partial x_i \partial y_j} = \frac{-e^2}{4\pi\epsilon_0}\frac{3(x_i-x_j)(y_i-y_j)}{[(x_i-x_j)^2+(y_i-y_j)^2]^{5/2}}. \qquad \text{(A.13)}$$

doi:10.6342/NTU202203211

A.2 Solution to the Inhomogeneous Mathieu Equation

The solution to the inhomogeneous Mathieu Equation,

$$\frac{d^2 s_i}{d\xi^2} + [a_i - 2q_i \cos(2\xi)]\, s_i = f_i, \tag{A.14}$$

can be expanded in terms of the Fourier components $\{\cos(2n\xi)\}$, i.e.,

$$s_i = f_i \sum_{n=0}^{\infty} c_i^{(n)} \cos(2n\xi). \tag{A.15}$$

By the substitution of Eq. (A.15) into Eq. (A.14), we get

$$a_i c_i^{(0)} - q_i c_i^{(1)} + \sum_{n=1}^{\infty} \left[\left(a_i - 4n^2\right) c_i^{(n)} - q_i \left(c_i^{(n-1)} + c_i^{(n+1)} \right) - q_i c_i^{(0)} \delta_{n1} \right] \cos(2n\xi) = 1,$$

which implies a set of linear equations,

$$a_i c_i^{(0)} - q_i c_i^{(1)} = 1 \tag{A.16}$$

$$c_i^{(n)} - \frac{1}{D_i^{(n)}} \left(c_i^{(n-1)} + c_i^{(n+1)} + c_i^{(0)} \delta_{n1} \right) = 0, \tag{A.17}$$

where $D_i^{(n)} \equiv \frac{a_i - 4n^2}{q_i}$. The linear equations can be expressed in a matrix form,

$$\begin{pmatrix} a_i & -q_i & & & \\ \frac{-2}{D_i^{(1)}} & 1 & \frac{-1}{D_i^{(1)}} & & \\ & \frac{-1}{D_i^{(2)}} & 1 & \frac{-1}{D_i^{(2)}} & \\ & & \frac{-1}{D_i^{(3)}} & 1 & \\ & & & & \ddots \end{pmatrix} \begin{pmatrix} c_i^{(0)} \\ c_i^{(1)} \\ c_i^{(2)} \\ c_i^{(3)} \\ \vdots \end{pmatrix} = \begin{pmatrix} 1 \\ 0 \\ 0 \\ 0 \\ \vdots \end{pmatrix}. \tag{A.18}$$

Since $1/D_i^{(n)}$ decreases rapidly as n increases, we have $c_i^{(n)} \to 0$ for large n. Therefore, we can truncate Eq. (A.15) at some n, and the finite matrix equation can be easily solved. In practice, it is found that keeping up to $c_i^{(2)}$ already yields enough accuracy. Once the

doi:10.6342/NTU202203211

expansion coefficients $c_i^{(n)}$ are solved,

$$\mathbf{s} = \begin{pmatrix} — & f_1 c_1^{(n)} & — \\ & \vdots & \\ — & f_{2N}\, c_{2N}^{(n)} & — \end{pmatrix} \begin{pmatrix} | \\ \cos(2n\xi) \\ | \end{pmatrix}, \tag{A.19}$$

the ion coordinates are readily available via the transformation $\mathbf{r} = \mathrm{Q}\mathbf{s}$, where Q is defined in Eq. (2.12), i.e.,

$$\begin{aligned} \mathbf{r} &= \mathrm{Q} \begin{pmatrix} — & f_1 c_1^{(n)} & — \\ & \vdots & \\ — & f_{2N}\, c_{2N}^{(n)} & — \end{pmatrix} \begin{pmatrix} | \\ \cos(2n\xi) \\ | \end{pmatrix} \\ &\equiv \mathbf{r}^{(0)} + \mathbf{r}^{(1)} \cos(2\xi) + \mathbf{r}^{(2)} \cos(4\xi) + \cdots, \end{aligned} \tag{A.20}$$

recovering Eq. (2.15). The nth-order micromotion amplitude is hence computed by

$$\mathbf{r}^{(n)} = \mathrm{Q} \begin{pmatrix} f_1 c_1^{(n)} \\ \vdots \\ f_{2N}\, c_{2N}^{(n)} \end{pmatrix}. \tag{A.21}$$

A.3 Formalism of Vibrational Normal Modes

Suppose N ions oscillates slightly in 1D about their equilibrium positions $\mathbf{z}(t) = \mathbf{z}^{(0)} + \boldsymbol{\zeta}(t)$, where $\mathbf{z}^{(0)} = (z_1^{(0)}, \ldots, z_N^{(0)})$ and $\boldsymbol{\zeta} = (\zeta_1, \ldots, \zeta_N)$. The total potential energy of the system can be expanded up to the second order in ζ_i, giving

$$V(\mathbf{z}) \approx V(\mathbf{z}^{(0)}) + \sum_{i=1}^{N} \zeta_i \left.\frac{\partial V}{\partial z_i}\right|_{\mathbf{z}^{(0)}} + \frac{1}{2} \sum_{i,j} \zeta_i \zeta_j \left.\frac{\partial^2 V}{\partial z_i \partial z_j}\right|_{\mathbf{z}^{(0)}}. \tag{A.22}$$

doi:10.6342/NTU202203211

Since by definition the equilibrium positions must lie at a minimum of the potential energy, $\frac{\partial V}{\partial \mathbf{z}}\big|_{\mathbf{z}^{(0)}} \equiv 0$ makes the second term of Eq. (A.22) vanish. After dropping the constant term $V(\mathbf{z}^{(0)})$, we obtain an approximated total energy

$$H \approx \frac{1}{2M}\mathbf{p}^{\mathrm{T}}\mathbf{p} + \boldsymbol{\zeta}^{\mathrm{T}}\mathrm{A}\boldsymbol{\zeta}, \tag{A.23}$$

where $\mathbf{p}$ is the momentum of each ion and

$$\mathrm{A}_{ij} \equiv \left.\frac{\partial^2 V}{\partial z_i \partial z_j}\right|_{\mathbf{z}^{(0)}}. \tag{A.24}$$

The fact that $\mathbf{z}^{(0)}$ lies at a minimum of $V(\mathbf{z})$ means that any small step $\boldsymbol{\zeta}$ away from $\mathbf{z}^{(0)}$ leads to slight increase of the potential energy, i.e.,

$$\Delta V \approx \boldsymbol{\zeta}^{\mathrm{T}}\mathrm{A}\boldsymbol{\zeta} \geq 0 \quad \text{for any } \boldsymbol{\zeta}. \tag{A.25}$$

Therefore, A is a positive semi-definite matrix, possessing non-negative eigenvalues $\mu_p \equiv M\omega_p^2$. The symmetry of A further enables an orthogonal transformation of diagonalization,

$$\mathrm{A}_D = \mathrm{B}^{\mathrm{T}}\mathrm{A}\mathrm{B} = \begin{pmatrix} \mu_1 & & \\ & \ddots & \\ & & \mu_N \end{pmatrix}, \tag{A.26}$$

where the orthogonal matrix B is constructed by inserting the pth-mode eigenvector $\mathbf{b}^{(p)}$ of A into its pth column. If we transform the ion coordinates into the normal coordinates by $\boldsymbol{\zeta} = \mathrm{B}\boldsymbol{\vartheta}$ and $\mathbf{p} \equiv \mathrm{B}\boldsymbol{\varpi}$, then Eq. (A.23) becomes

$$\begin{aligned} H &\approx \frac{1}{2M}\boldsymbol{\varpi}^{\mathrm{T}}\boldsymbol{\varpi} + \boldsymbol{\vartheta}^{\mathrm{T}}\mathrm{A}_D\boldsymbol{\vartheta} \\ &= \sum_{p=1}^{N} \frac{\varpi_p^2}{2M} + \frac{1}{2}M\omega_p^2\vartheta_p^2. \end{aligned} \tag{A.27}$$

doi:10.6342/NTU202203211

The ions hence move in the the normal coordinates as decoupled simple harmonic oscillators, $\vartheta_p(t) = \vartheta_p(0)\cos(\omega_p t)$. The pth vibrational mode can be expressed back in the ion coordinates by

$$\boldsymbol{\zeta}(t) \;=\; \mathrm{B}\begin{pmatrix} 0 \\ \vdots \\ \vartheta_p(t) \\ \vdots \\ 0 \end{pmatrix} \;=\; \vartheta_p(t)\,\mathbf{b}^{(p)}. \tag{A.28}$$

The eigenvector $\mathbf{b}^{(p)}$ thereby tells us the relative motion of the ions. For example, if $\mathbf{b}^{(p)} \propto (1,\,1,\,\ldots,\,1)$, then it is obviously the center-of-mass mode. Furthermore, if one of its components $b_i^{(p)}$ is particularly small, the ith ion must hardly move in the pth mode. We thus say, in other words, that this ion can hardly be coupled to the pth mode. The eigenvector $\mathbf{b}^{(p)}$ hence represents the *mode coupling* of each ion. For a general ion motion, the N ion amplitudes $\boldsymbol{\zeta}$ can be expanded in terms of the N normal modes, giving the linear combination

$$\boldsymbol{\zeta}(t) = \sum_{p=1}^{N} \vartheta_p(t)\,\mathbf{b}^{(p)}. \tag{A.29}$$

doi:10.6342/NTU202203211

Appendix B — Fast Gate Dynamics

B.1 The Displaced Motional States and Acquired Phases

If we define $|\tilde{\alpha}_p\rangle$ as the displaced coherent state and ξ_p as the acquired quantum phase after a whole series of kicks (i.e., by the end of a fast gate), then we have

$$\prod_{m=1}^{L} \hat{D}_p(ic_{mp})\, e^{-i\omega_p \delta t_m \hat{a}_p^\dagger \hat{a}_p} |\alpha_p\rangle = e^{i\xi_p} |\tilde{\alpha}_p\rangle. \tag{B.30}$$

According to Eq. (3.13), for $L = 1$ we have,

$$\begin{cases} \tilde{\alpha}_p = \alpha_p e^{-i\omega_p \delta t_1} + ic_{1p} \\ \xi_p = \mathrm{Re}\left[\alpha_p c_{1p} e^{-i\omega_p \delta t_1}\right] \end{cases}.$$

For $L = 2$,

$$\begin{cases} \tilde{\alpha}_p = \alpha_p e^{-i\omega_p (\delta t_1 + \delta t_2)} + ic_{1p} e^{-i\omega_p \delta t_2} + ic_{2p} \\ \xi_p = \mathrm{Re}\left[\alpha_p c_{1p} e^{-i\omega_p \delta t_1}\right] + \mathrm{Re}\left[\alpha_p c_{2p} e^{-i\omega_p (\delta t_1 + \delta t_2)} + ic_{1p} c_{2p} e^{-i\omega_p \delta t_2}\right] \end{cases}.$$

For $L = 3$,

$$\begin{cases} \tilde{\alpha}_p = \alpha_p e^{-i\omega_p (\delta t_1 + \delta t_2 + \delta t_3)} + ic_{1p} e^{-i\omega_p (\delta t_2 + \delta t_3)} + ic_{2p} e^{-i\omega_p \delta t_3} + ic_{3p} \\ \quad = \alpha_p e^{-i\omega_p T_G} + ic_{1p} e^{-i\omega_p (T_G - t_1)} + ic_{2p} e^{-i\omega_p (T_G - t_2)} + ic_{3p} \\ \\ \xi_p = \mathrm{Re}\left[\alpha_p c_{1p} e^{-i\omega_p \delta t_1}\right] + \mathrm{Re}\left[\alpha_p c_{2p} e^{-i\omega_p (\delta t_1 + \delta t_2)} + ic_{1p} c_{2p} e^{-i\omega_p \delta t_2}\right] \\ \qquad + \mathrm{Re}\left[\alpha_p c_{3p} e^{-i\omega_p (\delta t_1 + \delta t_2 + \delta t_3)} + ic_{1p} c_{3p} e^{-i\omega_p (\delta t_2 + \delta t_3)} + ic_{2p} c_{3p} e^{-i\omega_p \delta t_3}\right] \\ \quad = \mathrm{Re}[\alpha_p c_{1p} e^{-i\omega_p t_1}] + \mathrm{Re}\left[\alpha_p c_{2p} e^{-i\omega_p t_2} + ic_{1p} c_{2p} e^{-i\omega_p (t_2 - t_1)}\right] \\ \qquad + \mathrm{Re}\left[\alpha_p c_{3p} e^{-i\omega_p t_3} + ic_{1p} c_{3p} e^{-i\omega_p (t_3 - t_1)} + ic_{2p} c_{3p} e^{-i\omega_p (t_3 - t_2)}\right] \end{cases}.$$

doi:10.6342/NTU202203211

Hence, it is easy to induct that, for any integer L, we have

$$\begin{cases} \tilde{\alpha}_p = \left(\alpha_p + i\sum_{m=1}^{L} c_{mp} e^{i\omega_p t_m}\right) e^{-i\omega_p T_G} \\ \xi_p = \mathrm{Re}\left[\alpha_p \sum_{m=1}^{L} c_{mp} e^{-i\omega_p t_m}\right] + \sum_{m=2}^{L}\sum_{l=1}^{m-1} \mathrm{Re}\left[i c_{mp} c_{lp} e^{-i\omega_p (t_m - t_l)}\right] \end{cases}, \tag{B.31}$$

which is the coherent state $|\tilde{\alpha}_p\rangle$ and the acquired quantum phase ξ_p for mode p by the end of an arbitrary fast gate.

B.2 Derivation of the Fast Gate Fidelity Formula

By listing all the possibilities of Eq. (3.22),

$$\begin{cases} \hat{U}_{\text{gate}}|00\rangle = e^{i\Theta}|00\rangle \\ \hat{U}_{\text{gate}}|01\rangle = e^{-i\Theta}\prod_p \hat{D}_p\left(\beta_2^{(p)}\right)|01\rangle \\ \hat{U}_{\text{gate}}|10\rangle = e^{-i\Theta}\prod_p \hat{D}_p\left(\beta_1^{(p)}\right)|10\rangle \\ \hat{U}_{\text{gate}}|11\rangle = e^{i\Theta}\prod_p \hat{D}_p\left(\beta_1^{(p)} + \beta_2^{(p)}\right)|11\rangle \end{cases} \tag{B.32}$$

and using the fact of $\hat{D}^\dagger(\beta) = \hat{D}(-\beta)$, we can find a matrix representation of $\hat{\rho}$ in the computational basis

$$\hat{\rho} = \frac{1}{4}\begin{pmatrix} \mathrm{Tr}\left[\hat{\rho}_{\text{th}}\right] & a & b & c \\ a^* & \mathrm{Tr}\left[\hat{\rho}_{\text{th}}\right] & d & f \\ b^* & d^* & \mathrm{Tr}\left[\hat{\rho}_{\text{th}}\right] & g \\ c^* & f^* & g^* & \mathrm{Tr}\left[\hat{\rho}_{\text{th}}\right] \end{pmatrix}, \tag{B.33}$$

where

$$\begin{cases} a = e^{2i\Theta}\,\mathrm{Tr}\left[\prod_p \hat{\rho}_{\text{th}}^{(p)} \hat{D}_p\left(-\beta_2^{(p)}\right)\right] \\ b = e^{2i\Theta}\,\mathrm{Tr}\left[\prod_p \hat{\rho}_{\text{th}}^{(p)} \hat{D}_p\left(-\beta_1^{(p)}\right)\right] \\ c = \mathrm{Tr}\left[\prod_p \hat{\rho}_{\text{th}}^{(p)} \hat{D}_p\left(-\beta_1^{(p)} - \beta_2^{(p)}\right)\right] \\ d = \mathrm{Tr}\left[\prod_p \hat{D}_p\left(\beta_2^{(p)}\right) \hat{\rho}_{\text{th}}^{(p)} \hat{D}_p\left(-\beta_1^{(p)}\right)\right] \\ f = e^{-2i\Theta}\,\mathrm{Tr}\left[\prod_p \hat{D}_p\left(\beta_2^{(p)}\right) \hat{\rho}_{\text{th}}^{(p)} \hat{D}_p\left(-\beta_1^{(p)} - \beta_2^{(p)}\right)\right] \\ g = e^{-2i\Theta}\,\mathrm{Tr}\left[\prod_p \hat{D}_p\left(\beta_1^{(p)}\right) \hat{\rho}_{\text{th}}^{(p)} \hat{D}_p\left(-\beta_1^{(p)} - \beta_2^{(p)}\right)\right] \end{cases}. \tag{B.34}$$

doi:10.6342/NTU202203211

Since $\beta_1^{(p)}$ and $\beta_2^{(p)}$ only differ by a real proportionality constant, the displacement operators appearing in d, f and g can be simplified respectively by

$$\hat{D}(-\beta_1)\,\hat{D}(\beta_2) = e^{i\mathrm{Im}\left[-\beta_1\beta_2^*\right]}\hat{D}(-\beta_1+\beta_2) = \hat{D}(-\beta_1+\beta_2)$$

$$\hat{D}(-\beta_1-\beta_2)\,\hat{D}(\beta_2) = e^{i\mathrm{Im}\left[(-\beta_1-\beta_2)\beta_2^*\right]}\hat{D}(-\beta_1) = \hat{D}(-\beta_1)$$

$$\hat{D}(-\beta_1-\beta_2)\,\hat{D}(\beta_1) = e^{i\mathrm{Im}\left[(-\beta_1-\beta_2)\beta_1^*\right]}\hat{D}(-\beta_2) = \hat{D}(-\beta_2)\,.$$

Given the identity $\prod_p \mathrm{Tr}\left[\hat{\rho}_{\mathrm{th}}^{(p)}\hat{D}_p\left(\beta^{(p)}\right)\right] = \prod_p \exp\left[-\frac{1}{2}\left|\beta^{(p)}\right|^2 \coth\left(\frac{\hbar\omega_p}{2k_BT}\right)\right]$ and an expression for mean phonon occupation $\bar{n}_p = \frac{1}{2}\left[\coth\left(\frac{\hbar\omega_p}{2k_BT}\right)-1\right]$, we can rewrite Eq. (B.33) as

$$\hat{\rho} = \frac{1}{4}\begin{pmatrix} 1 & e^{2i\Theta}\Gamma_2 & e^{2i\Theta}\Gamma_1 & \Gamma_+ \\ e^{-2i\Theta}\Gamma_2 & 1 & \Gamma_- & e^{-2i\Theta}\Gamma_1 \\ e^{-2i\Theta}\Gamma_1 & \Gamma_- & 1 & e^{-2i\Theta}\Gamma_2 \\ \Gamma_+ & e^{2i\Theta}\Gamma_1 & e^{2i\Theta}\Gamma_2 & 1 \end{pmatrix}, \tag{B.35}$$

where

$$\begin{cases} \Gamma_j = \exp\left[-\sum_p \left|\beta_j^{(p)}\right|^2\left(\bar{n}_p+\frac{1}{2}\right)\right] \\ \Gamma_\pm = \exp\left[-\sum_p \left|\beta_1^{(p)}\pm\beta_2^{(p)}\right|^2\left(\bar{n}_p+\frac{1}{2}\right)\right] \end{cases}. \tag{B.36}$$

Here T is a characteristic temperature describing the initial out-of-plane motion, with a mean phonon number $\bar{n}_p$ for the pth motional mode. The gate fidelity will be readily available after we insert Eq. (B.35) into Eq. (3.23),

$$\begin{aligned} F &= \frac{1}{4}\begin{pmatrix} e^{i\frac{\pi}{4}} & e^{-i\frac{\pi}{4}} & e^{-i\frac{\pi}{4}} & e^{i\frac{\pi}{4}} \end{pmatrix}\hat{\rho}\begin{pmatrix} e^{-i\frac{\pi}{4}} \\ e^{i\frac{\pi}{4}} \\ e^{i\frac{\pi}{4}} \\ e^{-i\frac{\pi}{4}} \end{pmatrix} \\ &= \frac{1}{8}\left[2+\Gamma_+ +\Gamma_- -2\left(\Gamma_1+\Gamma_2\right)\sin(2\Theta)\right]. \end{aligned} \tag{B.37}$$

doi:10.6342/NTU202203211